FUNCTIONAL HYBRID NANOARCHITECTURES AND SCALABLE NANOMANUFACTURING TECHNOLOGIES FOR ENERGY CONVERSION AND OPTOELECTRONICS

by

Jong G. Ok

A dissertation submitted in partial fulfillment
of the requirements for the degree of
Doctor of Philosophy
(Mechanical Engineering)
in the University of Michigan
2013

Doctoral Committee:

Professor L. Jay Guo, Chair
Assistant Professor A. John Hart, Co-Chair
Associate Professor Jinsang Kim
Professor Katsuo Kurabayashi

To my advisor who guided my work,

To my colleagues who enriched my work,

and

To my family who enabled everything

Acknowledgements

It has been an amazing and rewarding experience to study and reach this point at the University of Michigan – a place full of inspirations unending, resources unbounded, and people unforgettable. It is my greatest pleasure now to thank all who spurred, nurtured, and furthered this thesis work.

With my first and foremost gratitude, I thank my advisor Professor L. Jay Guo. He has guided and encouraged my work and me with his insightful instructions and revitalizing support. I also sincerely appreciate my co-advisor Professor A. John Hart. Professor Hart has rationally and supportively galvanized my work and myself into this exciting stage. My deep appreciation extends to my committee members, Professor Jinsang Kim and Professor Katsuo Kurabayashi. They have provided me with constructive comments and invigorative criticisms that bolstered the quality and completeness of this work.

My earnest acknowledgement goes to two more persons: Dr. Se Hyun Ahn and Dr. Moon Kyu Kwak. It is unimaginable how this work could be done without Dr. Ahn's indispensable support and Dr. Kwak's thorough and enlivening contributions.

I especially appreciate Dr. Hui Joon Park for his essential and dedicated helps; Dr. Hyoung Won Baac for his extensive collaborations; Dr. Hong Seok Youn, Jae Yong Lee, and Kyu-Tae Lee for their enthusiastic assistance. I thank all my colleagues, regardless of whether they are still by my side or somewhere else, including Dr. Sameh H. Tawfick, Chad M. Huard, Dr. Carlos A. Pina-Hernandez, Young Jae Shin, K. Anne Juggernauth, Sei-Jin Park, Alex A. McLane, Cheng Zhang, Dr. Tao Ling, Jinjing Li, Dr. Yongyi Zhang, Dr. Kai Sun, Yisi Liu, and Dr. Anton Greenwald for their foregoing and/or ongoing contributions; and Hyunsoo Kim, Taehwa Lee, Taehee Jang, Dr. Haofei Shi, (An)Drew E.

Hollowell, Dr. Alex F. Kaplan, Dr. Yi-Kuei Wu, Dr. Ting Xu, Ashwin Panday, Dr. Sung-Liang Chen, Dr. Jing Zhou, Dr. Youngki Hong, Dr. Yeotaek Yoon, Dr. Myung-Gyu Kang, Long Chen, Christina M. Jones, Brandon D. Lucas, Fan Yang, Yang Yang, Dr. Eric R. Meshot, Dr. Jiseok Lee, Dr. Onas Bolton, Girish S. Kulkarni, Dr. Seunghyun (Sean) Lee, Dr. Nanditha Dissanayake, Dr. Chung Chiang Wu, Professor Zhaohui Zhong, Dr. Pilar C. Herrera-Fierro, Dr. John F. Mansfield, and many others for broadening, deepening, and colorizing my professional spectrum.

I additionally acknowledge all staff of the Lurie Nanofabrication Facility (LNF), the Electron Microbeam Analysis Laboratory (EMAL), the Solid State Electronics Laboratory (SSEL) at the University of Michigan and other facilities for technical and administrative aids. I also acknowledge all of the grants and fellowships from the University of Michigan, National Science Foundation (NSF), Defense Advanced Research Projects Agency (DARPA), Nissan Chemical, and other sponsors for financial supports.

Most importantly, I am indebted to my dear parents and all of my family for their endless love and self-giving support and to my priceless daughter Claire Minseo for her blissful but babble-encrypted cheering. Last, but not least, I owe everything to my beloved wife Bo Hyun Hong. She is the co-author of this thesis.

Table of Contents

List of Figures

List of Tables

List of Appendices

Abstract

Owing to their extraordinary ability to interacting with external stimuli as well as their versatile functionalities hardly observed in bulk systems, micro- and nano-scale materials, structures, and phenomena have been the subject of increasing interest from both academia and industry. Many diverse fields including optoelectronics, photonics, bioengineering, and energy conversion have all shown significant increases in utilization of, and need for, micro/nano-scale features. To meet this demand scalable, practical, and efficient methodologies for small-scale manufacturing are called for.

This thesis work addresses these issues while focusing on three main topics: (1) how micro/nano-scale structures and materials can be integrated into hybrid assemblies that can combine their complementary functionalities and extend applicability; (2) how these functional nanoarchitectures can be engineered in a continuous and scalable manner to increase the manufacturing throughput; and (3) how those two approaches can be coupled to the scalable buildups of functioncal nanoarchitectures to facilitate practical applications ranging from energy converters to optoelectronics/photonics.

More specifically, a 3D-hierarchical hybrid assembly of functional zinc oxide nanowires (ZNWs) and electrically addressable carbon nanotubes (CNTs) is developed and its application to photoelectric energy conversion is investigated. A series of continuous and scalable nanomanufacturing technologies follow, realizing high-speed (up to 1 m/min) patterning of small-scale features down to sub-100 nm resolution; Roll-to-Roll (R2R) process enables the continuous fabrication of large-area replica of desired pattern by continuously rolling the flexible master mold containing the counter-profiled pattern; NanoChannel-guided Lithography (NCL) can continuously create seamless and high aspect-ratio nanogratings by dynamically inscribing the cleaved grating mold edge

at a tilted angle over the liquid resist-coated surface; finally, Vibrational Indentation-driven Patterning (VIP) accomplishes a template-free fabrication of micro/nano-scale gratings via the high-frequency periodic indenting of a ‘flat’ tool edge. The integrative scaling-up of functional nanodevices is then further implemented in two ways; first, the ZNW/CNT hybrids are processed into scalable thin film photodetectors via roll-processing, achieving rapid photoresponse (< 0.3s) and high external quantum efficiency (> 35%); second, Photo Roll Lithography (PRL) is developed by combining conventional photolithography and continuous rolling, which realizes high-throughput fabrication of geometrically-tunable sub-micron patterns for transparent electrodes and plasmonic IR filters.

Chapter 1

Introduction

1.1 Background and motivation

Nanoarchitectures involving nanomaterials and nanoscale pattern structures are of great interests due to their ability to sensitively interacting with external stimuli such as light, force, and chemical species, as well as their extraordinary properties (e.g. mechanical, electrical, optical, and chemical) which are hardly observed in bulk systems. These outstanding characteristics found in nanoscale structures have led to a significant amount of research effort for their utilizations to a variety of applications ranging from optoelectronics to energy conversion devices[1-4].

There are two main approaches to achieve the nanostructures: 'bottom-up' synthesis and 'top-down' fabrication. Through a series of bottom-up procedures including chemical vapor deposition (CVD), catalysis, and solution chemistry, various nanomaterials with a diversity of structural configurations such as one-dimensional (1-D) structures (e.g. carbon nanotubes[5], semiconducting nanowires[6]) and 2-D thin films (e.g. graphene[7]) can be synthesized. These nanoscale constructs are attractive due to the high surface area along with the specific properties, yet are limited by their directly synthesizable length or area and by sometimes conflicting requirements for the

nanostructures both to convert or store energy carriers (e.g. by charge separation or intercalation), and to manipulate or transport electrons or photons. Therefore, both scalable engineering of individual nanostructures and multidimensional assembly of large numbers of complementary nanostructures into functional architectures that meet application-specific needs, are called for.

Micro/nano-scale structures with diverse features can be fabricated by many top-down micronanofabrication methods such as photo- or e-beam lithography[8] which however typically suffer from low throughput and high cost. Nanoimprint lithography (NIL)[1, 9] technology opens a way to high-throughput fabrication of nanostructures at great precision and low costs. NIL benefits from direct mechanical deformation of the resist material and therefore can realize resolutions beyond what conventional photo- or e-beam lithography can do that are limited by light diffraction or beam scattering. Since conventional NIL (i.e. thermal and UV) is basically a "stamping" process to replicate the micro/nanopatterns from the master 'mold' to another substrate, the productivity is critically dependent on the mold pre-fabrication step and the area a mold can be made up to. To avoid this bottleneck and to enable large-area nanopatterning at high speed, developing continuous, high-throughput, and scalable nanomanufacturing processes is highly requested.

Rationally designing, feasibly manufacturing, and intensively studying the performance of functional nanoarchitectures at multiple length scales, which can be derived from either bottom-up or top-down, by integrating both methodologies, but universally underpinned by the understandings of capabilities and limitations of novel materials and structures, are indispensable towards the next-generation applications

ranging from clean-energy harvesters to flexible electronics that will bolster the future of our society. With that sense has this work begun.

1.2 Nanostructures as functional building blocks: properties and applications

This section provides an overview of several nanostructures that the thesis will deal with as functional building blocks with particular interests throughout the following main work chapters; first as the bottom-up synthesizable nanomaterials, carbon nanotubes (CNTs) and zinc oxide (ZnO) nanowires (NWs) will be introduced, and the nanograting structures will then be presented as the top-down fabricable nanostructures. While focusing on their remarkable properties and why and how these nanostructures can work as functional components, representative applications based on these structures will also be briefly discussed.

1.2.1 Carbon nanotubes

Since discovered by S. Iijima in 1991[10], carbon nanotubes (CNTs) have addressed enormous research interests as well as practical applications for decades due to their versatile and outstanding properties. CNTs can be depicted in one phrase as the seamless cylinders of carbon atoms arranged in a hexagonal lattice[5], as illustrated in **Figure 1.1**[11]. Each carbon atom is bound to three adjacent ones in 120° lateral angle through σ-bonding within an atomically thin graphite layer (**Figure 1.1a**) which is wrapping around, and is continuing along, the cylinder axis. Depending on whether a CNT consists of one graphite wall or multiple walls concentrically stacked (where these

individual graphite layers are bound through van der Waals force as well as π-bonding along the in-plane direction with a spacing of ~0.34 nm), it can be categorized into a single-walled CNT (SWCNT; **Figure 1.1b**) and multi-walled CNT (MWCNT; **Figure 1.1c**). Typical diameters range from 0.4 to 5 nm for SWCNTs and can be up to hundreds of nm's for MWCNTs, while their lengths can be readily elongated up to mm scale by controlling the synthesis conditions (e.g. extended growth time). This structural nature of CNTs, as 'nearly one-dimensional' hollow carbon construct, leads to a diversity of extraordinary properties that are hardly found in other natural or bulk carbon structures such as planar graphite or carbon black.

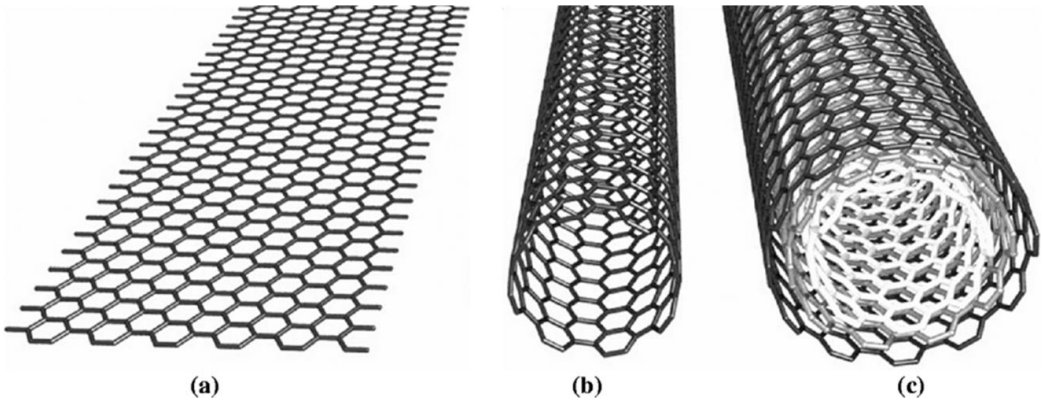

Figure 1.1 Schematic illustrations of (a) a single graphite layer where carbon atoms are laterally connected in the same plane, and (b) single-walled carbon nanotubes (SWCNTs) and (c) multi-walled carbon nanotubes (MWCNTs) that are constructed by a single or multiple graphitic layer(s) wrapping around the tube axis (Figure source: Figure 1 in F. Kreupl, *et al.*, *IEEE Int. Elec. Devices Meeting 2004, Technical Digest*, 2004).

For instance, CNTs possess excellent electrical conductivity along with tunable band gap properties depending on their structural configurations[5, 12]. At first, since the band gap of a CNT is inversely proportional to the diameter, CNTs having the diameter larger than ~3 nm turn to have the band gap smaller than the room-temperature thermal energy, and therefore behave like metals[5]. Thus in geometrical point of view, almost all

MWCNTs are metallic while SWCNTs can be either metallic or semiconducting depending on their diameters as well as chirality[13]. Additionally, the free electrons originating from the inter-layer π-bonding groups existing in between the layers of a MWCNT contribute to their metallic behavior.

The resistivity of 'individual' CNTs along the axis has been experimentally measured to be in 10^{-4}-10^{-6} Ω-cm range[14]. While this value already indicates high conductivity of CNTs, we can practically obtain much reduced resistivity in most of the CNT structures containing multiple CNTs; a number of lateral electrical contacts formed among neighboring CNTs further increases the total conductivity of the CNT structure. Furthermore, room-temperature ballistic electron transport has been observed over μm-scale distances in SWCNTs[15] as well as through parallel channels in MWCNTs[16]. Also, CNTs can carry a very high current density of up to 4×10^9 A/cm^2[17], which makes them very attractive for reliable electrical conductors and nanoelectronic templates.

Along with such excellent electrical properties, CNTs also show remarkable mechanical, thermal, and (electro)chemical properties. MWCNTs show an exceptional mechanical properties (i.e. ~1 TPa in modulus and ~100 GPa in strength)[18] and have superb thermal conductivity higher than 3000 W/m-K[19]. A wide range of functionalizability of CNTs along with chemical robustness[20] further extend the use of CNTs for (electro)chemical and/or biological sensors and target-oriented templates (e.g. Li^+, DNA) that often demand harsh chemical environment and long operation life.

Encouraged by such a versatile set of outstanding properties of CNTs, there have been a myriad of applications based on individual or combinative properties of CNTs.

Field-effect transistors[15, 21, 22], (super-)capacitors[23-26], transparent conducting electrodes[27, 28], mechanically, thermally, or electrically enhanced nanocomposites[29-31], chemical and biological sensors and actuators[32-36], energy converters[37, 38] and storages[39-42], and battery electrodes[43, 44] are just a few examples that have been demonstrated so far. Recently, the investigation and utilization of extraordinary optical properties of CNTs have also actively emerged, resulting in the demonstrations of perfect light absorbing metamaterials and optoacoustic ultrasound generators for bio therapy. Not limited to all above, a lot more will surely follow.

1.2.2 Zinc oxide nanowires

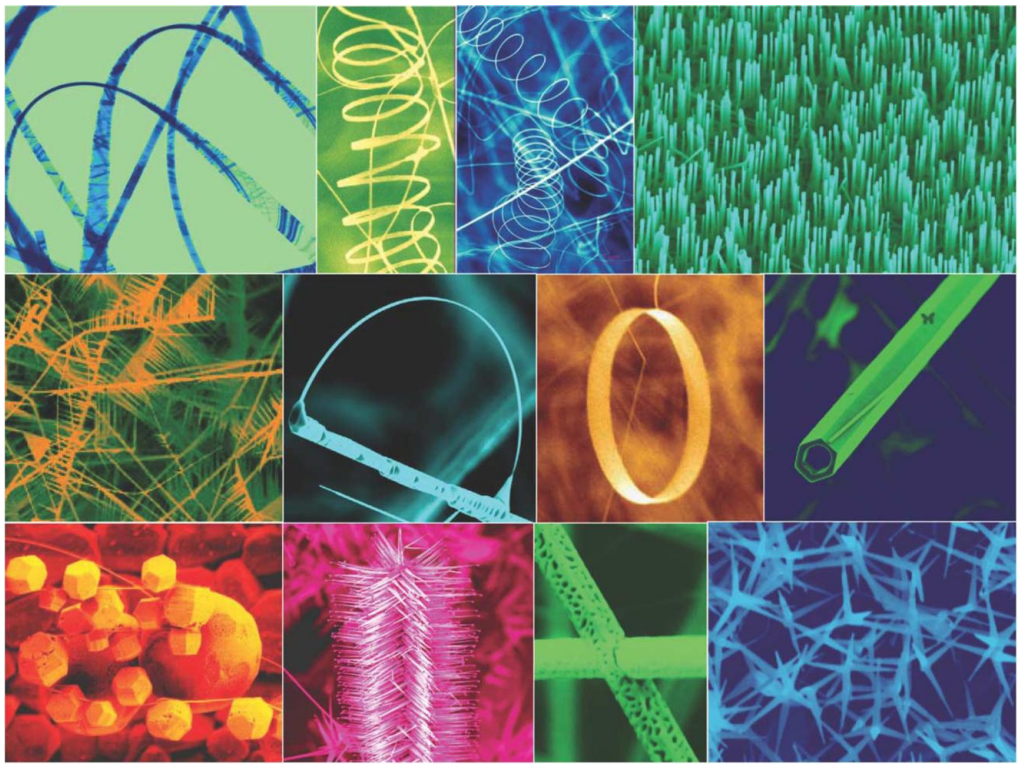

Figure 1.2 Various ZnO nanostructures (artificially colored) ranging from one-dimensional nanowires, nanorods, and nanobelts, to multidimensional nanorings, nanocombs, nanobristles, and nanostars (Figure source: Figure 1 in Z. L. Wang, *Mater. Today*, 2004).

Zinc oxide (ZnO) nanostructures have drawn significant research efforts in both academia and industry because of their wide structural configurations and diverse functionalities. **Figure 1.2**[45] shows several ZnO nanostructures whose structural configurations span from one-dimensional nanobelts and nanowires (NWs) to multidimensional nanobristles and nanosprings. Among those various structural formats, ZnO NWs (ZNWs), the one-dimensionally stacked crystalline ZnO structures, are particularly attractive in terms of the quantum confinement effects originating from their nanoscale one-dimensional architecture[46].

ZNWs are structured as hexagonal wurtzite where the tetrahedrally coordinated O^{2-} and Zn^{2+} ions are alternatively stacked along the c-axis (i.e. [0001] direction).Such a non-central symmetric structure of ZNWs along with large electromechanical coupling[46] induces piezoelectricity[3] and pyroelectricity[47] upon mechanical bending or exposure to temperature change. Besides, since ZnO is a wide band-gap (≈3.37 eV) n-type semiconductor with large exciton binding energy (≈60 meV), ZNWs show UV range photoluminescence[48] as well as UV-induced photoconductivity[49]. In addition, ZNWs show tunable electrical conductivity depending on the surrounding gas molecules, according to the reversible chemisorption mechanism of reducing gas species interacting with the oxygen molecules on the ZnO surface (thereby changing the ZnO conductivity)[50].

Capitalizing these versatile properties of ZNWs, a variety of applications have been extensively demonstrated, including: UV nanolasers and photodetectors[48, 51], piezoelectric nanogenerators[52, 53], transistors[54, 55], photovoltaic cells[56, 57], and sensors for chemical and biological molecules[50, 58-61]. However, the intrinsic high

resistivity of ZNWs (i.e. ~MΩ-cm scale[51]) may degrade the practical applicability of ZNWs by themselves, especially for high-current generation and/or sensitive photodetection; quenching this drawback, for example, through assembling with other electrically communicable nanostructures with higher electrical conductivity such as CNTs, will be one of the most important aspects elaborated in this thesis work.

1.2.3 Micro/nano-gratings

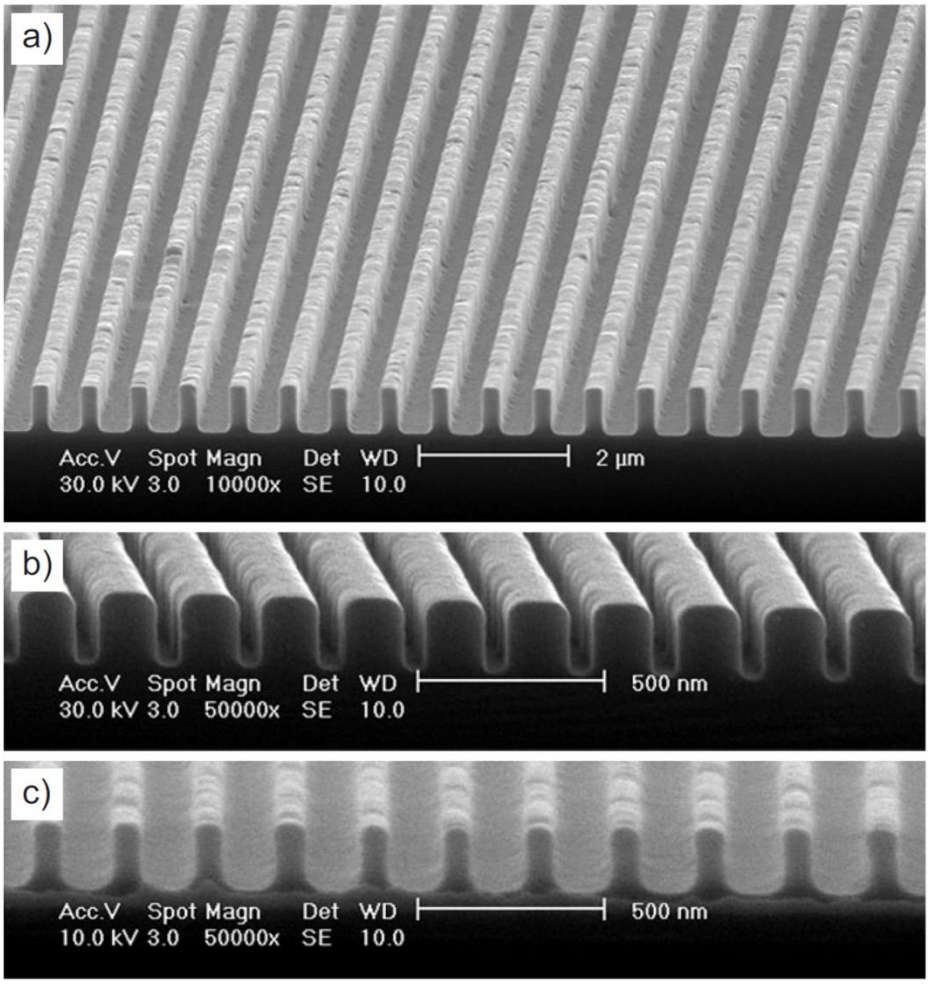

Figure 1.3 Various micro/nano-grating structures fabricated by nanoimprint lithography: (a) 250 nm linewidth polymer grating, (b) silicon nitride grating with 70 nm-wide trenches, and (c) 70 nm linewdith polymer grating replica imprinted using the mold shown in (b). (Figure source: Figure 8 in L. J. Guo, *Adv. Mater.*, 2007).

The micro/nano-grating structures (**Figure 1.3**[9]), defined as the two-dimensional parallel line arrays of orderly periods in micro/nano-scale dimension, deserve distinguishing attention over many top-down fabricable micro/nanostructures. Their simpler structures and thus easier fabrication methodologies but diverse functionalities assure the extensive usefulness and broad applicability for many fundamental components and applied devices.

Beginning with one of the most straightforward examples, the metallic nanogratings having invisible nanoscale line structures, when patterned on transparent substrates, can directly serve as the transparent conducting electrodes for various electronic devices ranging from light-emitting diodes (LEDs)[62, 63] to solar cells[64, 65]. Beyond those simple structure-oriented utilizations, the surface plasmon resonance (SPP) specifically found in nanoscale metallic grating structures, has extended their applications to optical instruments[66] and SPP-driven sensing devices[67, 68].

In the similar sense, as the geometrical parameters (e.g. period, height, width) of micro/nano-scale gratings are within the ‘sub-wavelength’ regime of light from UV to IR, the optical properties of incident light in desired wavelengths can be tuned, depending on the pattern geometry and structural configuration[69]. Therefore, these small-scale grating structures draw great interest for a variety of optoelectronic and photonic devices such as wire-grid polarizers[70, 71], anti-reflection films[72], and photonic color filters[73, 74]. As will be discussed in detail in Chapter 3.3[75], the sub-wavelength patterns particularly formed on the metal-insulator-metal (MIM) stack can manipulate the optical reflection or transmission in the way the natural optics system cannot realize. This character leads to the plasmonic ‘metamaterials’.

1.3 Goal and thesis outline

This thesis encompasses two big streams: (1) hierarchical hybrid assembly of complementary and multiscale nanostructures, and (2) development of continuous and scalable nanomanufacturing processes beyond paradigmatic nanofabrication methodologies. These bottom-up and top-down approaches both aim the same big goal: the **utilization of the functional micro/nano-architectures to useful devices in scalable way** which has been materialized in the following chapters;

Chapter 2 demonstrates the fabrication and characterization of hybrid architectures of ZnO NWs (ZNWs) grown on organized carbon nanotubes (CNTs). This functional hybrid system is implemented by a two-step CVD process involving CNT growth from a hydrocarbon source followed by ZNW growth using a Zn metal source. By taking a look at ZNWs and CNTs as separate functional building blocks, it will be emphasized how the hierarchically assembled ZNW-CNT hybrid structures can complement the drawbacks of each component and achieve synergetic functionalities. Detailed characterizations and analyses of the ZNW/CNT hybrid system are carried out, finalized by its application to photoelectric energy conversion.

Chapter 3 presents the continuous and scalable nanomanufacturing processes and their direct applications to optoelectronics and photonics. Beginning with the Roll-to-Roll (R2R) NIL, consistent efforts are made to increase the processing throughput and reduce the prerequisite steps while preserving the nanoscale resolution. We develop NanoChannel-guided Lithography (NCL) that utilizes the horizontal inscribing of cleaved molds, and Vibrational Indentation-driven Patterning (VIP) that makes use of the vertical

vibrating indentation of flat tools. It will be spotlighted that the preparation labor of master molds in terms of pre-fabrication and size/area can be significantly reduced from R2R to NCL, and even can be totally eliminated in VIP.

Chapter 4 describes the integrative practice of scaling up of functional nanoarchitectures in practical and feasible fashion, by combining the bottom-up grown functional hybrid nanostructures, novel top-down nanomanufacturing methods, and even conventional nanofabrication process. We first demonstrate the scalable fabrication of ZNW/CNT thin film devices through roll processing, toward anisotropic and rapid-responsive photodetectors and high photocurrent generators; then we introduce Photo Roll Lithography (PRL) that enables the continuous photolithographic fabrication of various micro/nano-scale features that are capitalized to transparent conducting electrodes and band-tunable IR filters.

Chapter 5 summarizes the findings and contributions of this work from perspective of scientific significance, engineering innovation, and practical usefulness, followed by the outlook for what may come next to broaden and deepen the reach of this work.

Chapter 2

Electrically Addressable Hybrid Assemblies of Zinc Oxide Nanowires and Carbon Nanotubes and Their Energy Conversion Characteristics

(*The work described in this chapter is from: J. G. Ok, S. H. Tawfick, K. A. Juggernauth, K. Sun, Y. Zhang, and A. J. Hart, Advanced Functional Materials 20, 2470 (Aug 2010)*.)

2.1 Three-dimensional hierarchy comprising complementary nanostructures

A typical and the simplest format of nanostructures may be 1-D nanowires (NWs) or nanotubes (NTs), where a large number (typically greater than 10^{10} cm^{-2}) of NTs or NWs is grown from the substrate surface typically catalyzed[76]. Depending on the characteristics of the structures and synthesis methods, the vertical alignment is achieved by crystallographic interactions with the substrate (e.g. ZNWs on sapphire[77]) and/or by crowding among the structures during the initial stages of growth (e.g. CNT 'forests'[78]).

Beyond the synthesis and applications of myriad 1-D nanostructures made of individual materials[76, 79], recent efforts have also explored the nanoscale heterostructures that combine the attributes of multiple materials. For example, "superlattice" nanowires (NWs) with alternating material segments are made by cycling the precursor chemistry during growth[80], or by sequential filling of porous

templates[81, 82]. Core-shell architectures are made by sequentially depositing nanoscale films on the outer surfaces of NWs, and these can function individually as photovoltaic cells[83, 84]. Branched structures are made by seeding the outer surfaces of NWs with catalyst to cause additional NWs or nanotubes (NTs) to grow in a simultaneous or sequential fashion[85-88]. Also, many types of metal, oxide, polymer, and semiconductor nanoparticles (NPs) have been placed on the outer surface of carbon nanotubes (CNTs)[20, 41, 43, 89-92].

While extensive research has demonstrated the unique size and structure-dependent properties of these and many other nanostructured building blocks, relatively few scalable approaches exist for creating functional hybrid architectures in three dimensions. In that context, a promising hybrid 3-D construct could be created using an array of vertically aligned and electrically conducting nanostructures as the substrate for a second type of nanostructure having complementary properties. Such hierarchically structured materials having a high density of nanoscale junctions between complimentary materials (e.g. conductors and semiconductors) along with large interfacial areas will be significantly beneficial for energy conversion and storage technologies[2].

2.2 Carbon nanotubes as templates for functional nanowire integration

CNTs[93, 94] are particularly attractive as scaffolds and templates for forming, connecting, and addressing other types of nanostructures since they are electrically conductive (all multi-wall CNTs (MWNTs) and statistically 33% of single-wall CNTs) and mechanically robust, and their surfaces can be modified chemically[20]. Further,

vertically aligned CNT “forests” can be grown on diverse substrates including silicon wafers[95], metal foils[96], and advanced fibers[97, 98]; and chemical vapor deposition (CVD) methods in combination with ordinary lithography can create patterned and molded[99] CNT forests over length scales ranging from micrometers to millimeters.

Previous approaches to fabricating complementary nanostructures involving CNTs include assembly of axial heterojunctions (e.g. Si[100], Ni[101], Ag[102], Au/Cu[82], or Sn[103]) and synthesis of nanostructures (e.g. MnO_2[104], GaN[105], Pt[106], and TiO_2[107]) on the surfaces of CNTs, but have practical limitations. Fabrication of CNT-based axial heterostructures often requires the step of template preparation (e.g. anodized aluminum oxide[82, 101, 102]) and later removal of the template. Additionally most methods to attach or grow other nanostructures onto CNTs have used solution chemistry which is advantageous due to its low temperature, yet is extremely slow and can undesirably alter the morphology of forests due to capillary force.

In the following sections, a more versatile and scalable method based on the step-wise CVD approach is introduced for building hybrid 3-D architectures of oxide NWs on vertically aligned CNTs. The hybrid structures are made by a two-step CVD process involving growth of vertically aligned CNTs from catalyst NPs on a silicon wafer, followed by catalyst-free NW growth on the CNT surfaces by thermal evaporation of a pure metal or metal oxide source in the presence of oxygen. Importantly, the CNTs withstand the oxidative growth process for NWs and establish electrical contact to the NWs. The NWs uniformly and conformally coat the surfaces of individual CNTs and CNT bundles throughout CNT forests, realizing 3-D hybrid nanoarchitectures.

2.3 Hybrid architectures of zinc oxide nanowires grown on carbon nanotubes

Zinc oxide (ZnO) NWs[108] have been investigated for applications including light-emitting devices[48] and vibrational energy harvesters[52]. ZnO NWs (herein called ZNWs) have a wide band-gap (≈3.37 eV), large exciton binding energy (≈60 meV), and a non-central symmetric wurtzite crystal structure. They also exhibit UV photoluminescence (PL)[48] and piezoelectricity[52]. However, despite recent progress in the synthesis of ZNW arrays by high temperature vapor-liquid-solid (VLS)[108] and vapor-solid (VS)[109], as well as by low temperature aqueous solution methods[110], the performance and practical feasibility of resulting ZnO-based devices is limited by the lengths of ZNWs which are typically no more than 1-20 μm. As a result, the power output of ZnO-based energy harvesters has been scaled up by stacking and wiring multiple substrates each holding NW arrays[111]. While this is effective, the relatively short NW length means that the volumetric performance of such a device is dominated by the substrate size, and device fabrication and assembly requires multiple delicate sequences. by photoconductive behavior and photocurrent generation of the hybrid material under UV illumination.

2.3.1 Synthesis of hybrid ZNW/CNT structures

In order to create hybrid NT/NW architectures by simultaneously or sequentially performing two CVD processes, the respective process conditions and structures must be chemically and thermally compatible. The following subsections will discuss several ZNW growth methods to find the right conditions to achieve hybrid array.

2.3.1.1 Vapor-Liquid-Solid (VLS) growth: incompatible growth conditions

We first attempted to grow ZnO/CNT hybrid structures following previously reported ZnO nanowire (ZNW) synthesis methods based on the high-temperature VLS process using Au catalyst[112]. In that process, ZNWs are grown using a ZnO/graphite powder mixture (1:1 mass ratio) as a source. The substrate is a-plane sapphire (i.e. Al_2O_3 $(11\bar{2}0)$) substrate having a 5 nm-thick Au film deposited by e-beam evaporation. The furnace is maintained at 950 °C, with 0.6-3 mbar pressure and 5-20 sccm air flow. CNTs are grown via the growth conditions described in **Appendix A**.

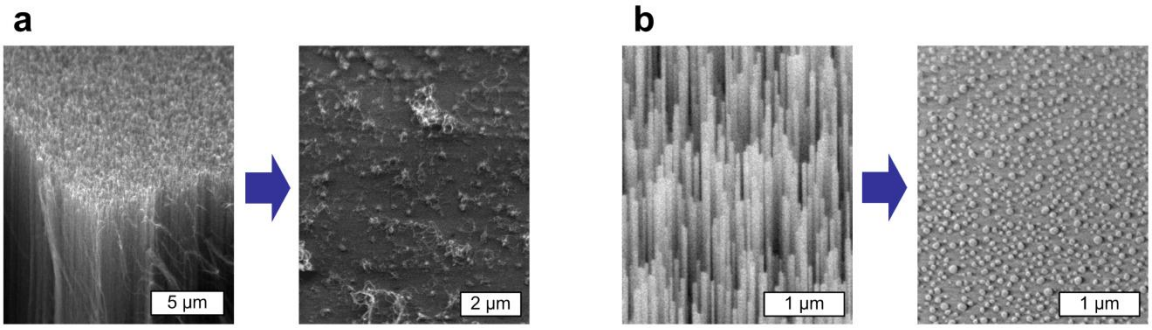

Figure 2.1 (a) Vertically aligned CNTs (left) were destroyed when they were exposed to process conditions suitable for ZNW growth by the VLS method (right). (b) VLS-grown ZNWs (left) vanished after they underwent the CNT growth process (right).

A CNT sample loaded in VLS-driven ZNW growth process is severely damaged because of the high-temperature oxygen environment (**Figure 2.1a**). Also, all ZNWs are destroyed after exposure to the CNT growth conditions at 775 ℃ under C_2H_4/H_2, presumably due to reduction of ZnO (**Figure 2.1b**). It is observed that the exposure of ZNWs to hydrogen even for less than 30 seconds at 775 °C destroys the ZNWs and leaves only catalyst nanoparticles on the substrate.

2.3.1.2 Hydrothermal growth: undesirable structural alteration

Hydrothermal growth of ZNWs can be conducted at very low temperatures (70-200 ℃) in liquid solution, and ZNWs were previously grown on CNTs by a hydrothermal method[113]; however, this process requires deposition of a nanocrystalline ZnO seed layer on the CNTs prior to ZNW growth, and needs a very long growth time (i.e. 12-48 hours). More importantly, surface tension forces from the ZnO growth solution inevitably cause elastocapillary aggregation of the CNTs,[114, 115] and this can undesirably alter the network morphology and prevent achievement of a well-organized hybrid array.

2.3.1.3 Vapor-Solid (VS) growth: compatible ZNW growth on CNTs

We find compatible conditions for growing ZNW/CNT hybrid structures in VS growth process using Zn metal source[116]. This is because the melting temperature (420 ℃) of Zn is much lower than ZnO (1975 ℃), and therefore a sufficient Zn vapor pressure for ZNW growth can be created at a much lower pressure. This in turn allows ZNW growth in an oxidizing low pressure environment at a temperature where the CNTs are not severely damaged by oxygen. **Figure 2.2** shows the apparatus for growth of hybrid ZNW/CNT materials, where a controlled gas flow (air and He) is supplied using digital mass flow controllers (MFCs), and pressure is precisely modulated via automated feedback pressure control system. Since the temperatures at source and substrate locations are of great importance in growth characteristics, we measure the temperature profile inside the chamber at growth temperatures (**Figure 2.3**). This temperature profile is also used when calculating the critical radii at different conditions as will be following

later. Air provides oxygen to form ZnO, while He enables independent regulation of the Zn vapor concentration and downstream transport for control of NW growth. Unless otherwise noted, the structures shown in this work were grown on MWNT forests for 20 minutes at 600 ℃ and 6 Torr, with a flow of 17.5 sccm air mixed with 20 sccm He.

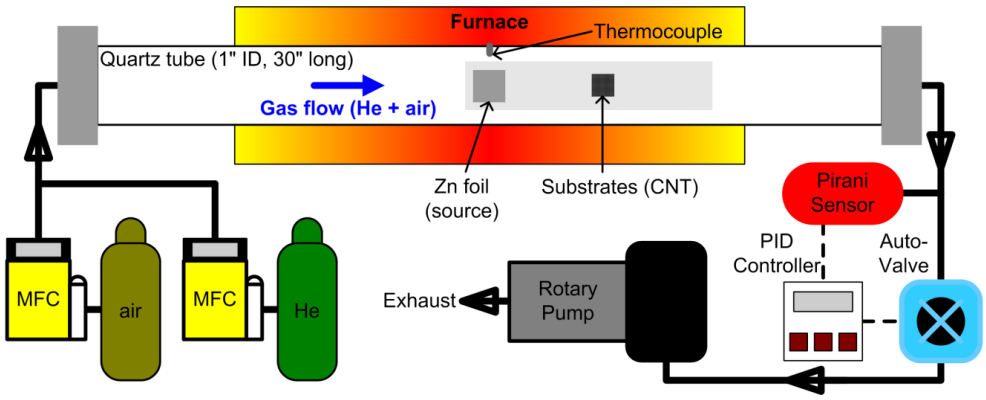

Figure 2.2 Schematic of the apparatus used for ZNW and CNT growth. For ZNW growth, a Zn foil in the center supplies Zn vapor as it is heated above its melting temperature under flowing air/He. The positions of the Zn source and CNT substrate are indicated by arrows. A CNT forest placed downstream serves as the substrate for ZNW growth. MFCs adjust the flows of air and He from the cylinders to the chamber inlet, and the pressure control system connected between the outlet of a chamber and the vacuum pump regulates the chamber pressure.

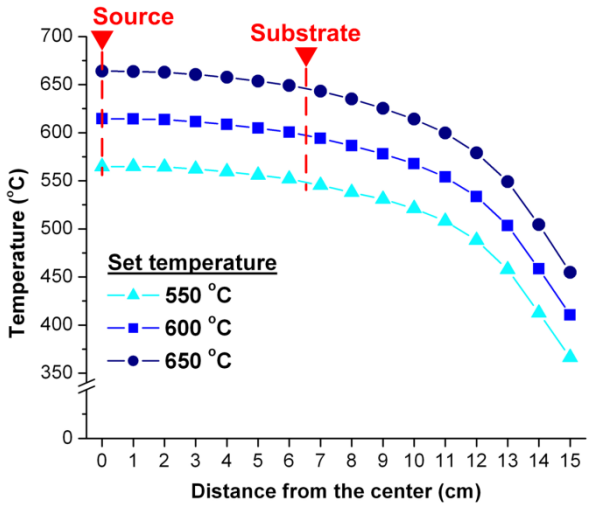

Figure 2.3 Temperature profiles measured along the central axis of the furnace tube at different setpoint temperatures.

2.3.2 Structural analysis

CNT forests which are initially black in color appear light gray to the naked eye after ZNW growth. The ZNWs grow uniformly and radially from the CNTs within the forest, as shown in scanning electron microscope (SEM) images (**Figure 2.4**). Notably, the aligned morphology of the CNTs is not disturbed by the ZNW growth process. Energy-dispersive X-ray spectroscopy (EDX) analysis (**Figure 2.5a**) also confirms that the structures grown on CNTs consist of Zn and O. Further, grazing incidence X-ray diffraction (GI-XRD, **Figure 2.5b**) confirms that the coating is crystalline ZnO.

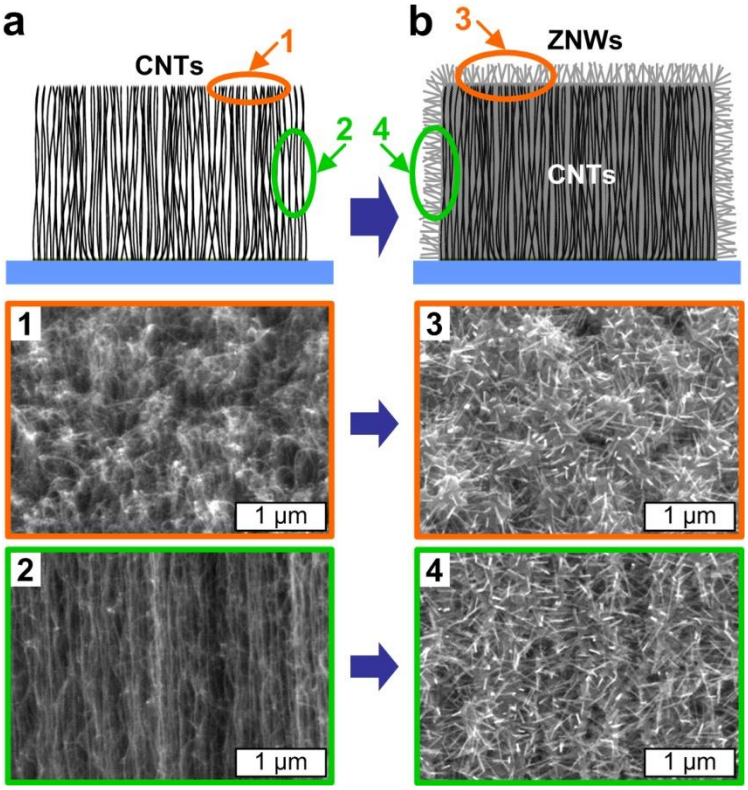

Figure 2.4 Growth of ZNWs on vertically aligned CNT forests. Schematic illustrations and SEM images show CNT forests before (a) and after (b) ZNW growth. SEM images were all taken from 45° tilted view, as indicated by arrows. ZNW growth is shown on both tangled CNT morphology of the top surface of the forest (1, 3) and the aligned CNT morphology of the forest sidewall (2, 4).

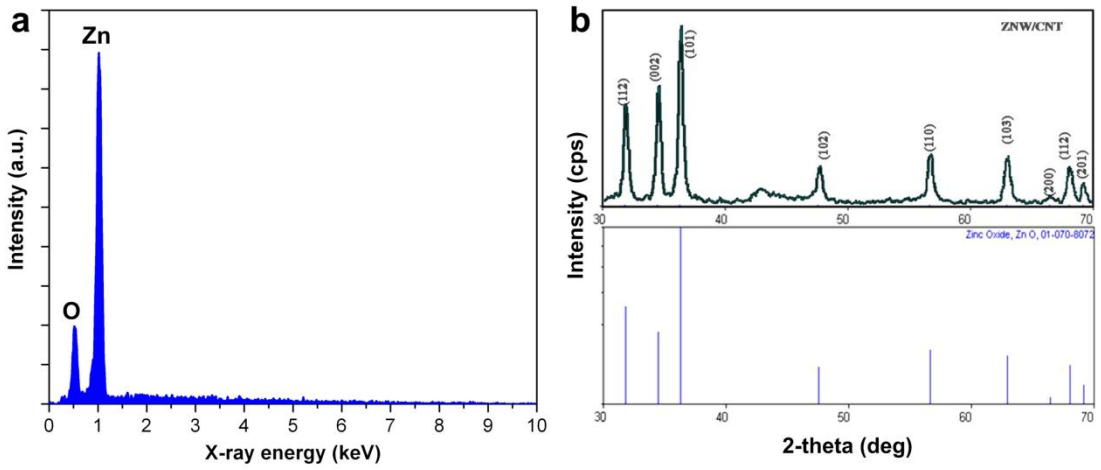

Figure 2.5 (a) EDX and (b) GI-XRD spectra taken from the top surface of a ZNW/CNT hybrid sample. EDX spectrum shows clear Zn and O peaks, and measured GI-XRD spectrum (top) reveals sharp peaks indicating highly crystalline samples which were identified as being the peaks corresponding to ZnO based on the ICCD card # for the line plot (bottom).

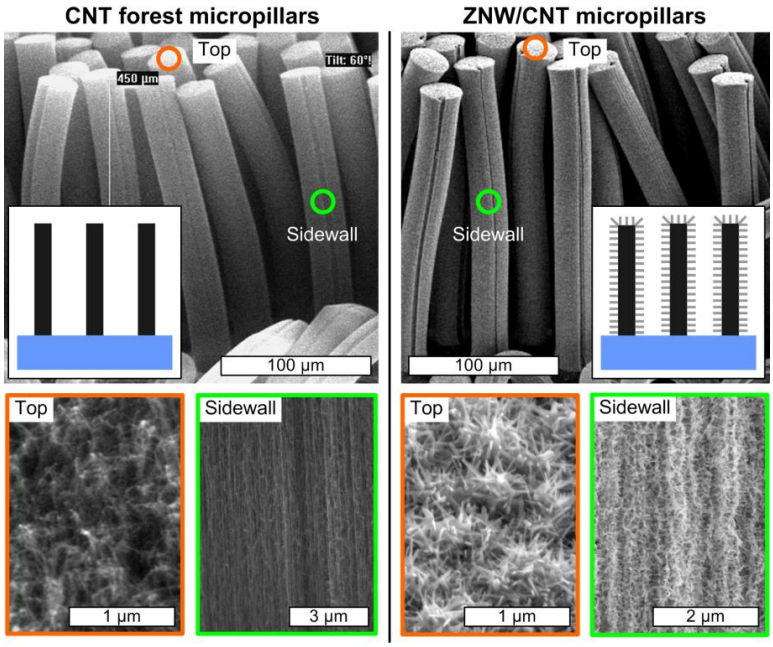

Figure 2.6 Growth of ZNWs on the arrays of CNT "pillars" grown from lithographically patterned catalyst: (a) before and (b) after ZNW growth. The enlarged views of top surfaces and sidewalls before and after ZNW growth clearly show that ZNWs are uniformly grown on the entire surface of CNT pillars. The insets to pillar images illustrating the schematics of each case vividly demonstrate the total surface area of a construct can be significantly increased after ZNW growth.

ZNW growth penetrates uniformly into the CNT forest to a distance of approximately 15 µm; thus, growing ZNWs on CNT microstructures that are first grown from lithographically patterned catalysts can achieve fully 3-D ZNW growth over areas. An example of this is shown in **Figure 2.6**, and demonstrates in principle that a wide variety of hierarchical designs can be built by our process.

Transmission electron microscopy (TEM) imaging of a hybrid ZNW/CNT bundle, shown in **Figure 2.7**, reveals precisely how the ZNWs extend from a nanocrystalline base layer that coats the CNTs. The ZNWs are approximately 300-500 nm long and 25-50 nm diameter, and notably this diameter is smaller than that of ZNWs typically grown on flat substrates from a powder source[77, 117]. As clearly observed in **Figure 2.7b**, the ZnO nanocrystals directly contact the outer walls of the CNTs. Lattice-resolved imaging and Selected-area electron diffraction (SAED) of an individual ZNW (**Figure 2.7c**) determines the lattice parameters $a \times \cos 30° = 2.8$ Å and $c = 5.2$ Å, which are consistent with the exact values of $a = 3.25$ Å and $c = 5.21$ Å [118]. Therefore, the ZNWs have the

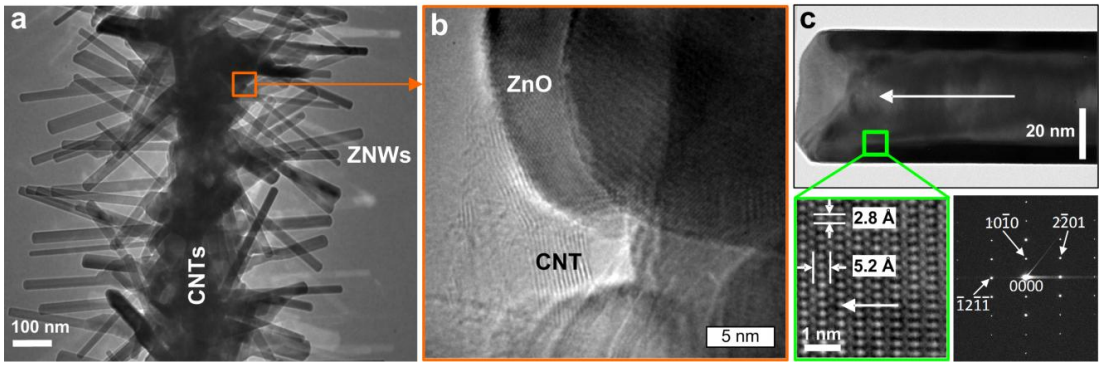

Figure 2.7 TEM images of a hybrid ZNW/CNT bundle: (a) plain view of ZNW/CNT bundle with core diameter ≈100 nm and ZNW diameters ≈10-50 nm; (b) close view of ZnO-CNT interface showing intimate relationship between graphitic MWNT walls and ZnO nanocrystals; (c) view of the tip of an individual ZNW. The lattice-resolved image and accompanying electron diffraction pattern of the ZNW in (c) verify the typical wurtzite crystal structure and c-axis [0001] growth direction.

expected hexagonal wurtzite ZnO structure, and grow along the c-axis in the [0001] direction which is energetically favored[46].

Additional imaging confirms the polydispersity of ZnO crystal orientation with respect to the CNTs. For example, **Figure 2.8** shows that ZnO crystals can nucleate directly on the CNT surface, and can also homogeneously branch at equal angles. In both cases, ZnO grows along the c-axis. Scanning TEM (STEM) with electron energy loss spectroscopy (EELS) (**Figure 2.8d**) discloses a sharp interface profile between ZnO (represented by the oxygen edge) and C, where the transition between O and C occurs completely within a distance of ≈2.5 nm. Establishing this intimate contact is necessary for transport across the ZNW/CNT interface, and thus is vital for devices and materials which combine the characteristic properties of multiple nanostructures.

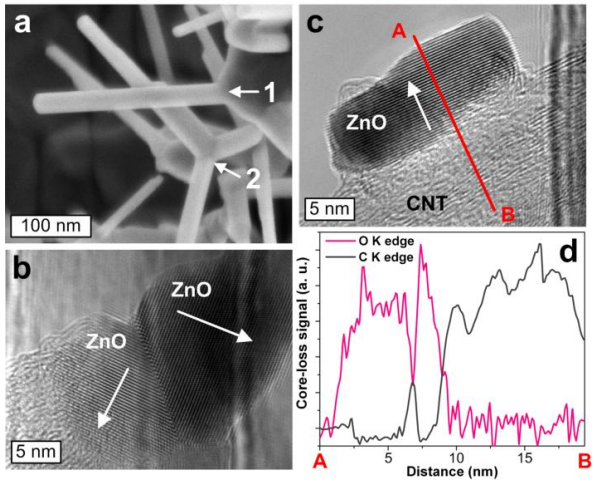

Figure 2.8 Growth of ZNWs from the interface of ZnO and a CNT. High resolution (HR)-SEM image (a) shows how ZNWs protrude (1) from a basal polycrystalline ZnO film that grows on the CNTs and how particular ZNWs meet at tetrahedral junctions emerging from the ZNW-coated CNT surface (2). TEM images demonstrate (b) tetrahedral and (c) normal growth of ZnO clusters on a CNT surface, which are to develop to ZNWs along the c-axis apparently distinguishable for each cluster by the lattice structure, as indicated by arrows. EELS line scan profiles (d) of C (using its K edge at 284 eV) and O (using its K edge at 532 eV) were taken along the A-B line across the ZnO-CNT interface marked in (c), indicating a clear and chemically stable boundary.

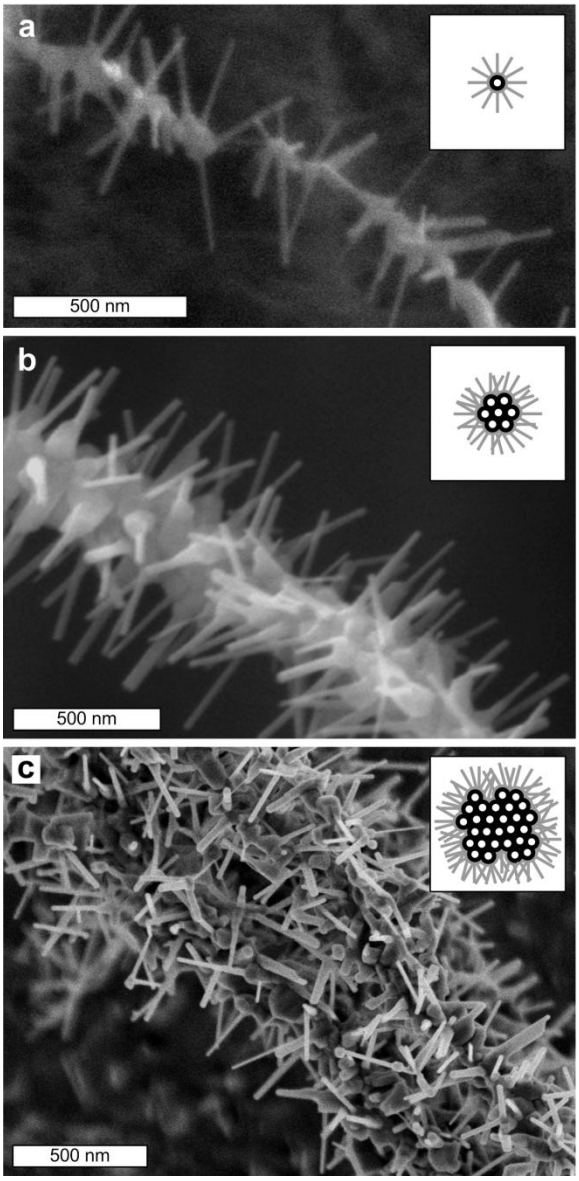

Figure 2.9 Conformal morphology of ZNW growth on the outer surfaces of aligned CNT assemblies: (a) a small group of CNTs, having initial diameter ≈20 nm; (b) a larger group, having initial diameter ≈100 nm and ZNW length ≈500 nm; and (c) a successively larger group having an irregular outer surface, showing how ZNW growth locally follows the morphology of the CNT substrate.

To assess how the outer surfaces of CNTs behave as a substrate for ZNW growth, ZNWs were also grown on isolated groups of CNTs, which were created by printing CNTs from a forest onto a copper grid prior to ZNW growth. SEM examination of these

structures (**Figure 2.9**) reveals that the CNT surfaces are typically coated by a polycrystalline ZnO film, and that ZNWs extend from this base layer. We find that individual CNTs (or very small groups) act as suspended "strings" that support ZNW growth, and larger groupings of CNTs are coated with radially oriented ZNWs on their outer surfaces. Because a CNT forest contains isolated and bundled CNTs of varied aggregation[119, 120], we expect similar ZNW/CNT structures are present throughout the CNT forest. Thus, controlling the diameter, density, and hierarchical organization of CNTs within a forest using known methods[121, 122] of controlling the CNT growth catalyst and CVD conditions can determine the relative density of ZNWs in the final hybrid material. So far, we have found that the ZNW diameter does not noticeably change with the size of the CNT bundle.

2.3.3 Photoluminescence analysis

PL spectroscopy provides additional insight into the crystalline quality of the ZNWs and the interactions between the ZNWs and CNTs. **Figure 2.10** shows the room-temperature PL spectra of our hybrid ZNW/CNT material, measured at 325 nm excitation. The PL spectra demonstrate a sharp and intense near-band edge UV emission peak at 397 nm, and a broad deep-level green emission peak at ≈550 nm. An as-grown, bare CNT sample does not show any PL sensitivity within the scanned wavelength range, which confirms the peaks shown in the ZNW/CNT sample are from the ZnO nanostructures. Also, the PL spectra of ZNW/CNT structures are invariant when the excitation wavelength is varied. The series of noisy peaks observed at around 450-490 nm is an artifact of the adhesive backing which was used to mount the ZNW/CNT sample to the

measurement substrate, as verified by the spectrum for the tape in **Figure 2.10**. The relatively sharp UV emission peak indicates that the sample is highly crystalline and of good structural quality. The broad decay observed here is also attributed to spectral overlap between the ZnO spectrum and artifacts from the mounting tape.

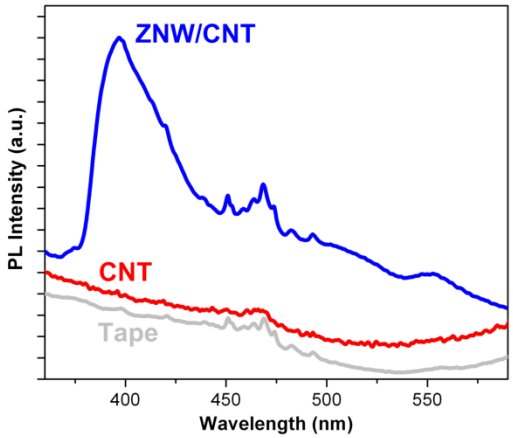

Figure 2.10 PL spectra of the top surfaces of a ZNW/CNT sample and a bare CNT sample having the same geometry (1 × 1 cm lateral dimensions) taken at excitation wavelength of 325 nm.

The deep-level visible wavelength (550 nm) peak is typically associated with defects in the ZnO structure[123] such as oxygen vacancies[124], and the broad peak centered at 525nm is attributed to the recombination of photogenerated holes with ionized oxygen vacancies[124]. It was also previously reported that the peak position of the green emission decreases from 520 nm to 506 nm with the diameter of ZNWs decreasing from 100 nm to 25 nm[108]. This change was attributed to a greater fraction of oxygen vacancies present in the thinner nanowires, because the greater relative surface area of thinner nanowires favored a higher level of surface and sub-surface oxygen vacancies. The broad peak for our sample is thus indicative of the polydispersity in ZNW diameters grown on CNTs. The PL characteristics of both the ZNWs and the underlying film, and

the characteristics of the ZNW-CNT interface, must be investigated further to fully understand the PL behavior of the hybrid material. Further, while not an absolute measure, the intensity ratio of the near-band edge adsorption peak in the UV range to the deep-level emission peak in the visible range provides an indication of the crystallinity of the system[123, 125]. Thus, a strong, intense UV peak and a weak, broad visible peak indicate that the hybrid ZNW/CNT structures are highly crystalline with low defects.

2.3.4 Mechanism of ZnO crystal growth on CNTs

It is evident that CNTs facilitate abundant formation of ZnO nanocrystals on their surfaces, which then form ZNWs by continued growth. According to the VS mechanism that has typically been studied for NW growth on flat substrates[126], Zn atoms adsorb onto the substrate and migrate to defect sites (e.g. pits, protrusions) where they accumulate to form crystalline clusters[70]. In our case, it is likely that ZnO nanocrystals form both on the surfaces of individual CNTs and in the nanoscale "grooves" between adjacent CNTs that are held closely by van der Waals interactions. Zn is oxidized to ZnO upon interaction with the substrate, and as more Zn and O atoms are stacked on each ZnO grain, ZNWs grow preferentially along the [0001] direction which minimizes the total surface energy. After the stable clusters form, NW growth proceeds in the energetically favored [0001] direction. Previous research suggests NW growth is primarily fed by adsorption of adatoms onto the sidewalls of each NW and subsequent diffusion to the tips, where crystallization possibly occurs at advancing step edges arising from screw dislocations[86, 127-130]. If diffusion on the NW surface is much faster than self-nucleation of clusters on the NW surface, the NW lengthens much faster than its diameter

increases, and this is a favorable condition for growth of long and slender NWs[131, 132].

Consistent with this mechanism, at short growth times (e.g. 5 minutes), we observe short ZNWs along with isolated ZnO nanocrystals on the CNTs (**Figure 2.11**). At longer times (20 minutes as shown in **Figures 2.4 and 2.9**), the ZNWs are longer and the CNT surfaces are fully covered by a polycrystalline ZnO film. We expect that ZNWs that grow at shallow angles with respect to the CNT surface are eventually incorporated in the ZnO film that coats the CNTs, and ZNWs that grow at larger angles to the substrate remain freestanding. As shown in **Figure 2.8a**, tetragonal and/or tetrahedral branching[133] of the ZnO also occurs.

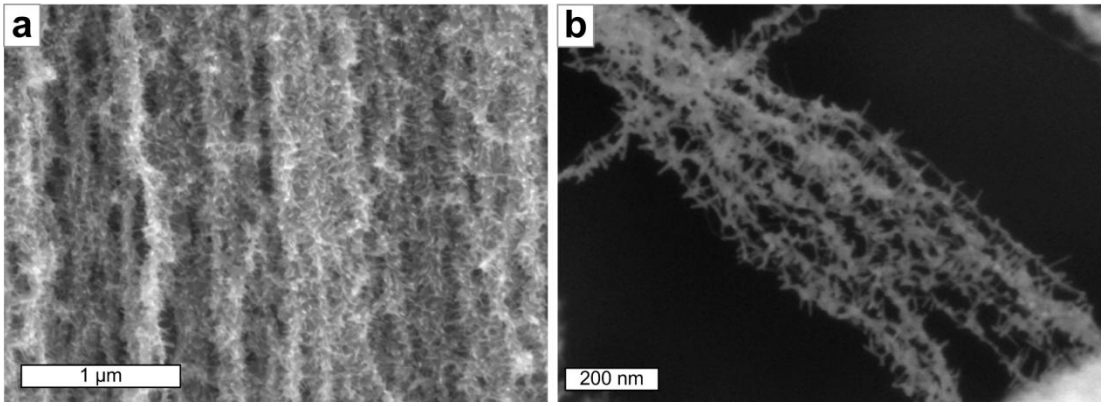

Figure 2.11 Conformal morphology of ZNW growth on the outer surfaces of aligned CNT assemblies: (a) a small group of CNTs, having initial diameter ≈20 nm; (b) a larger group, having initial diameter ≈100 nm and ZNW length ≈500 nm; and (c) a successively larger group having an irregular outer surface, showing how ZNW growth locally follows the morphology of the CNT substrate.

Thus, the mechanism of ZNW growth on CNTs is analogous to that on flat substrates, and the initial formation of ZnO nanocrystals can be further understood by a classical model of nucleation and growth[134]. Zn atoms adsorb and diffuse on the CNTs, forming ZnO nanocrystals that must exceed a critical size that dictates a decrease in their

total free energy with continued growth. In other words, for a cluster of given size to be stable, its growth must create a net decrease in total free energy. This critical size is estimated by calculating the first derivative of the total free energy (ΔG) of a nanocrystal with respect to its radius R, as fully described in **Appendix B**. Modeling the cluster as a hemisphere on a flat substrate and considering the change in surface energy due to nano-scale curvature of the cluster (**Figure 2.12**), we find the free energy of formation (ΔG) is

$$\Delta G = \pi\left(3.3\sigma_1 + \sigma_{12}\right)R^2 - \frac{2\pi kT}{3v}\ln\left(\frac{P}{P_\infty}\right)R^3 \qquad (2\text{-}1)$$

Here, σ_1 is the cluster surface energy (ZnO), σ_{12} is the cluster-substrate interface energy (ZnO-C), v is the atomic volume, k is Boltzmann's constant, T is the absolute temperature of the substrate, P is the pressure of the vapor precursor (determined from the source temperature), and P_∞ is the equilibrium vapor pressure above the bulk surface at T. Also, by taking the first derivative of Equation (3-1), we obtain that the minimum stable radius R^* (the critical radius) is

$$R^* = \frac{(3.3\sigma_1 + \sigma_{12})v}{kT\ln(P/P_\infty)} \qquad (2\text{-}2)$$

A critical limitation and simplification of this model is that the cluster contains only a single species; however, in our case Zn must interact with O to form ZnO, and it is not precisely known when and where Zn is oxidized during the atomic processes of adsorption, diffusion, and cluster formation. Further, all atoms needed to form a crystal of stable size do not arrive simultaneously. Thus, the dynamic stability of a crystal is affected by the diffusion and residence times of the adatoms on the substrate, which are not known. This model also does not consider the effects of substrate (CNT) curvature

and/or the nanoscale geometry of the nucleation sites, and the geometry of the ZnO-CNT interface will certainly determine the contact area per unit volume, and hence alter the contribution the ZnO-CNT interface to the total free energy.

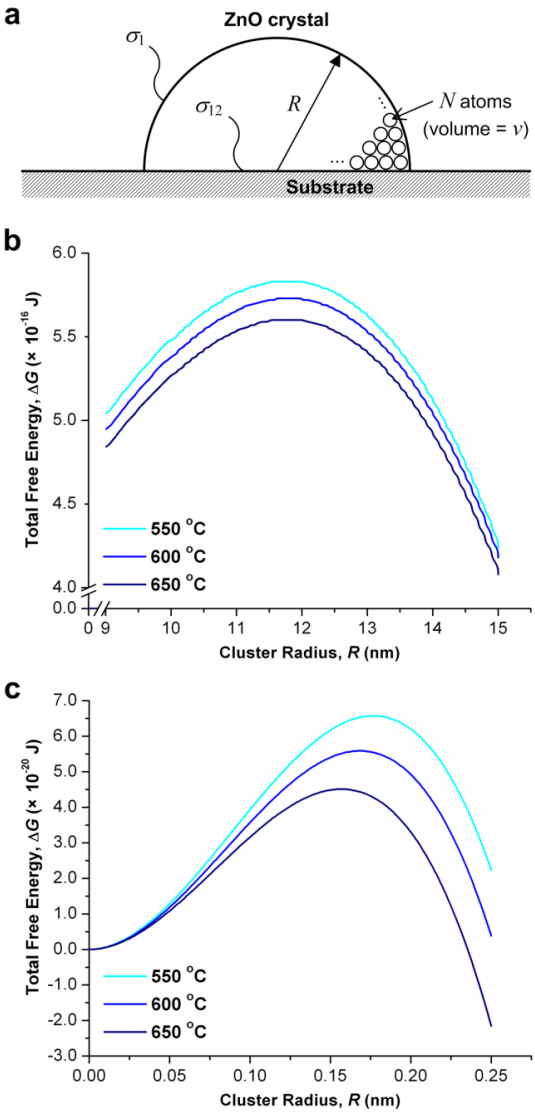

Figure 2.12 Analytical model of heterogeneous nucleation and growth of ZnO nano-clusters: (a) diagram of a hemispherical Zn (or ZnO) cluster being formed on a substrate surface, having a diameter of R and consisting of N Zn atoms; plots (b) and (c) showing ΔG versus R at different temperatures for the two limiting cases discussed in the text. Plot (b) applies when Zn vapor directly adsorbs to form Zn clusters which are later oxidized, and (c) applies when Zn vapor forms ZnO clusters immediately.

With these limitations in mind, we estimate the critical radius R^* for two limiting cases: (I) where Zn vapor adsorbs to form Zn clusters which are later oxidized, and therefore P_∞ is the vapor pressure of Zn at the substrate temperature; and (II) where Zn vapor forms ZnO clusters immediately, and therefore P_∞ is the vapor pressure of Zn above ZnO at the substrate temperature. Substituting these and other parameter values[135-138] for our growth conditions as described in **Appendix B**, we get $R^* \approx 11.8$ nm for case (I) and ≈ 0.17 nm for case (II). Also, as T increases and temperature-dependent parameters such as surface energy and vapor pressure therefore also change accordingly, ΔG decreases for both cases (**Figures 2.12b and 2.12c**).

According to these calculations, the critical cluster size is substantially smaller than the ZNW diameter observed in TEM images. Therefore, we can make two conclusions: (1) the cluster size does not directly determine the ZNW diameter, and (2) VS growth of ZnO on CNTs reflects competition between NW growth and polycrystalline film growth. As time proceeds, the balance between NW and film growth depends on the tendency to form new crystals via continuous nucleation, and the tendency to grow NWs from the initial crystals as their size increases, and clusters of a certain size much larger than the critical size for nucleation emerge in the [0001] direction as NWs.

Further, we observed that film growth dominates over NW growth as the temperature increases (**Figure 2.13**). This corroborates the analytical prediction that the free energy of cluster formation ΔG decreases as T increases; an increased tendency to form stable clusters would result in decreased mobility of Zn and/or ZnO atoms to the

tips of NWs. In the future, measurement of the growth kinetics and diameter and length distributions of ZNWs under different process conditions will shed more light onto the factors controlling the nucleation density and size of the nanostructures on CNTs.

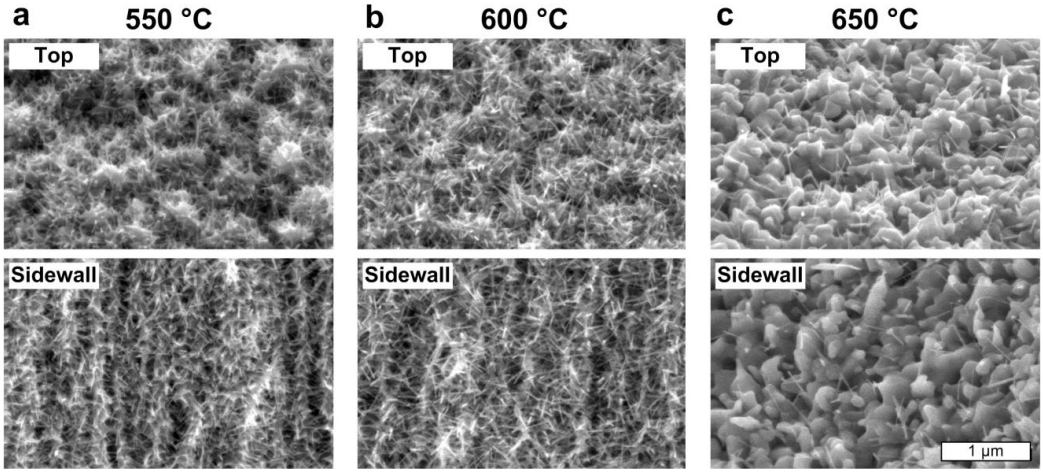

Figure 2.13 ZNWs grown on CNT forests at different furnace setpoint temperatures: (a) 550 ℃, (b) 600 ℃, and (c) 650 ℃.

2.3.5 Yield and scalability

Owing to the high surface area of the CNTs, the hybrid ZNW/CNT configuration increases the yield of ZNWs by a factor of 10^1-10^3 as compared to growth on a flat substrate of the same area. Also, the large mass ratio of ZNWs to CNTs, which will be imperative to achieve high performance for energy conversion applications, can in principle be tuned by over a broad range (~10^2-10^4) by controlling the CNT and ZNW dimensions within reasonable bounds. All these calculations are based on measurements of ZNW dimensions from TEM images.

To quantify how our ZNW-CNT hybrid structures offer a significantly higher yield of ZNWs, as compared to a ZNW array grown on a flat substrate, we calculate the population of ZNWs grown on (1) a flat substrate and (2) an orderly, cylindrical CNT

bundle array. We consider that the CNT array has a distribution of bundle sizes (see **Figure 2.9** for example), and we know that the outer surface of the bundle is the substrate for ZNW growth. Thus, we compare here CNT arrays with different bundle diameters.

Figure 2.14 depicts schematics of each case with average geometrical parameters whose values are chosen based on our studies. For simplification, a ZNW is assumed as a cylinder, and a CNT bundle is regarded as a cylindrical solid structure where ZNWs grow only on the outer surface. For ZNWs, the average length (l), diameter (d), and spacing (s) were approximated based on our TEM images of the ZNW/CNT hybrids. Three different values of the diameter of CNT bundles (D) are chosen corresponding to SEM images of bundles shown in **Figure 2.9**. The CNT bundle spacing (S) is chosen to allow adjacent CNT bundles with ZNWs on surface to be placed without any overlapping to maintain geometrical compatibility.

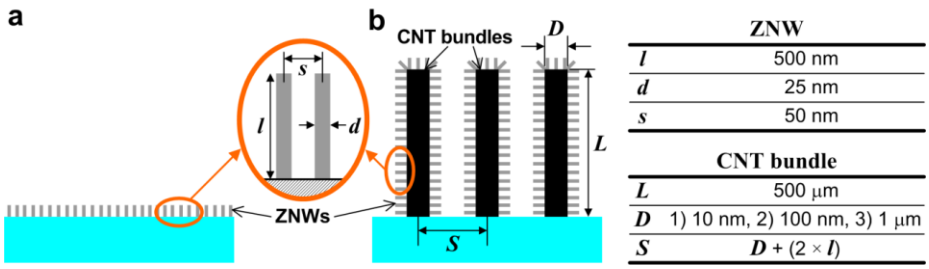

Figure 2.14 Comparative illustrations of the yield of ZNWs in (a) a flat substrate and (b) a CNT array, and the gemoetrical parameters defined for the calculations following.

Table 2.1 Calculated number densities of ZNWs grown on CNT forests with different bundle diameters, denoted as the number of ZNWs per unit area of the Si substrate.

ZNWs on flat substrate (Figure 2.14a)	**ZNW-CNT hybrid structures** (Figure 2.14b)		
	D = 10 nm	D = 100 nm	D = 1 μm
4.00×10^{10} cm^{-2}	6.16×10^{11} cm^{-2}	5.19×10^{12} cm^{-2}	1.57×10^{13} cm^{-2}
Yield ratio (hybrid:flat)	15:1	130:1	393:1

Table 2.1 summarizes the total numbers of ZNWs grown on an equal unit area (i.e. 1 × 1 cm) for (a) a ZNW array on a flat substrate and (b) a hybrid ZNW-CNT array. As the CNT construct can provide high surface area, the yield of ZNWs is higher by a factor of 10^1-10^3, depending on the diameter of CNT bundles. The CNT length is fixed to 500 µm in all cases.

When utilizing this ZNW-CNT hybrid material to a nanoscale energy conversion device such as an electrochemical battery or solar cell, the mass ratio of ZNWs to CNTs will also be an important factor to determine the energy density, for example, with the unit of [Wh/kg]. **Figure 2.15** plots the mass ratio of ZNWs to CNTs versus the CNT bundle diameter *D* with different ZNW lengths, demonstrating that our hybrid architecture is beneficial to achieve high energy density per unit area of substrate. Therefore, this material may present a significant performance advantage if intimate electrical contact is established between the CNTs and ZNWs at a high density and over a large area, as will be investigated in details in the following section.

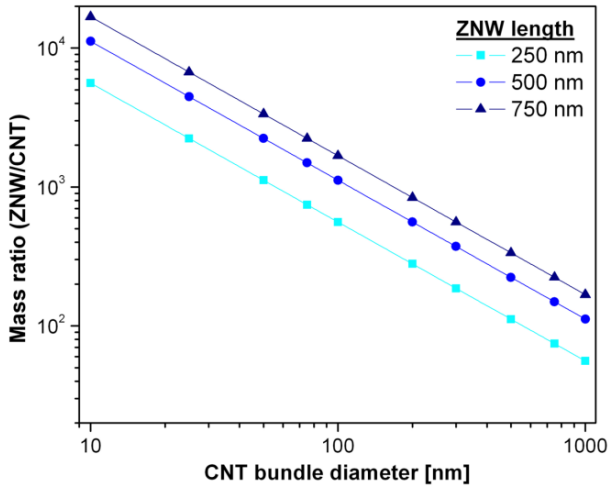

Figure 2.15 Calculated mass ratio of ZNWs to CNTs in the hybrid architecture showing the increase in the yield of ZNWs and mass ratio (ZNW to CNT) achievable by introducing the ZNW/CNT hybrid architecture.

2.4 ZNW/CNT thin films as electrically addressable energy conversion devices

2.4.1 Fabrication and characterization of anisotropic ZNW/CNT thin films

To investigate the electrical characteristics of the ZNW/CNT hybrid architecture, and to demonstrate its energy harvesting properties, we fabricated thin film devices comprising laterally-aligned films of the hybrid material with integrated electrical contacts. **Figure 2.16a** depicts the fabrication procedure described in detail in **Appendix A**. Briefly, CNTs were grown from lithographically-patterned catalyst, then the CNTs were "rolled" to form a horizontally aligned CNT (HA-CNT) sheet[139], then Au electrodes were deposited using shadow masks, and finally ZNWs were grown on the CNTs.

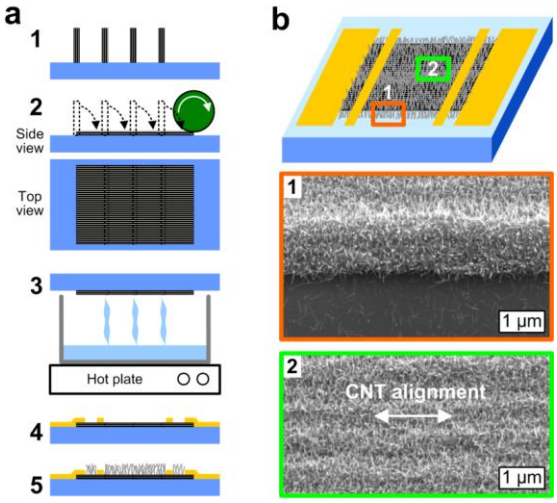

Figure 2.16 Fabrication and characterization of a hybrid ZNW/CNT film for measurement of electrical and photoelectric properties. Schematic (a) depicts (1) CNT forest blade growth from lithographically patterned catalyst; (2) and (3) folding of CNTs to horizontal orientation using mechanical rolling and surface tension; (4) deposition of Au contacts by using shadow mask pattern; and (5) ZNW growth. Schematic of the final device (b) is accompanied by SEM images of ZNW morphology on CNT sheet with ≈1.5 µm thickness.

As seen in SEM images of the device (**Figure 2.16b**), ZNWs selectively grow on the CNTs in comparison to the surrounding substrate (i.e. smooth SiO_2/Si surface), confirming that (consistent with the VS mechanism) the substrate surface roughness plays an important role in heterogeneous nucleation[140]. This attribute is further advantageous in self-patterning ZNW growth based on the substrate topography.

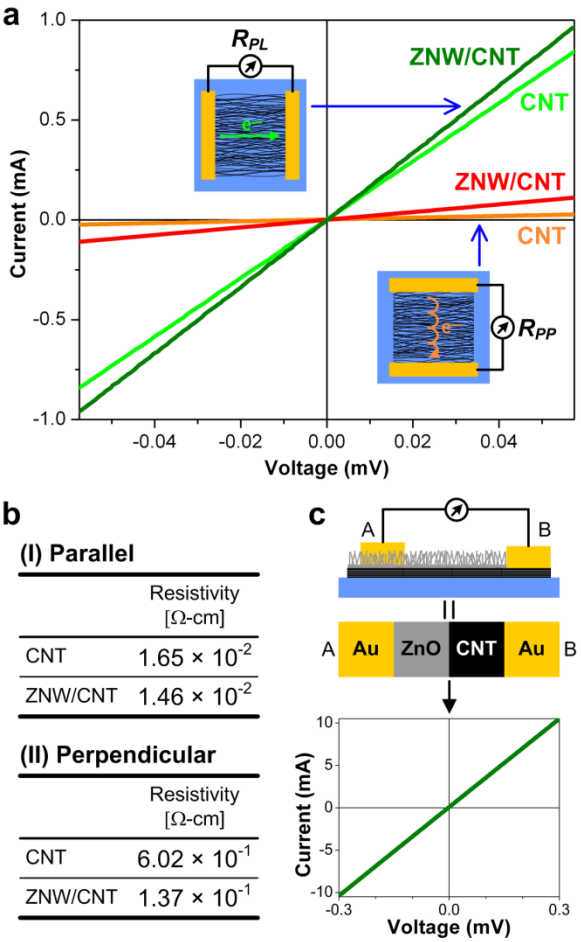

Figure 2.17 Anisotropic electrical characteristics of ZNW/CNT sheets: (a) *I-V* curves before and after ZNW growth in the parallel (along the CNTs) and perpendicular (normal to the CNTs) configurations; (b) resistivity data, based on *I-V* measurements and sheet geometry, before and after ZNW growth; and (c) *I-V* measurement after an additional Au electrode is deposited on top of the ZNW layer, as shown in the accompanying schematic. Insets to (a) schematically show electron transport mechanism through aligned CNTs in parallel and perpendicular directions.

The electrical characteristics of the laterally-aligned films were measured using a 4-point method before and after ZNW growth, both parallel and perpendicular to the CNT alignment direction. The *I-V* curves are shown in **Figure 2.17a**. As expected from the anisotropic organization of the film, the electrical conductivity is significantly larger along the CNT axis ("parallel" device), than perpendicular to the CNT axis ("perpendicular" device). This unique anisotropic behavior represents transport where the resistance is dominated by the characteristics (e.g. wall structure and defects) along individual CNTs in the parallel configuration; and primarily by electron hopping[141] between CNT sidewalls in the perpendicular configuration.

The electrodes are deposited prior to ZNW growth and therefore contact the CNTs "under" the ZNWs. Because the anisotropic electrical conductivity of the film persists after ZNW growth, we conclude that the ZNW growth process does not alter the properties of CNTs. This corroborates our TEM images (**Figure 2.7**) that show intimate contact between the graphitic CNT walls and ZnO nanocrystals. Further, the electrical conductivity in both directions is slightly higher after ZNW growth, demonstrating that the ZnO nanostructures bridge the high-resistance contacts between neighboring CNTs, and can also possibly mitigate resistance at serious defects (i.e. kinks, breakages) along individual CNTs. Accordingly, the relative decrease in resistivity after ZNW growth (**Figure 2.17b**) is much larger (77%) for the perpendicular device than the parallel device (11%). The resistivity of ZNWs was previously measured to be 3.5×10^6 Ω-cm[51], which is several orders of magnitude higher than measured for the CNT sheet in either direction. Therefore, even though the electrodes are connected by a continuous path of ZnO because the CNTs are coated with a thin ZnO film at the base of the NWs, electrical

transport through the ZnO has a negligible contribution to the overall transport through the device.

We also measured the electrical transport across the ZnO/CNT interface by depositing a fifth Au electrode on top of the device after ZNW growth, resulting in a transport path through a series path of Au-ZnO-CNT-Au. The linearity of this *I-V* curve (**Figure2.17c**), in conjunction with the linearity of the *I-V* curves through the CNTs (Au-CNT-Au; **Figure2.17a**) demonstrates Ohmic contact between ZnO and the CNTs. In other words, the ZnO and CNTs form a nonrectifying junction, which is expected[142] because MWNTs, which are metallic regardless of their chirality, have a lower work function (4.5-5.0 eV[143, 144]) than n-type semiconducting ZnO (5.3-5.4 eV[145]).

2.4.2 Photoconduction and photocurrent generation of the ZNW/CNT hybrids

Finally, we demonstrate that the ZNW/CNT hybrids are highly attractive building blocks for new energy conversion materials that couple the attractive properties of ZNWs and CNTs. As an initial step in this direction, the hybrid ZNW/CNT films demonstrate photoconductive behavior and photocurrent generation, with rapid dynamics, upon exposure to UV illumination. These tests were performed using the ZNW/CNT film with Au contacts in the parallel device configuration, and the intensity of illumination was controlled by changing the distance between the UV source and the device. An identical CNT sheet without ZNWs did not exhibit any of these photoresponsive characteristics. The configuration for these measurements is shown schematically in **Figure 2.18a**.

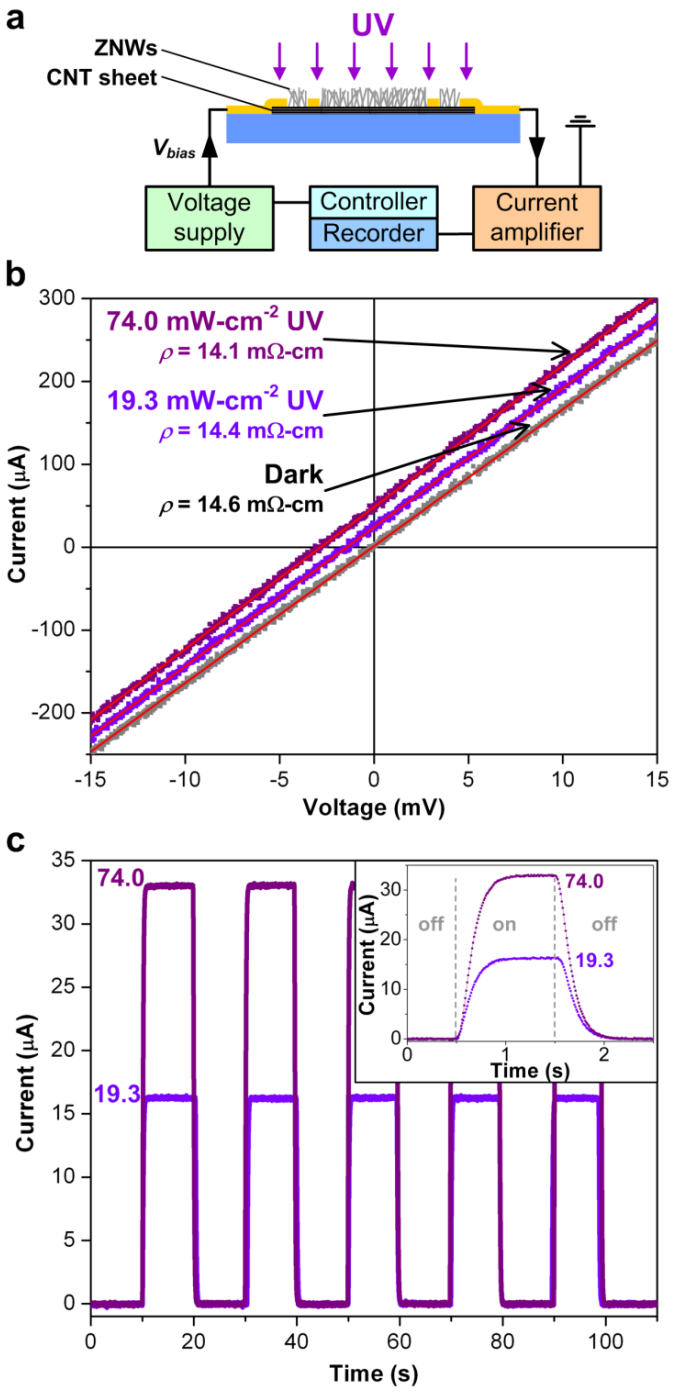

Figure 2.18 Photoelectric behavior of a hybrid ZNW/CNT thin-film device in the parallel configuration: (a) measurement configuration; (b) *I-V* curves upon 365 nm UV irradiation at different intensities; (c) time-resolved photocurrent generated by turning on and off the UV light without applied bias. Inset to (c) shows a single curve during 1 second UV exposure, demonstrating rapid photoresponse (≈0.5 seconds).

2.4.2.1 Photoconductive behavior

First, in **Figure 2.18b**, we see that the resistivity of the ZNW/CNT film decreases slightly upon UV illumination, and the magnitude of this decrease is proportional to the UV intensity. This is well-known as the photoconductive effect[49], and the relatively small magnitude of the decrease in resistivity is consistent with our understanding that the electrical transport through the device is dominated by conduction through the underlying MWNTs which are metallic. Based on previous studies of ZnO photoconduction[49, 146, 147], we suggest that ambient O_2 adsorbs on the ZNW surfaces and associates with free electrons from the n-type ZnO. When the device is illuminated with a photon energy exceeding the ZnO band gap (≈3.37 eV), electron-hole pairs are generated in ZnO. The photogenerated holes migrate to the surface along the potential slope created by band bending and discharge the adsorbed O_2 ions,

$$h^+ + O_2^-(ad) \rightarrow O_2(g) \qquad (2\text{-}3)$$

The remaining free electrons enhance the conductivity of ZnO, and this marginally enhances the ZNW/CNT hybrid conductivity.

Previous photoconductivity measurements of individual ZNWs made electrical contacts directly to the ZnO, which in combination with the low conductivity of ZnO results in significant photoconductive gains[146]. However, the comparatively slight enhancement of the ZNW/CNT conductivity in our study suggests that the additional free electrons are donated from the ZnO nanostructures to the CNTs, and these electrons have a measurable yet small effect on the CNT conductivity. Consistent with the photoconduction mechanism, there is no measurable change in conductivity when the

ZNW/CNT device is exposed to UV light in vacuum (**Figure 2.19**). Therefore, in the absence of oxygen interaction on the surface of ZnO, the photogenerated electron-hole pairs recombine within the material and do not contribute to conduction.

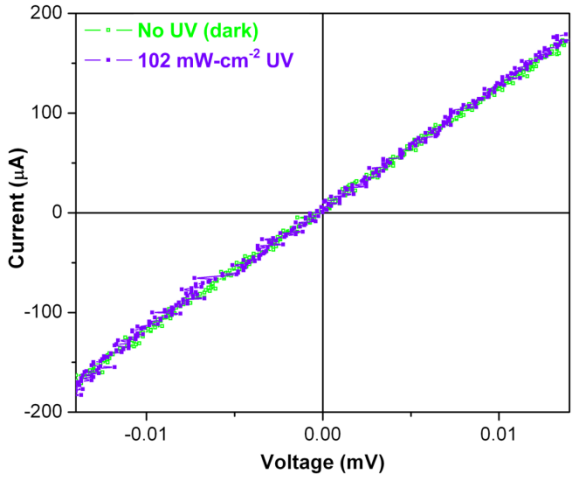

Figure 2.19 *I-V* measurements of the ZNW/CNT hybrid film in vacuum environment. UV illumination has a negligible effect on the conductivity in vacuum.

2.4.2.2 Photocurrent generation and response dynamics

The ZNW/CNT film also produces a distinct electrical current when illuminated under zero bias, indicating that the hybrid material itself operates like a photovoltaic cell (**Figure 2.18c**). We suggest this current is generated by continuous turnover of the oxygen-mediated photoconduction mechanism. In other words, continuous adsorption and desorption of ionized surface oxygen collects photogenerated holes from the surface of the ZnO (the anode), while electrons flow into the CNTs (the cathode) and are collected by the circuit. Notably, this current is absent in vacuum, confirming that ambient oxygen is necessary to generate the photocurrent. The high surface area of our device increases the intensity of the photocurrent, even though the kinetics of oxygen adsorption and desorption may be slow. The external quantum efficiency (EQE) of this

behavior is approximately 1 %, at a UV intensity of 19.3 mW-cm^{-2}. Under these conditions, the device generates 163.2 mA-cm^{-2} and 0.97 mV, as measured across the Au electrodes deposited at opposite extents of the film.

The ability of the hybrid material to generate a photocurrent through the CNTs at zero bias indicates that electrons from the semiconducting (n-type) ZnO structures can readily transport to the metallic CNTs due to the ohmic contact between the CNTs and ZnO. Upon exciton generation inside the ZnO, photogenerated electrons from ZnO flow into the CNTs. The direction of the photocurrent is determined by the contact resistances between the Au electrodes and the ZNW/CNT film. The photocurrent flows to the electrode with the lowest contact resistance, and the direction of current flow does not change when the connections to the measurement circuit are reversed.

Finally, the photoresponse dynamics are studied by switching the UV light on and off, with the device in air. The rates of increase and decay of the photocurrent are strikingly rapid, as it takes less than 0.5 second for the current to decay to below 1% of the steady illumination value at 0 V bias (inset to **Figure 2.18c**), and less than 1 minute to decay at 300 mV bias (data not shown). Comparatively, UV photodetectors based on individual ZNWs exhibit response times ranging from seconds to minutes[51, 146, 148], and photodetectors using polycrystalline ZnO thin films exhibit response times ranging from a few minutes to several hours[147]. The rapid response of the ZNW/CNT hybrid is attributed to the intimate contact between the ZNWs and CNTs, which enables rapid dissipation of carriers that remain in the ZnO after the illumination is turned off. Hence, our material combines the large-area scalability of a thin film with the rapid response observed with individual NWs.

2.5 Summary

We have demonstrated a suite of versatile methods for building hybrid architectures of ZNWs on aligned CNTs. The inherent scalability of the two-step CVD process, as well as the rolling and patterning methods used to fabricate functional hybrid sheets, suggest it will be possible to scale this process for efficient manufacturing. The CNTs are a true 3-D substrate that makes uniform and distributed electrical contact to the ZNWs, thereby overcoming an important obstacle to the use of aligned NWs that have been previously demonstrated on flat substrates. The UV-induced photoconductive behavior and photocurrent generation of the ZNW/CNT hybrids are examples of how this architecture may be used to efficiently couple the attractive properties of NWs in large numbers. These may take advantage of the utility of ZNWs in dye-sensitized solar cells, gas sensors, and piezoelectric devices. Our process is also scalable to virtually any CNT configuration, ranging from isolated CNTs in electronic devices, to bulk configurations like tangled films ("buckypapers") and bulk powders. These are important steps toward next-generation nanoscale energy conversion and storage technologies.

Chapter 3

Continuous and Scalable Nanomanufacturing Technologies and Their Direct Application to Optoelectronics and Photonics

3.1 Manufacturing in small scale: demands and challenges

There has been an increasing demand for sub-wavelength periodic structures in optoelectronics and photonics[149-151]. Fabrication of such micro/nano-scale structures has widely leaned on the optical lithography due to its reliability and matured protocols[8, 152]. The principle of photo- or e-beam lithography, however, makes it difficult to scale the faithfully fabricable feature sizes down to sub-wavelength regime because of the nature of light diffraction or beam scattering. Also, its low throughput and limitation in scalable processing address the challenges to meet the emerging needs of large-area and low-cost manufacturing of practical micro/nano-engineered devices. In this regard, a series of efforts have been made to find alternative methodologies to afford the sub-wavelength scale fabrication, such as laser interference lithography[153], plasmonic nano-ruling[154], and block copolymer-assisted patterning[155, 156].

In particular, NanoImprint Lithography (NIL)[9] provides an unique solution to achieve sub-10 nm spatial resolution with high precision and great reproducibility. In

NIL (**Figure 3.1a**), a rigid 'mold' containing the counter-pattern imprints the desired pattern onto the targeted substrate under controlled pressure typically aided by heat and/or UV illumination. Since NIL is purely based on mechanical deformation, it is free from optical disturbances, thereby readily producing sub-micron period patterns. For example, NIL enables the fabrication of nanoscale metal gratings that can act as transparent electrodes[62, 63] and enhanced charge-collecting layers in photovoltaics[64, 65, 157]. NIL can also define such nanogratings in the metal-insulator-metal (MIM) stack to realize a new type of color filters useful for displays applications[69, 73, 158].

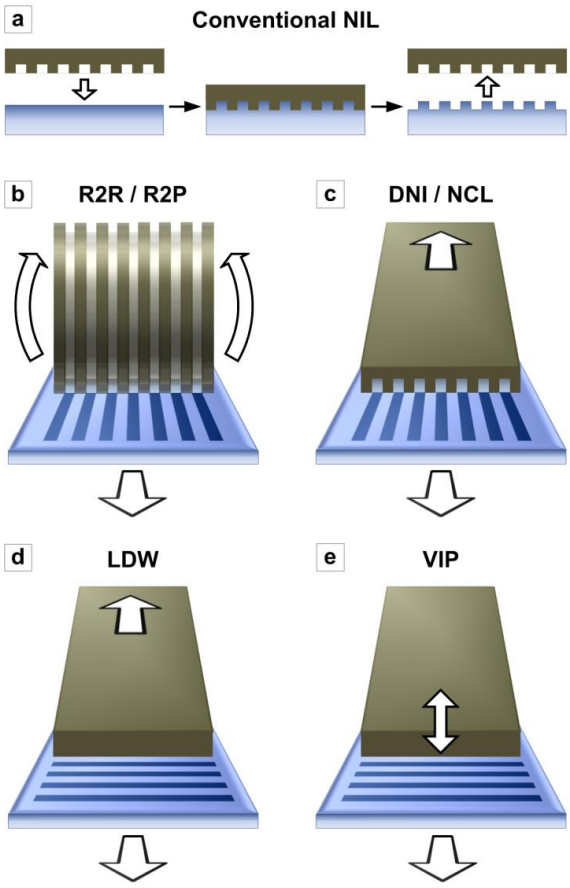

Figure 3.1 Overview of conventional NIL and more continuous and scalable versions (b-e) that will be discussed in this chapter: (b) Roll-to-Roll/Roll-to-Plate (R2R/R2P) nanopatterning, (c) Dynamic Nano-Inscribing (DNI) and NanoChannel-guided Lithography (NCL), (d) Localized Dynamic Wrinking (LDW), and (e) Vibrational Indentation-driven Patterning (VIP).

Despite the simple and relatively low-cost procedure of NIL, the current process and throughput in conventional NIL (on the order of a few minutes per wafer) is still far from meeting the demands of many practical applications, especially in photonics, biotechnology, and organoelectronics. Namely, in typical NIL, the replica area is limited by the master mold size because the patterning process is essentially 'stamping'. The steady heating required in thermal NIL until the substrate (e.g. thermoplastics) is fully imprinted may be another roadblock to further increase the throughput and simplify the process control.

3.2 Scalable and high-throughput micro/nano-manufacturing: chapter overview

In this chapter, we present several continuous and high-throughput patterning techniques based on direct mechanical deformation, which are capable of more scalable and faster fabrication of small-scale features sub-wavelength period gratings; as schematically illustrated in **Figures 3.1b-e**, some can be done with only small area of a master mold, or even need not any pre-defined master pattern.

Specifically, we first introduce *Roll-to-Roll (R2R) NIL (R2R NIL)*[159, 160] that has been developed utilizing the rolling of a flexible master mold to continuously imprint the replica pattern on either a flexible (R2R) or rigid (Roll-to-Plate; R2P) substrate (**Figure 3.1b**). We move on to *NanoChannel-guided Lithography (NCL)*[161] which adopt the sliding of a cleaved edge of a small area of a rigid master mold over a liquid resist-coated substrate to inscribe seamless and indefinitely long nano-grating patterns (**Figure 3.1c**). Moving forward, *Vibrational Indentation-driven Patterning (VIP)*[162]

opens a ‘template-free’ fabrication of grating structures. VIP creates micro/nano-scale gratings via the periodic indentations driven by the vertical vibration of a flat tool edge onto any softer materials (**Figure 3.1e**). We will also demonstrate how these methods can be applied to the high-throughput fabrication of various optoelectronic and photonic devices.

3.3 Roll-to-Roll (R2R) nanomanufacturing toward scalable and flexible electronics

Benefiting from the NIL principle but aiming to achieve further scalable and faster processing, Roll-to-Roll (R2R) NIL technique has realized continuous, large-area fabrication of micro/nano-scale pattern structures[159, 163, 164]. In the R2R NIL process, a flexible micro/nanostructured mold wrapping around a roll makes a conformal contact to another roll where a substrate typically coated with UV-curable resist is attached, and produces a faithful replica pattern as the rolling proceeds under a slight pressure, followed by the instant UV curing to crosslink the resist material and set the patterns.

R2R NIL enables the fabrication of scaled-up replica of micro/nanopatterns on rigid and flexible substrates, while providing much improved throughput at low cost[159, 164]. This continuous and scalable nanomanufacturing technique can be capitalized to various applications. For instance, the R2R-patterned grating structures can be adopted to the large-area metal wire-grid polarizers (MWGPs)[159, 163] and organic photovoltaic cells (OPVs)[165]. There are many other applications that are directly fabricable and/or integrative with the R2R/R2P NIL process, ranging from printable/flexible electronics[166] to functional organic materials[167]. Carbon nanotubes (CNTs)[168]

and graphene[169, 170] of emerging interest as sustainable and multipurpose nanomaterials[171] can also be continuously processed via R2R method for transparent electrodes and electronic templates. Other reported applications include transistors[172, 173], sensors[174], light sources[175], data storages[176], fuel cells[177], and rectennas[178]; a lot more will surely follow. Not limited to grating pattern, the sub-wavelength scale dot patterns can be continuously defined on MIM stack by R2R process to achieve large-area flexible plasmonic structures, as will be demonstrated in the following sections[75].

3.3.1 Design criteria of successful R2R manufacturing system

A more successful and reliable R2R NIL can be achieved by choosing the suitable mold and resist materials and equipping the continuous and uniform resist coating methods. First, the molds for R2R NIL not only should be flexible enough to wrap around a roll but also need to have sufficient modulus to imprint other materials with better durability. Of another great significance is a low surface energy for clean mold release. Meeting these requirements, fluoropolymers[159] such as ethylene tetrafluoroethylene (ETFE) and perfluoroalkoxy (PFA), and polydimethylsiloxane (PDMS)[75] are suitable for mold films.

As proper resist materials, liquid-phase room-temperature UV-curable polymers such as epoxy-silicon[179], and epoxy-silsesquioxane (SSQ)[180] are overall great choices for rapid and continuous patterning free from heating or long-time curing. There are several additional techniques to offer further aids for the patterned resist to remain on the without being detached by the mold; the mold surface can be tuned to have lower

surface energy, the substrate surface can be treated with the primer promoting adhesion to the resist coating[160], or the anti-sticking agent can be added to resist material syntheses[70].

Another important aspect is the continuous and uniform resist coating on a large-area substrate. While spin-coating is popularly used for uniform coating, it cannot afford the resist coating over the long substrate roll or plate continuously fed in the R2R NIL. In this sense, roll-dipping or drop-casting followed by a doctor-blade scraping are attractive alternatives for continuous and uniform coating, which can be readily integrated to the R2R NIL system.

3.3.2 Continuous and scalable fabrication of flexible plasmonic metamaterials via R2R process

Sub-wavelength scale patterns are of great interest for a variety of optoelectronic and photonic applications ranging from wire-grid polarizers[70, 71] to photonic color filters[73, 74] as they can tune the optical properties in desired wavelengths depending on the pattern geometry and structural configuration[69]. In particular, the metal-insulator-metal (MIM) architecture having the top metal layer patterned in sub-wavelength scale can implement such light-interacting metamaterials[181-183] by inducing the surface plasmon polaritons (SPPs) at metal-dielectric interfaces[184, 185]. Accordingly, these patterned MIM structures have been intensively investigated such as plasmonic nanoantennas[186, 187], plasmonic sensors[188, 189], optical absorbers[190], and microbolometers[191, 192]. However, the fabrication of patterned MIM structures over a large area by conventional methods involving photo-, ion-, or e-beam lithography

presents technical limits in scalability as well as fabrication throughput, and has prohibitive costs for practical applications.

Providing a breakthrough solution, here the R2R process as a simple, high-throughput, and fully scalable process is capitalized to the continuous fabrication of a SPP-driven metamaterial array on flexible substrates. Specifically targeting dual-band IR filters (covering 6-8 μm and 10-12 μm wavelengths), we design the Al-SiO_2-Al MIM structure with the top Al layer patterned into subwavelength size circular disk patches having varied diameters in the range of 2-3.2 μm[193]. Using the R2R NIL patterning process, such Al disk patterns with few defects are continuously fabricated on the SiO_2/Al layers deposited on polyethylene terephthalate (PET) substrates. The broadband IR filtering characteristics are investigated through Fourier Transform Infrared (FT-IR) spectroscopy measurement and the results agree well with the 3D simulation based on COMSOL Multiphysics modules.

3.3.2.1 Fabrication and characterization

The overall fabrication procedure is illustrated in **Figure 3.2a.** First a MIM stack of Al (100 nm)/SiO_2 (200 nm)/Al (200 nm) was sputter-coated on a large area PET substrate. Next, a UV-curable epoxy-silsesquioxane (SSQ)[180] was continuously coated over the substrate and then a R2R NIL process is employed to produce continuous patterns in the UV cured SSQ (**Figure 3.2b**). Finally the top Al layer of the MIM stack was etched by using the patterned SSQ masking layer. In this process, a large-area flexible mold having hole patterns with 600 nm depth was first fabricated by stamping a 4"-wafer scale Si pillar master onto a polydimethylsiloxane (PDMS) pad (**Figure 3.2c**),

and the process can be repeated to cover larger areas. The fabrication of the Si master mold follows a similar procedure that can be found elsewhere[194]. The PDMS pad bearing the negative replicas of the Si master was wrapped around a roll in the 6"-compatible R2R NIL apparatus that was previously described[164]. The UV-curable epoxy-SSQ resist was diluted in propylene glycol methyl ether acetate (PGMEA) and coated as a uniform thin film on the MIM-stacked PET substrate by using a motorized 6"-compatible coating module. A 2 min soft-baking at 50 ℃ removes the PGMEA solvent from the SSQ thin film, and the roll bearing the SSQ-coated substrate and supported by an underlying rubber cushion layer was put in conformal contact with the roll bearing the PDMS stamp for the subsequent R2R NIL process.

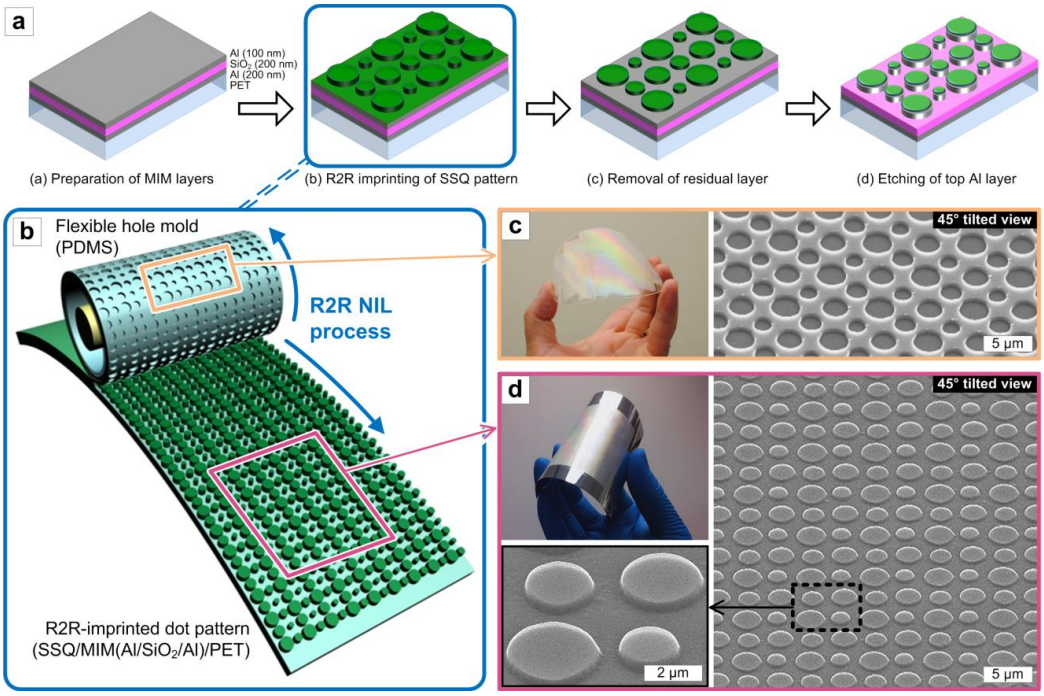

Figure 3.2 (a) Illustration of the overall fabrication procedure of the MIM-based plasmonic metamaterial structure. The SSQ pattern was continuously created on the MIM-deposited PET substrate by the R2R NIL process which is schematically depicted in detail in (b). The flexible large-are PDMS mold having the hole pattern shown in (c) is rolling over a SSQ-coated Al/SiO_2/Al/PET substrate under conformal contact, imprinting the SSQ dot pattern with a very thin residual layer as indicated in (d).

The R2R NIL process was conducted at the speed of as fast as 1 m/min to imprint the SSQ patterns. As demonstrated in **Figure 3.2d**, the R2R NIL process successfully patterns the SSQ layer, and the following etching process faithfully defines the Al disk array on the MIM stack-coated flexible PET substrate. Since the uncured SSQ remains a viscous liquid film after the coating and soft-baking, it can be readily drawn to fill the hole patterns in PDMS by the capillary force induced by the confinement of the PDMS microstructure at contact[195], and the resulting disk patterns can be formed without the aid of excessive pressure at ambient temperature and environment. The UV light (Omnicure S1000, EXFO) instantly cures the imprinted SSQ layer before it is released from the PDMS mold. This gentle but rapid patterning mechanism of the R2R NIL process for the room-temperature UV-curable resist is the pivotal feature that realizes 'continuous' patterning, and therefore improves the fabrication throughput and scalability. Furthermore, due to excellent conformal contact between the polymer substrate and the PDMS mold, the residual layer of SSQ after imprinting could be controlled to an almost negligible thickness in this process and easily removed by a slight reactive ion etching (RIE) if needed[180]. The subsequent wet or dry etching of the top Al layer[196] completes the final MIM structure comprising the Al disk patterns on the SiO_2/Al layers (**Figure3.3**). **Figure 3.3a** demonstrates the fabricated MIM pattern on the flexible PET substrate with few defects. The enlarged top view (**Figure 3.3b**) reveals that the Al disks with four different diameters of 2, 2.4, 2.8, and 3.2 μm are arrayed with 300, 500, 700, and 900 nm spacings. The final pattern geometry is almost identical to that of the original design (depicted in the upper right of **Figure 3.3b**), which ascertains the excellent reliability and precision of the overall fabrication including the continuous R2R NIL

process. Here it is noted that the remaining SSQ mask having the thickness of less than 50 nm (see the inset to **Figure 3.3b**) may work as a protection against environmental insults owing to the SSQ's good physical/chemical robustness[197], and does not affect the IR absorption properties of the structure.

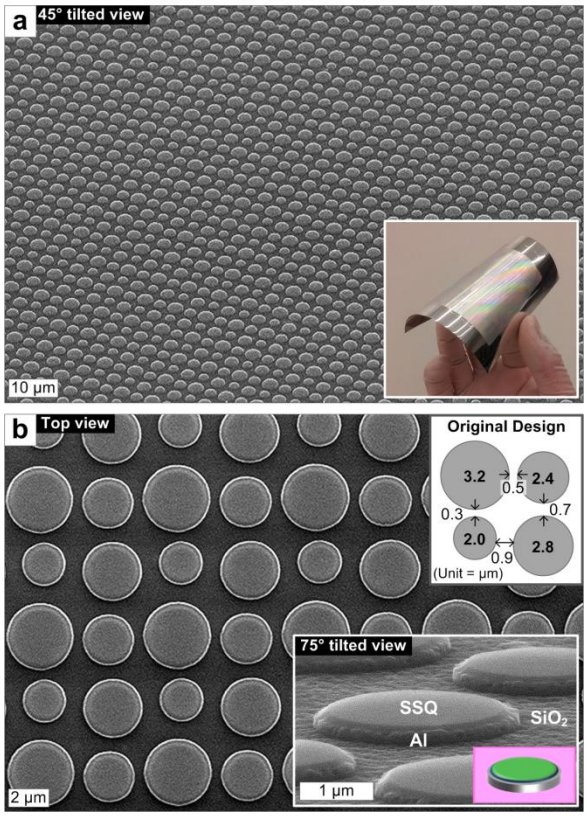

Figure 3.3 (a) The fabricated plasmonic metamaterial film comprising the Al disk array faithfully patterned via the R2R NIL process on SiO_2/Al/PET substrates. The scalability and flexibility are exemplified in the inset to (a). The enlarged top view (b) discloses the fabricated disk pattern geometry that is almost identical to the original design described in the upper-right corner. The inset reveals the remaining SSQ mask on top of Al disk patches.

3.3.2.2 Plasmonic IR filtering characteristics

The IR reflection spectrum of the fabricated sample is measured by the FT-IR spectroscopy (Spectrum GX, Perkin-Elmer, with the incident IR wavenumbers swept

from 4000 cm^{-1} to 400 cm^{-1}), and is displayed in **Figure 3.4** along with the 3D simulation (COMSOL Multiphysics) plot calculated using the original geometry for the same wavelength regime. The desired broadband IR filtering characteristics with two broadened bandwidths in approximately 6-8 and 10-12 μm wavelengths is validated experimentally, and is confirmed to be in fairly good agreement with the result obtained from the simulation. Moreover, these properties are independent of the polarization due to the circular shapes of metal pattern[189] as well as of the IR incident angle owing to the strong coupling between the SPP modes of the metal pattern and underlying dielectric layer[185].

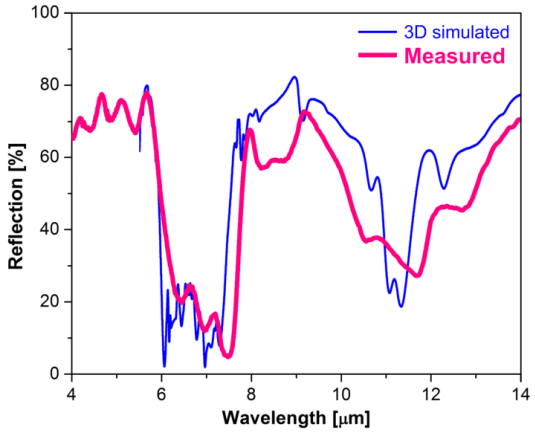

Figure 3.4 (a) The fabricated plasmonic metamaterial film comprising the Al disk array faithfully patterned via the R2R NIL process on SiO_2/Al/PET substrates. The scalability and flexibility are exemplified in the inset to (a). The enlarged top view (b) discloses the fabricated disk pattern geometry that is almost identical to the original design described in the upper-right corner. The inset reveals the remaining SSQ mask on top of Al disk patches.

The disk patterns with multiple diameters in a unit cell allow the plasmonic MIM array structure to operate in a wide IR range, which is attributed to the superposition of individual resonance dips determined by each disk diameter, thereby yielding overall broadening effect[198]. Similar plasmonic wideband IR absorbers based on these

principles have been demonstrated by adopting the 2D MIM gratings[186] or 3D square patches[187] with multiple sizes. The metal disk together with the bottom metal layer and the dielectric defines a Fabry-Perot resonator, and the wavelength λ for the first-order resonance is roughly given as $\lambda \approx 2n_{eff}w$ [186], where n_{eff} is the effective index of the MIM waveguide and w is the diameter of the metal disks. This is confirmed by additional calculations; the IR reflection spectra simulated from the identical MIM pattern but with the uniform disk size (i.e. either 2, 2.4, 2.8, or 3.2 μm) show narrower dips corresponding to their respective first- and second-order resonances, as summarized in **Table 3.1**. The resonances from each disk size remain almost invariant regardless of the change in the period (not shown here), which is consistent with the literature[182]. In the IR reflection spectrum, the reflection dips from neighboring narrow bands can overlap and merge to form a broadened reflection band when the disk resonators with different diameters are grouped into sub-wavelength unit cell. We found that the overlap of the four individual plots is nearly matching to the simulated spectrum of the original mixed disk array (**Figure 3.4**). Consistently, in the experiment two broadened dips in the reflection spectrum emerge at 6-8 and 10-12 μm wavelengths with the appearances of combined resonances from four different disk diameters, which are suitable for dual-band IR filter applications.

Table 3.1 Simulation data of fundamental and second-order resonances for each diameter.

Disk diameter [μm]	Fundamental resonant mode [μm]	Second-order resonant mode [μm]
2.0	9.87	5.62
2.4	10.56	6.07
2.8	10.87	6.64
3.2	11.28	7.11

3.3.3 Summary

We have demonstrated a practical methodology for the continuous fabrication of plasmonic metamaterial films by utilizing the high-speed R2R NIL process. Attributed to its rapid and continuous patterning principle, the process throughput as well as scalability can be significantly enhanced. As a specific example, we have successfully fabricated a dual-band IR filtering array in the form of patterned MIM structures on flexible PET films by continuously patterning the top metal layer into the disk array with varying diameters. The fabricated metamaterial structure exhibits the desired broadband IR filtering characteristics contributed from the multiple resonance dips, which is also verified by the 3D simulation analysis. Our method may open a facile route to fabricating various metamaterial structures on scalable and flexible substrates at low cost and high speed.

3.4 Continuous and seamless fabrication of nanogratings by NanoChannel-guided Lithography (NCL) on liquid resists

One of the biggest challenges underlying in R2R NIL may be the fabrication of an original flexible mold large enough to afford the roll wrapping. Usually starting from the small-area fabrication of master patterns onto a rigid substrate (e.g. Si) by means of laser interferometry or e-beam writing, the mold must be scaled up to the desired area through stepping or tiling processes, followed by the transfer onto a flexible film. In addition, there is an inevitable seam region where the two ends of the flexible mold meet on the roller, which interrupts the otherwise continuous patterns. Alternative methodologies to address these issues therefore must realize seamless patterning without the need of large-

area molds.

The recently reported Dynamic Nano-Inscribing (DNI)[199] method can create seamless large-area nanogratings on any materials softer than the molds at high speed. DNI uses a slice of cleaved rigid grating molds to mechanically inscribe a polymer surface to create nanograting structures in a dynamic fashion. However, the elastic recovery of the plastically deformed solid surfaces after the release of mechanical force[200] limits the aspect ratio of the inscribed structure, especially for small period gratings. This cannot satisfy the need for many applications such as metal wire-grid polarizers[71, 201] where higher aspect-ratio and well-defined cross-sectional profiles are highly desirable[163].

To address these issues, we have developed a nanopatterning technique by adopting liquid resist materials to a high-throughput nanoinscribing process, aiming to achieve high-speed and low-cost fabrication of continuous nanograting structures for large-area optoelectronic applications. As a suitable liquid resist, we introduce UV-curable epoxy-based silsesquioxane (SSQ) which is a viscous liquid polymer that solidifies into a cross-linked high-modulus material upon UV curing without significant volume shrinkage[180]. Whereas a relatively large force is required to 'inscribe' nanopatterns on a solid substrate by plastically deforming the material, a liquid resist can readily 'infiltrate' the openings in the mold grating upon contact under slight mechanical force. These nanochannel-guided liquid streaks are continuously extruded from the contact region as the mold translates along the surface, enabling continuous formation of nanograting patterns without elastic recovery. To ensure the success of the nanopatterning process by this "*NanoChannel-guided Lithography* (NCL)", the substrate

material should have non-wetting property with respect to the liquid resist used in the process. The shallow but plastically deformed groove features on the substrate along with its non-wetting characteristics prevent the immediate reflow of the as-formed liquid nanograting structures until the pattern is fully cured by UV light.

3.4.1 Process overview of NCL

The setup for the NCL process is schematically shown in **Figure 3.5a**. First, the edge of a rigid grating mold makes contact with a UV-curable liquid resist coated on a polymer substrate (i.e. perfluoroalkoxy (PFA) or polyethylene terephthalate (PET)). The grating mold is inclined at an angle of ~15° with respect to the moving substrate and the contact force is about 5 N. The contact point can be maintained at ambient or elevated temperature, controlled by localized heating by using a conductive heater attached to the backside of the mold. The heating is used to adjust the viscosity of the liquid resist for optimal filling of the nanochannel features on the mold within the processing time. The polymer substrate is placed on a silicone rubber film, which prevents the substrate against slip during the process and ensures conformal contact to the mold edge with the support of a multi-axial tilting stage. As the substrate is moved at a controlled speed with respective to the mold, the liquid resist material on top of the substrate is extruded from the end of the nanochannels on the mold, as illustrated in **Figure 3.5d**. A UV light placed in front of the mold promptly cures the liquid resist to form the nanogratings with well-retained profile. Such a continuous process produces a seamless nanograting in cured liquid resist material.

The mold-substrate contacting angle, θ, can be chosen between ~10° to 35° for

reliable processing; too small θ may induce excess liquid resist to infiltrate the mold openings by capillary action before entering the contact region. On the other hand, if θ becomes too large, the effective mold opening depth, $d(\cos\theta)$ where d is the original mold opening depth, becomes smaller, which can restrict liquid infiltration along the nanochannels at contact.

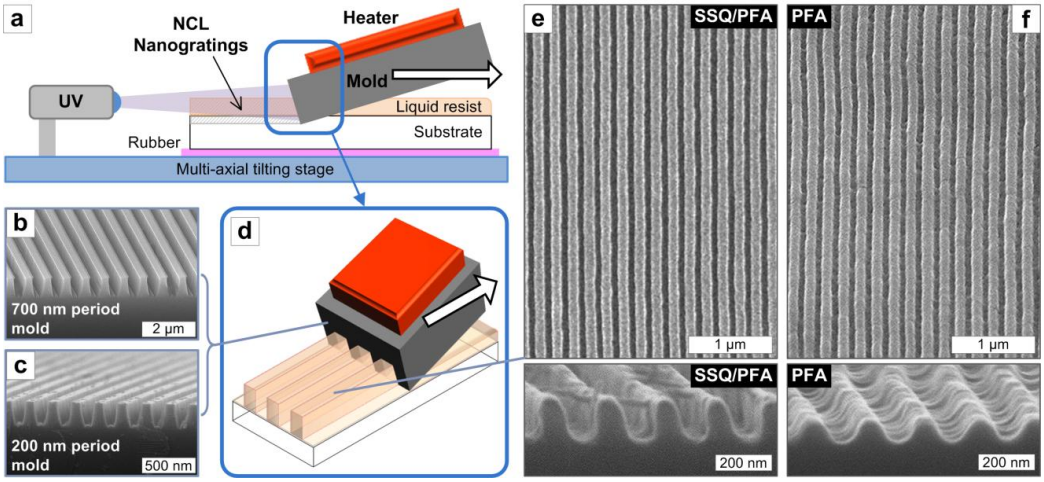

Figure 3.5 (a) Schematics of the NCL process where the liquid resist is extruded from the nanochannels on the grating mode and promptly cured by UV light to retain the profile. A slice of the SiO_2/Si grating molds having either (b) 700 nm or (c) 200 nm period is used at ambient or heated condition, and the liquid SSQ resist is coated on a polymer substrate (e.g. PFA or PET). An enlarged perspective view of the process (d) illustrates the liquid lines are extruded from the openings of the mold grating at the contact region. SEM images of 200 nm period nanogratings formed on the PFA substrates at 80 ℃ (e) with and (f) without liquid SSQ coating. The insets are the counterprofiles of each grating structure, evidently showing that the aspect ratio of resulting nanogratings can be significantly improved by the use of SSQ layer.

3.4.2 Nanograting formation on liquid-coated surfaces compared to solids

The key advantage of the NCL process is that it can produce nanograting structures in a UV curable liquid resist with higher aspect-ratio profiles than ones

inscribed on the solid plastic surface by the DNI process. This is demonstrated by comparing the 200 nm period grating patterned on a SSQ-coated PFA surface by NCL with the grating formed on the solid PFA by DNI, as shown in **Figures 3.5e and 3.5f**. Similar results were observed in gratings of different periods (e.g. 700 nm) and substrate materials (e.g. PET), as can be found in **Figure 3.6**.

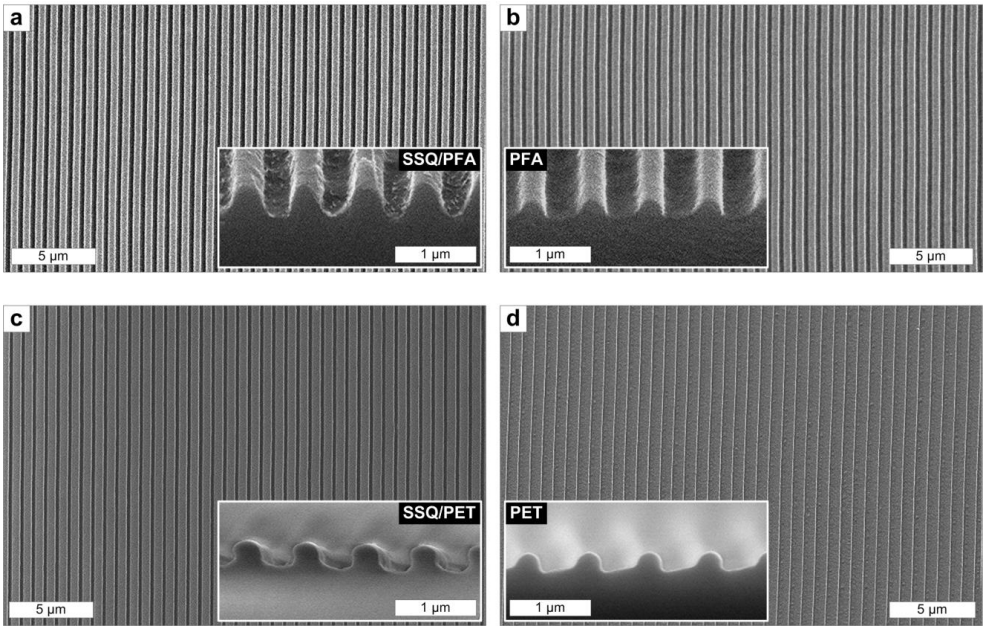

Figure 3.6 SEM images of 700 nm period nanogratings formed on the PFA substrates (a) with and (b) without SSQ coating, and formed on the PET substrates (c) with and (d) without SSQ coating. All are processed at 80 °C. The insets are the counterprofiles of each grating structure, evidently showing that the aspect ratio of resulting nanogratings can be significantly enhanced by the use of SSQ layer. These are all consistent with the result obtained in 200 nm period nanogratings on PFA substrates (Figures 3.5e and 3.5f).

For the normal DNI patterning on solids, the plastic deformation by mechanical inscription that forms the nanograting is inherently limited by the elastic recovery process. This effect hampers a reliable patterning of nanograting of smaller periods (e.g. 200 nm period) even under a very large mechanical load. In comparison, in the new NCL process, the liquid resist material can be readily filled into the nanochannels on the SiO_2/Si grating

mold due to viscous flow, similar to the polymer flow process in Nanoimprint Lithography (NIL)[9]. Excessive liquid is continuously swept away by the mold until the process terminates, which is confirmed by the experiments where the same nanograting structures are obtained despite different thicknesses of the initial SSQ resist. The final pattern appears to have slightly rounded corners due to the reflow of as-patterned polymer liquid grating before it is fully cured, similar to the previous reports[202, 203]. However, the as-extruded liquid streaks on the underlying surface can mostly sustain the structures without significant immediate reflow by the control of wetting properties, as will be explained in detail.

3.4.3 Interactive influence of resist wettability and substrate topography

In NCL, the liquid-solid interaction plays a critical role in determining the final profile of the nanostructures. This is because the as-formed liquid SSQ grating extruded from the nanochannel should be able to maintain its profile rather than immediate reflow before it is cured, which is directly related to the wetting property of the solid surface. Interestingly, we found that the solid substrate surface underneath the liquid SSQ layer appears to be simultaneously inscribed during the process (**Figure 3.7**). The inscribed profile on PFA substrate is more pronounced than that of PET; and the SSQ grating has more faithfully replicated profile on PFA but not on PET substrate. We believe that the nanograting formation in the NCL process is dictated by two main factors: (1) the wetting characteristics of liquid SSQ on the solid surfaces, and (2) the deformation characteristics of the solid surface. Therefore both the surface energy and elastic moduli of the solid substrate are important in this process.

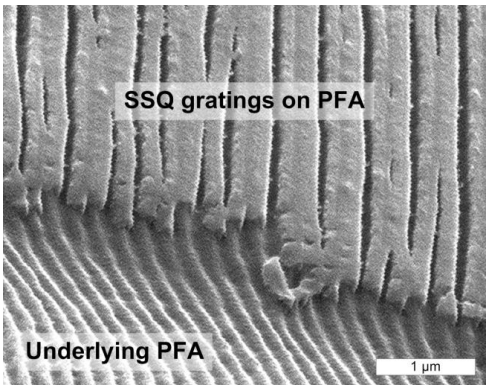

Figure 3.7 SEM image of the exposed underlying PFA surfaces after the NCL process, showing deformed morphology along the mold transfer direction. The sample was fabricated by applying the 200 nm period mold on the SSQ-coated PFA substrate at 80 ℃, followed by full curing under intense UV light. To make this boundary, the fully cured SSQ/PFA nanograting sample was first vapor-treated with Silquest A-187 at 90 ℃ for 5 min. Next, epoxysilicone was partially applied (drop-casting) and UV-cured, then was quickly delaminated by a razor blade. The SSQ/PFA grating at the boundary look somewhat stuck to each other because of capillary infiltration of residual epoxysilicone.

Figure 3.8 compares the nanograting formation characteristics on solid materials (i.e. PFA and PET) having different elastic modulus; and SSQ liquid resist also has different wetting behaviors on the two substrates due to the different surface energies of the two substrates. The contact angles of a liquid SSQ droplet on the flat PFA and PET surfaces at room temperature were 67.9° and 20.1°, respectively (**Figures 3.8a1 and 3.8b1**). The large contact angle and the resultant non-wetting behavior of liquid SSQ on PFA will stabilize the as-formed liquid grating against reflow, allowing time for it to be cured and solidified (**Figure 3.8a**). In fact, it was observed that the grating profile remains almost static regardless of the UV curing time, confirming the self-stabilization of the as-extruded liquid lines from the nanochannles on the mold on PFA. In contrast, the small contact angle between liquid SSQ on PET dictates a good wetting behavior of the SSQ on PET that results in quick reflow of the as-formed nanograting structure (**Figure 3.8b**). One should also take into account that during the NCL process the

underlying PFA surface having a smaller modulus (E ~0.5 GPa) is deformed more than PET (E ~3 GPa). Thus, as schematically shown in **Figure 3.8a2**, the as-formed liquid SSQ grating sitting on top of the inscribed PFA grating benefits from the large contact angle at SSQ-PFA interfaces and maintains a vertical profile, which is essential to obtain high aspect-ratio nanograting structures. On the other hand, the shallow profile in PET due to its high modulus and the low contact angle of SSQ cannot efficiently prevent the lateral reflow of the liquid resist pattern before it is fully cured.

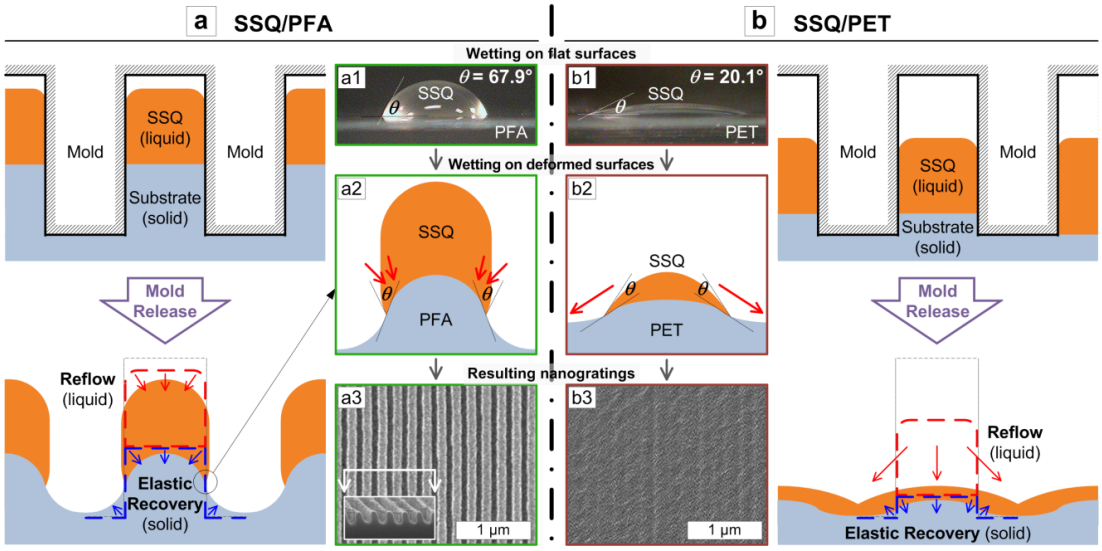

Figure 3.8 Diagrams of nanograting formations by the NCL process on SSQ-coated (a) PFA and (b) PET substrates. At contact, liquid resist is filled into the nanochannels on the mold and solid substrate is plastically inscribed by the sharp edge of the grating mold. The inscribed solid surface undergoes elastic recovery while the as-formed liquid experiences reflow depending on its wettability on the solid surface. Final grating geometry is determined by the cooperative effect of liquid wetting and substrate topography. The contact angle of SSQ droplets is much larger on PFA than on PET ((a1) and (b1)). Meanwhile, PFA is deformed more than PET due to its smaller modulus, which helps to maintain a vertical profile of the SSQ ridges on top. This is comparatively depicted in (a2) and (b2) where the subsequent reflow directions are marked with arrows. The SSQ reflow on PFA is effectively restricted by the local contact with SSQ-repellant PFA grooves, whereas the as-formed liquid SSQ lines on the PET surface shortly collapse due to the better wettability on PET along with the insufficient local deformation of the PET surface. Accordingly, the resulting nanogratings processed at 80 ℃ ((a3) and (b3)) show that more faithful, higher aspect-ratio nanogratings can be created on the SSQ-coated PFA surface (inset to (a3) shows the counterprofile of a cross-section).

To further verify the wetting-dependent mechanism, we modify the surface of the PET by fluorosilane coating to render it non-wetting to SSQ. **Figure 3.9** compares 700 nm period SSQ nanograting formed on the normal and fluorosilane-treated PET (F-PET) substrates by NCL, respectively, which demonstrates that the pattern profiles can be tuned by different wetting conditions on the same material substrate. Here, a much larger contact angle of SSQ to the F-PET prevents the wetting-induced reflow of liquid SSQ and allows time for the as-formed SSQ grating to be fully cured before it is relaxed by the reflow. This may enable the fabrication of high aspect-ratio nanogratings on hard surfaces which cannot usually form very deep patterns under normal circumstances.

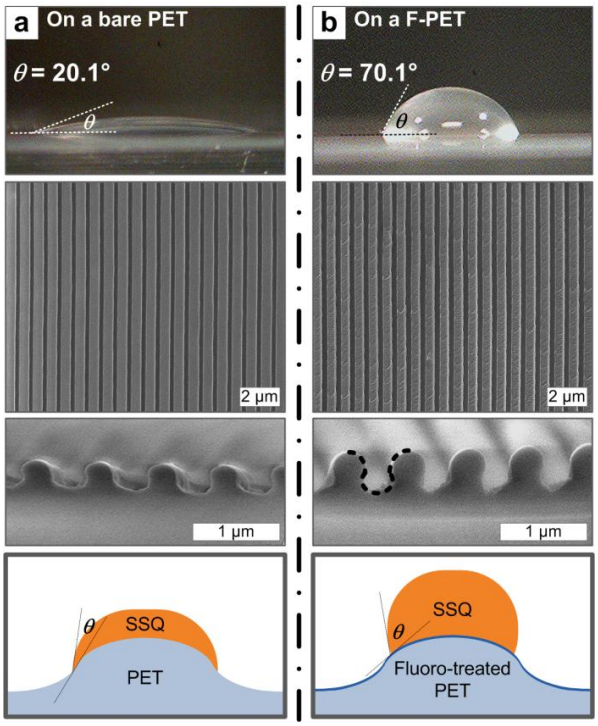

Figure 3.9 Comparison of nanogratings formed on the surfaces of the same material with different surface properties: (a) normal PET and (b) fluorosilane-treated PET (F-PET). A significant increase in contact angle is observed in a F-PET surface, resulting in the nanograting (processed at 80 ℃) with higher aspect ratio which is attributed to the improved non-wetting characteristic of the substrate surface that mitigates the reflow of the as-formed liquid resist grating. ases as the temperature increases up to ~80-90 ℃. SSQ starts to cure beyond ~90 ℃, causing increase in viscosity.

3.4.4 Temperature-controlled grating heights

Understanding the flow characteristics of the liquid SSQ material, such as viscosity, is important to determine the channel filling behavior in the NCL process prior to the UV curing. We observed that the viscosity of the liquid SSQ decreases with the increasing temperature from room temperature up to around 80 °C, as presented in **Figure 3.10a**. It was also confirmed that liquid SSQ behaves as a Newtonian fluid since the viscosity remains constant and shear stress increases linearly with the sweeping shear rate[161]. For a Newtonian liquid such as liquid SSQ, and assuming laminar flow, the velocity, u, at which a mold channel is filled is proportional to $\tau(L/\mu)$ [204], where τ is shear stress, L is the channel width, and μ is the viscosity of the SSQ liquid material. This is consistent with the cavity filling time in regular NIL process[1].

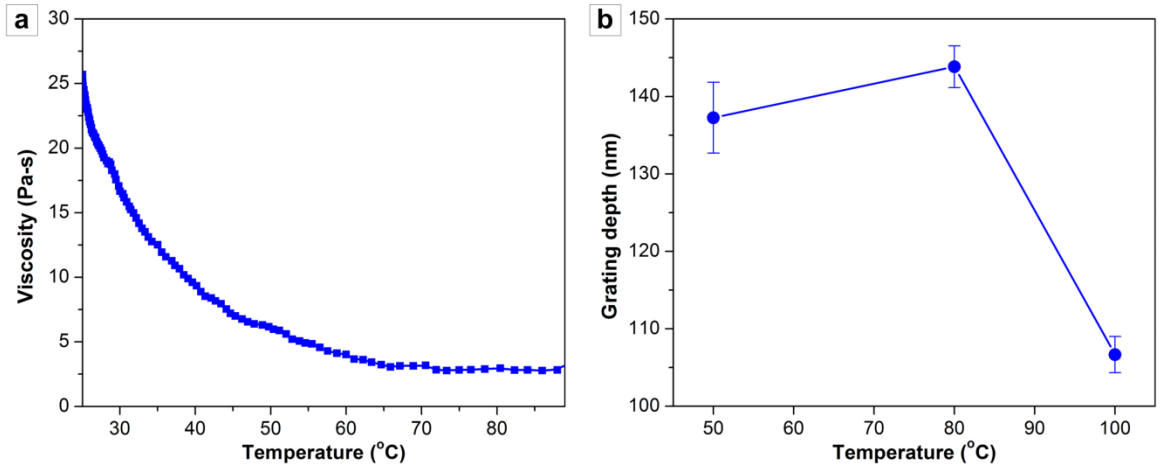

Figure 3.10 (a) Viscosity of liquid SSQ as a function of temperature. The SSQ viscosity decreases as the temperature increases up to ~80-90 ℃. SSQ starts to cure beyond ~90 ℃, causing increase in viscosity. (b) The grating depths measured from the counterprofiles of 200 nm period nanogratings formed on SSQ-coated PFA substrates at different temperatures. The values are averaged over three different positions for each case.

In NCL, this relationship suggests that for the same applied pressure, and given a similar process speed, a grating pattern with a greater depth can be obtained for a lower viscosity SSQ due to a more complete filling of the nanochannels by the liquid SSQ, which can be achieved by a higher processing temperature (**Figure 3.10b**). The pattern depth becomes smaller at 100 °C than at 80 °C because the heat causes partial curing of the SSQ resist and therefore an increase in SSQ viscosity. A similar trend is observed when using PET as substrates, as shown in **Figure 3.11**.

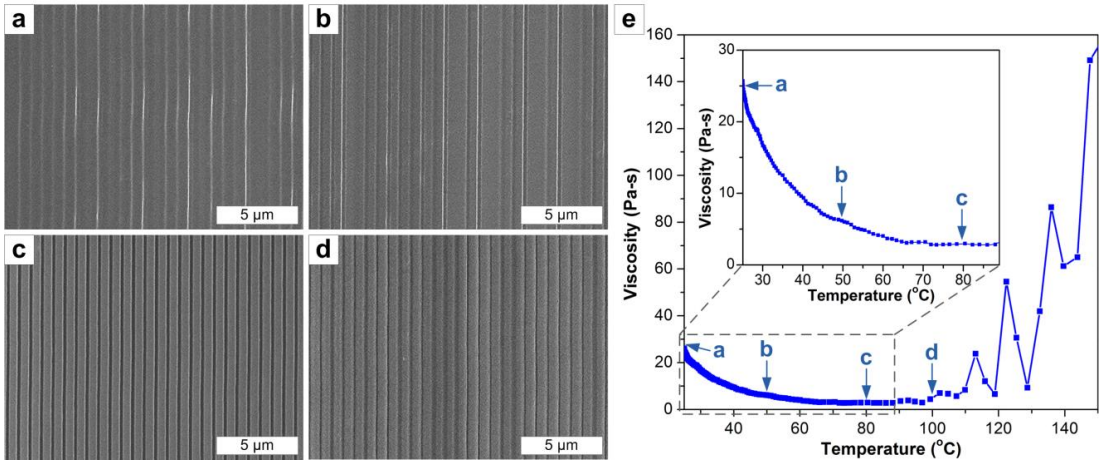

Figure 3.11 SEM images of 700 nm period nanogratings formed on the SSQ-coated PET substrates at different processing temperatures: (a) room temperature, (b) 50 ℃, (c) 80 ℃, and (d) 100 ℃. The viscosity of SSQ as a function of temperature is shown in (e), with the marks at which (a)-(d) are processed. The grating depth appears to increase with more faithful profiles from room temperature up to 80 ℃, as the SSQ viscosity decreases, while it appears to become shallower when processed at 100 ℃ at which the SSQ viscosity increases because of curing effect. The viscosity measurement becomes unstable after 90 °C presumably due to the 'stick and slip' motions caused by the SSQ curing, but the increasing trend is obvious.

3.4.5 Potential prospects of NCL

We have demonstrated that faithful nanogratings can be fabricated by NCL with the feature size as small as 100 nm. We believe this resolution may be further scaled

down by controlling the process parameters as well as selecting resist and substrate materials showing larger contact angle. Topographies on the underlying solid substrates created by mechanical inscription during NCL help the the as-extruded liquid patterns maintain a more vertical profile and therefore sustain the shape of the liquid walls while it is being cured. In our previous work on DNI, we have observed that it becomes more challenging to inscribe grooves on solids as the feature size decreases, which can be a limiting factor for the minimum feature size in the NCL process. A systematic study on this nanoscale mechanical inscription of various solids is currently in progress to extend the processability of NCL down to smaller scales. Since a processing force can be controlled to be very small, mold wear caused by continuous contacting can be significantly reduced to enhance process durability.

3.4.6 Summary

We developed a novel technique to fabricate continuous high aspect-ratio nanograting structures down to sub-100 nm scale by the NCL, a NanoChannel-guided Lithography process, using liquid resists. The procedure of NCL process can be summarized as following: (1) A slice of grating molds, typically heated, contacts a liquid-coated substrate at an angle. (2) At mold-substrate contact, the liquid layer (SSQ) infiltrates the nanochannels on the mold, while the edge of the mold simultaneously inscribes the plastic substrate to form shallow grooves. (3) As NCL proceeds, the liquid SSQ grating is extruded from the nanochannels. (4) The non-wetting behavior of the liquid resist against the topographically deformed plastic substrate prevents the immediate reflow of the liquid grating pattern, allowing time for it to be fully cured and

become solid nanogratings. Since the UV cured resist forms discrete lines on top of the polymer substrate that has inscribed slightly, the NCL process can be regarded as a residual layer-free process. Therefore the typical process employed in NIL to remove the residual layer by anisotropic etching is unnecessary. The final geometry of liquid gratings can be tailored by the processing temperatures as well as the surface characteristics of the underlying solid substrate. Such a 'direct-write' NCL patterning of liquid resists is a gentler process than the previous DNI technique and result in much more faithful pattern replication, especially for small period and high aspect ratio structures. This new technique may open a way to mass-produce large-area, high-quality nanogratings at low cost. Such nanogratings can be utilized in a variety of applications such as metal wire-grid polarizers and plasmonic color filters[73, 158].

3.5 Template-free Vibrational Indentation Patterning (VIP) of micro/nano-scale grating structures with real-time pitch and angle tunability

(*This work is done with collaboration with Dr. Se Hyun Ahn.*)

Roll-to-Roll (R2R) NIL[159, 205] has opened a way for continuous NIL processing over large area, where a roll bearing a flexible imprinting stamp prints the replica pattern on the substrate roll in a continuous fashion. For seamless and faster patterning, continuous Dynamic Nano-Inscribing (DNI)[206] and NanoChannel-guided Lithography (NCL)[161] have been introduced to produce linear patterns that only require a thin slice of cleaved grating mold.. Nevertheless, all these mechanical-based

processes require the original stamps containing nanostructures which should be prepared by low-throughput processes such as e-beam lithography or laser interferometry.

One attractive strategy to overcome the aforementioned issues is to utilize direct mechanical indentation to the micro- and nano-scale patterning as long as an indenting tool is mechanically harder than the substrate materials. With repeated indenting by the tools having relatively simple shapes, the micro/nano-scale patterns can be obtained in a continuous and seamless manner. Indeed, nano-hole arrays have been successfully fabricated by using atomic force microscope (AFM) for biomimetic dry adhesives[207] or ultrahigh-density data storage applications[208]. However, these approaches require multiple times of tip indentations and still should be accompanied with the prerequisite steps to prepare nanopore membranes[207] or block copolymer templates[208]. Micro-indentation process using a pyramidal diamond tip has also been adopted to develop micro-nano hybrid patterns on an anodized aluminum substrate, which is however based on the destructive denting of nanostructures under heated conditions[209]. Therefore it is still demanding to capitalize the mechanical indentation to more scalable and controlled patterning at ambient conditions.

Here we present a highly versatile and more practical patterning method, Vibrational Indentation-driven Patterning (VIP), to continuously create micro/nano-scale gratings on various materials with real-time tunability of grating periods and profiles. In VIP a tilted edge of a hard material (e.g. Si wafer) is set to high-frequency vertical vibration, where the tool edge makes sequential indentations onto a moving substrate and continuously create grating patterns at high speed. VIP can make perfectly straight and multidimensional grating patterns onto any substrates softer than the tool material. The

grating periods and depths can be easily controlled simply by modulating the tool vibration and/or substrate feeding rate. As a result, the period-variable chirped gratings can be easily achieved. Furthermore, controlling the tool tilting angle leads to the fabrication of angle-tunable blazed gratings. Such structure can be further configured to become optical polarizers after angled-deposition of metal on one side of the blazed planes.

Additionally the nature of sequential indentation of VIP process enables the creation of nano-scale grating pattern over infinitely long flexible substrate, by using a finite size indenting tool. Such a utility makes it very attractive to use VIP to produce flexible template for high-throughput R2R NIL.

3.5.1 Principle and design of VIP

3.5.1.1 Basic principle of VIP

The working principle of VIP is simple and straightforward. A well-cleaved Si wafer edge (or a flat edge of any hard materials) tilted at a proper angle and vibrating at a desired frequency sequentially indents into a moving substrate to generate V-shaped periodic gratings (**Figure 3.12a**). In one embodiment, the vibration is generated by a high-speed servo motor controlling a rotation with a mass eccentrically mounted on the head. The period λ of resulting pattern is simply given as $\lambda = V / f$, where f is vibration frequency of the tool and V is the substrate feeding speed. Assuming the edge is perfectly cleaved to 90° and the elastic recovery of a substrate after deformation is negligible, the indented trench width s becomes $s = h\ (\tan\theta + \cot\theta)$, where h is indented depth and θ is tool tilting angle. Therefore, the period of grating patterns can be easily controlled by

modulating the vibration frequency and/or substrate feeding speed. As will be demonstrated later, the real-time modulation of tool-substrate motion and tool tilting degree during a single VIP process can create the grating patterns having varying periods and angles. Also, the trench geometry can be readily controlled by the indenting force (vibration amplitude) and tool tilting angle. In this paper, VIP has been performed at 45° tilting angle to achieve the symmetric V-shaped patterns unless otherwise specified; later, the tilting angle will be varied to demonstrate the fabrication of asymmetric blazed gratings with different blazed angles.

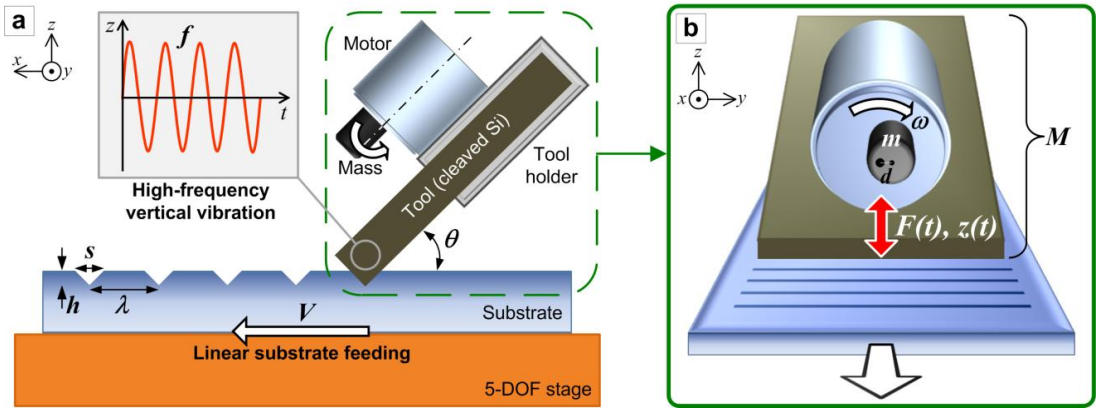

Figure 3.12 Schematics of Vibrational Indentation-driven Patterning (VIP) with the process parameters indicated: (a) side view and (b) perspective view. A mass eccentrically mounted to the high-speed motor generates high-frequency vertical vibration at the tool tip, creating periodical indentations into a moving substrate to continuously produce micro/nano-scale grating structures with V-shape trench profile.

3.5.1.2 Additional design considerations

Several design aspects may be taken into account to generate more reliable vibration in VIP. Stable vertical oscillations of the tool at a consistent frequency and with sufficiently high amplitude are of great importance in VIP to achieve uniform and faithful patterns. Vibration force (F) generated from an eccentric mass (m) with the distance from

mass center (*d*) at the rotating speed of ω (see **Figure 3.12b** for notations), is given as a function of time *t* as,

$$F_e(t) = md\omega^2 \cdot \sin \omega t \tag{3-1}$$

The corresponding vertical response *z* of the total system (motor-assembled tool) with the mass of *M* is

$$z(t) = \frac{m}{M} d \left(\frac{\omega}{\omega_n} \right)^2 \left| G(i\omega) \right| \sin(\omega t - \phi) \tag{3-2}$$

where ω_n is a natural frequency given as $\omega_n = \sqrt{k/m}$, and $G(i\omega)$ is defined as $G(i\omega) = (1-(\omega/\omega_n)^2 + 2i\zeta(\omega/\omega_n))^{-1}$ where ζ is a damping ratio of system written as $\zeta = c/(2\sqrt{mk})$ with arbitrary constant of *c*. An excitation frequency can be chosen to be away from the system's resonance frequency to avoid the resonance or by increasing the damping factor (e.g. critical damping (ζ = 1)). In this work we adopt the former as it is experimentally more reasonable to implement.

Since the vibrating motor uses a single eccentric mass, there are other degrees of vibrating motion apart from the vertical direction. To enable vertical indentations (i.e. along the *z*-axis as specified in **Figure 3.12**) with minimal lateral (i.e. *x*- and *y*-axes) perturbations, the tool mounting setup is designed to have much higher stiffness in the *x*- and *y*-directions.

Similar to our previously demonstrated techniques such as DNI and NCL that also use tilted edges, conformal contacting to the substrate is a key criterion for reliable patterning in VIP. Hence, polymer substrates having a certain level of compliances are desirable to accommodate conformal contact. This also helps extend the tool life.

3.5.2 Fabrication of uniform period gratings with easy control of pattern period and depth

The micro/nano-scale grating structures of arbitrary periods can be fabricated by VIP without prefabricated stamps. The grating period can be easily controlled by modulating vibration frequency and substrate feeding speed. **Figure 3.13** shows Scanning Electron Microscope (SEM) images of grating patterns having uniform periods fabricated on polyethylene terephthalate (PET) substrates. With the vibration frequency fixed vibration at 150 Hz (corresponding to ~9000 rpm motor rotation), a 250 µm s^{-1} substrate feeding speed produces ~1.6 µm periodic pattern (**Figure 3.13a**). The same vibration frequency with 100 µm s^{-1} feeding speed yields ~660 nm periodic pattern as shown in **Figure 3.13b**. Likewise, the period can also be controlled by adjusting the vibration frequency at constant feeding speed.

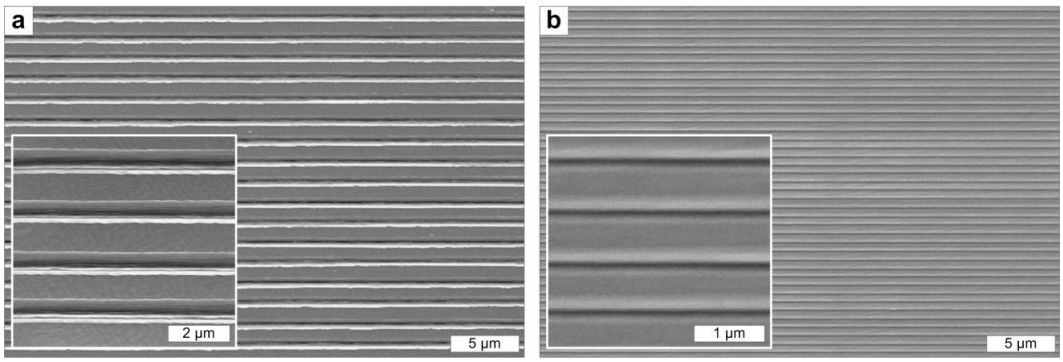

Figure 3.13 SEM images of micro/nano-scale gratings fabricated on PET substrates by VIP. Different substrate feeding speeds of (a) 250 µm s^{-1} and (b) 100 µm s^{-1}, under the constant vibration frequencies of 150 Hz, lead to 1.6 µm and 660 nm uniform period gratings, respectively. Insets reveal (a) deep and (b) shallow pattern profiles controlled by the tool-substrate gap during VIP. Note the patterns shown in insets to (a) and (b) have different periods.

Here the pattern profile (e.g. trench depth) can be controlled by adjusting the indenting force which depends on the contacting point of the oscillation cycle. When

indentation occurs at the midpoint of the oscillation cycle where the force is the maximum, the deepest trenches can be achieved (inset to **Figure 3.13a**). On the other hand, if the tool just touches the substrate at the lowest point of oscillation cycle, very shallow trenches are created (**Figure 3.13b**).

By combining higher vibration frequency and slower substrate feeding, the resulting pattern period can become essentially as small as desired. The practical limit, however, emerges from several issues. The sharpness of the indenting tool needs to be guaranteed. It is more challenging for the vibration at very high motor rotation rate (i.e. faster than ~25,000 rpm in our setup) to stay at steady and uniform stroke because of the motor resolution. The motorized linear stage used for substrate feeding also has the minimum incremental speed (i.e. ~25 μm/s in our setup). Aside from these instrumental limitations, the principle of VIP process also predicts that the vertical response becomes larger as the vibration frequency increases (see Eq. (3-2)); this is counterproductive to the fact that smaller pattern typically requires smaller indentation amplitude. Considering all these aspects, the smallest feature size that VIP can reliably achieve with our current experimental system is ~100 nm.

3.5.3 Applicability to various substrate materials and multidimensional patterns

Based on pure mechanical indentation, VIP can create grating patterns on any substrate material softer than the tool material. Essentially the substrate does not require any pretreatment (e.g. surface chemical modification or coating of a resist material), which is a great benefit over conventional lithographical technologies. Furthermore, since

VIP does not involve any heating or chemical agent, it can be used to pattern thermosensitive organic materials at ambient environment.

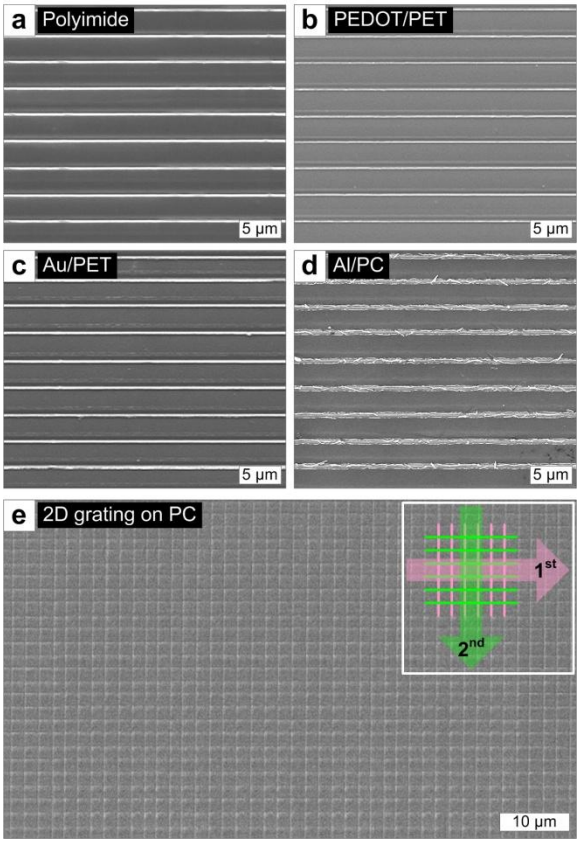

Figure 3.14 (a)-(d) Grating patterns with 3 μm periods fabricated by VIP on various substrates: (a) polyimide, (b) PEDOT-coated PET, (c) 50 nm Au-coated PET, and (d) 50 nm Al-coated PC. (e) 2D grating structures of 2 μm period fabricated on PC by two sequential VIP processes along the perpendicular axes as illustrated on the upper-right corner.

Figure 3.14 demonstrates ~3 μm period grating patterns fabricated by VIP on various substrates. A polyimide film, widely useful for its excellent chemical/mechanical stability, is typically uneasy to pattern due to very high glass-transition temperature (T_g > 350 ℃) and low toughness, but VIP can readily make clear patterns as shown in **Figure 3.14a**. Poly(3,4-ethylenedioxythiophene) (PEDOT) is a key conductive polymer material popularly used in organic light-emitting and photovoltaic applications[210], yet is

vulnerable to the exposure to heat and chemicals. Although we previously demonstrated that localized heated-DNI (LH-DNI) could create nanogratings on PEDOT and poly(3-hexylthiophene) (P3HT)[206], the applied heat might affect the properties of those organic materials over times. Here, VIP provides a safer solution to fabricate grating pattern on the heat-sensitive organic layers at room temperature, as exemplified by PEDOT patterns on PET as shown in **Figure 3.14b**.

The thin metal film deposited on a polymer film can also be 'cut' into the metal grating structures as VIP makes sufficiently deep indentations into the polymer substrate. For example, a 50 nm-thick Au film coated on a PET substrate is cleanly cut to form discrete lines (**Figure 3.14c**). Similar is for an Al layer on a polycarbonate (PC) substrate (**Figure 3.14d**); the debris generated by the fracture of Al due to its lower toughness can be removed by subsequent cleaning such as ultrasonic agitation.

Since the tool does not touch the substrate surface between indentations in well-controlled VIP, the grating structure first formed by VIP along one direction is not disturbed by the subsequent VIP process along another direction. This allows sequential VIP processes on the same substrate to create multidimensional pattern structures. **Figure 3.14e** demonstrates the two-dimensional (2D) grating structure faithfully fabricated by two VIP processes sequentially performed in orthogonal directions. Note that such flexibility is difficult to obtain in conventional NIL or in the inscription-based methods such as DNI and NCL. Hence, VIP can provide a practical alternative to easily and rapidly create 2D patterns which are useful for certain optical and electronic applications. For example, such 2D micro/nano-patterns can be adapted to the light-trapping surfaces in photovoltaic cells to increase the energy conversion efficiency[211, 212].

3.5.4 Real-time fabrication of period-variable chirped gratings

The period-variable, namely, 'chirped' gratings are useful for a variety of applications ranging from light dispersing devices to high-power ultrafast lasers[213-215], but the fabrication of chirped gratings has mostly relied on e-beam lithography of very low processing speed. Recent effort to produce chirped gratings in faster and more straightforward way has been made based on gradually increased surface strain from the stretched PDMS with geometric gradient[216], but the precise pitch control is still challenging because it needs a delicate pre-fabrication step for the PDMS stamps that cannot be modified during the process.

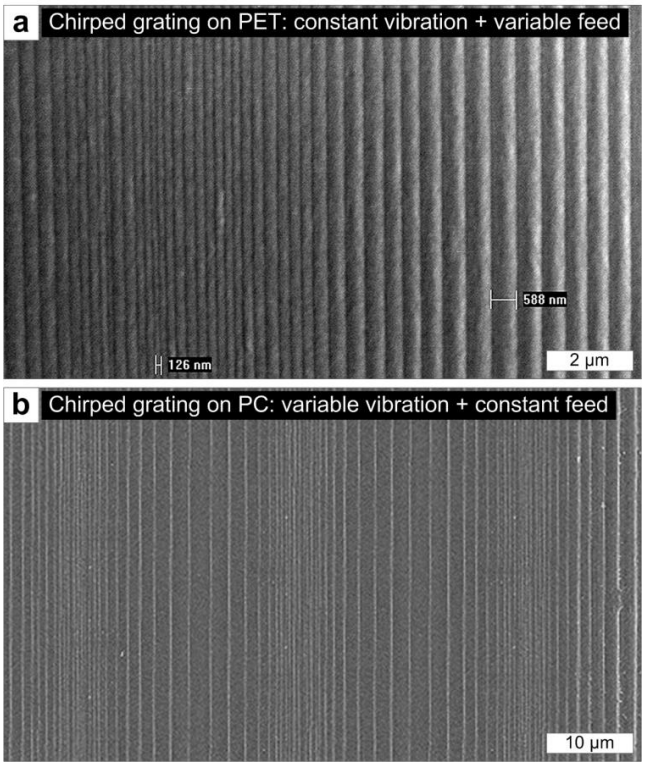

Figure 3.15 Grating patterns having variable periods (chirped gratings) fabricated by VIP in a single process (a) on a PET substrate by modulating the substrate feeding speed between 25 and 120 μm/s under constant 200 Hz vibrational indentations, and (b) on a PC substrate by modulating the vibration frequency between 40 and 200 Hz under constant 100 μm/s feeding.

Providing a breakthrough solution, VIP enables a single-step fabrication of chirped grating structures by 'real-time' modulating the indenting frequency and/or substrate feeding speed during a single process. **Figure 3.15** demonstrates chirped gratings fabricated in two ways; periods are real-time varied by either modulating the substrate feeding speed between 25 and 120 $\mu m\ s^{-1}$ under constant 200 Hz vibration (**Figure 3.15a**) or modulating the vibration frequency between 40 and 200 Hz under constant 100 $\mu m\ s^{-1}$ feeding (**Figure 3.15b**). This process is especially practical as it can be performed in a very simple, single stroke without the need of stamps. Such grating patterns having steeply varying periods can further be applied to optical color filters[217] and plasmonic antennas[218].

3.5.5 Fabrication of angle-tunable blazed gratings and application to IR polarizers

VIP trenches are intrinsically of V-shaped profiles (i.e. blazed grating) as originating from the indentation of a right-angle cleaved Si edge. Blazed grating structures have served as essential components for optical diffractions[219] and derivative applications such as optical demultiplexers[220], beam deflectors[221], and field-of-view enhancement in imaging systems[222]. However, fabrication of blazed gratings has typically relied on diamond ruling or complex procedures involving reactive ion-etching and/or wet-etching of masked substrates in tilted angle[223, 224].

Here VIP provides a facile, mask-free route to creating an angle-tunable blazed grating in a single step by controlling the indenting angle θ, as depicted in **Figure 3.16a**. **Figure 3.16b** shows the cross-sections of blazed gratings fabricated on perfluoroalkoxy

(PFA) films by VIP at different tool-tilting angles, demonstrating successful and easy control of the blaze angles. As the process is purely based on mechanical deformation free from chemical or wet process, a very clean and smooth sawtooth profile can be obtained, as confirmed by the AFM profiling over the ~5 μm-period 20°-blazed grating fabricated on PC (**Figure 3.16c**). Smooth surface is essential for high performance optical blazed gratings.

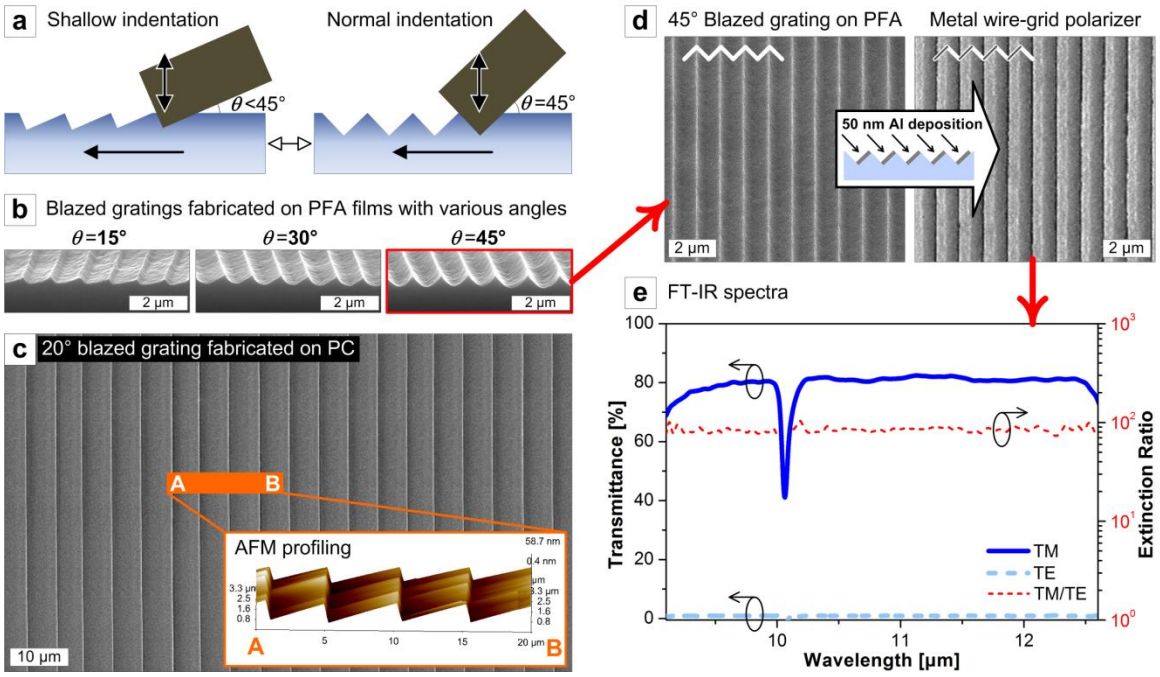

Figure 3.16 Schematic illustrations of blaze angle control by adjusting the tool tilting angle in VIP. (b) Cross-sectional SEM images of blazed gratings fabricated on PFA by VIP with different tool tilting angles. (c) 20° blazed grating structure with 5 μm period fabricated on PC. Inset to (c) shows the enlarged topology characterized by AFM across the four pitches, indicating clear blazed grating profile. (d) SEM images of 45° blazed gratings formed on PFA, before (left) and after (right) 50 nm Al shadow evaporation. (e) Measured TM and TE transmission from the Al-deposited 45° PFA blazed grating using polarized incident IR light, along with calculated extinction ratio (TM/TE).

The 45°-blazed grating structure formed on a transparent film can function as micro-prism arrays that can be used in light guide plates[225] or diffusion films[226] in

liquid crystal display (LCD) panels. Furthermore, when one side of prism planes is covered with metal, the structure conducts directional transmission of incident light that realizes autostereoscopic three-dimensional displays[227]. Here we show another application by demonstrating a metal wire-grid polarizer, which is fabricated by shadow-evaporating a 50 nm-thick Al layer on one side of the 45°-blazed grating on a PFA film. The period of a blazed grating used is ~ 1 μm, which works for mid-IR range. **Figure 3.16e** shows the optical transmission of transverse-magnetic (TM) and transverse-electric (TE) modes measured on Fourier transform infrared spectroscopy (FT-IR) by using the polarized incident IR light. The structure achieved ~80 % transmission in TM mode with well-suppressed (< 1 %) TE transmission. The extinction ratio (i.e. ratio of TM to TE transmission) is quite uniform at ~85-90 in the measurement range. The transmission dip emerging in ~10 μm wavelength originates from the specific absorption of the PFA substrate, which can be removed by using different substrate materials.

3.5.6 Summary

We have demonstrated Vibrational Indentation-driven Patterning (VIP), a template-free, high-throughput patterning technique, that realizes continuous, period-tunable fabrication of micro/nano-scale gratings by vertical indentations of a vibrating flat tool edge on a moving substrate. As VIP is based on mechanical deformation, any materials softer than the tool can be patterned in one- or multi-directions with full control of grating periods. Real-time modulation of vibration and substrate feeding enables a single-step fabrication of chirped gratings. The blazed gratings with various blaze angles can also be readily created by adjusting the tool tilting. With its simple control and great

versatility, VIP may be applicable to continuous and scalable fabrication of functional gratings and find further applications in optics, electronics, and energy conversion.

Chapter 4

Scalable Integration of Bottom-up Nanostructures and Top-down Nanofabrications toward Pragmatic Nanoelectronics

4.1 Scalable manufacturing of functional nanostructures toward practical benefits: chapter overview

'Combining' the continuous, high-throughput nanomanufacturing methodologies with multiscale, functional nanostructures, this thesis project approaches its eventual goal stated in Chapter 1: the scalable implementation of functional nanodevices to bolster our community. Indeed, this spirit has already been materialized in the previous chapters in a series of formats including the photoelectric energy converters and photonic devices directly fabricated through 3-D hybrid assembly and scalable nanomanufacturing highlighted by R2R process in previous chapters.

Not limited to the novel methodologies presented so far, conventional techniques such as photolithography may also be integrated in ingenious fashion in order to realize more viable applications. This chapter in that regard moves forward in two ways; (1) the ZnO/CNT hybrid system will be demonstrated in more scalable version by adopting mechanical rolling process toward rapid-responsive photodetectors and high-photocurrent

generators, and then (2) Photo Roll Lithography (PRL) which integrates conventional photolithography and novelly invented rollable processing will be presented along with its application to transparent conducting electrodes and IR polarizers.

4.2 ZnO/CNT hybrids fabricated via scalable roll processing

As discussed in Chapter 3, Zinc oxide (ZnO) nanowires exhibit UV-induced photoelectric characteristics and therefore have been extensively used in photodetectors and light emitters[51, 77, 146, 228, 229]. Also, the sensitivity of their properties to surface effects has enabled a variety of chemical and biological sensors[50, 58-61], such as gas sensors that modulate the ZnO conductivity by interaction with the oxygen molecules on the ZnO surface[50]. However, because such functional nanowires (NWs) are typically grown as electrically isolated structures surfaces having low electrical conductivity, post-processing such as harvesting, positioning, and/or metalizing are often required to make use of those functional properties in electrically addressable fashion. In the same regard, it remains challenging to build “macroscopic” architectures that take advantage of such functionalities beyond the single-nanowire level..

One attractive strategy to build functional and electrically communicable macroscopic architectures is to directly fabricate nanostructures such as ZnO NWs on conductive frameworks[171]. This provides a means to make electrical contact to a large number of functional nanostructures in parallel, and to amplify the NW-driven signal intensity above ambient noise levels, alleviating challenges in electrical readout. Moreover, it is desirable for such frameworks to be compatible with thin film processing, and even with emerging printing methods for flexible systems.

In particular, multi-walled (MW) carbon nanotubes (CNTs) are an attractive framework due to their electrical conductivity[16], mechanical[230, 231] and chemical robustness[232], and high flexibility[233]. Moreover, CNTs can be manipulated after synthesis to form horizontally-aligned (HA) CNT sheets[139], three-dimensional (3D) micro-features[234], and indefinitely long yarns[235]. It has been shown that ZnO NWs (herein abbreviated ZNWs) can be directly grown on CNTs via a low-temperature vapor-solid (VS) growth mechanism, where Zn is supplied by evaporation of Zn metal at 500-600 ℃[116, 228]. This process was adapted to build hybrid 3D architectures comprising ZNWs on CNTs configured in vertically-aligned (VA-) forests and HA-sheets fabricated by mechanical rolling of patterned VA-CNT forests.

We fabricate hybrid ZNW/CNT sheets by scalable CVD, rolling, and printing methods that can be integrated with lithographic processing. Then we systematically investigate the unique photoconductive characteristics of hybrid thin films, attributed to charge carrier transport through the anisotropic CNT network and rapid electrical interactions between hierarchically organized ZnO and CNTs. The films exhibit highly anisotropic photoconductivity, governed by the enhancement of CNT-CNT contacts by ZnO. The conformal Ohmic interface of ZnO and CNTs enable rapid photoresponse (i.e. sub-second) upon pulsed illumination as compared to ZnO thin-film photodetectors whose response time can be as high as minutes to hours[147]. Moreover, the ZnO-CNT hybrid exhibits a large photocurrent of μA-mA, compared to ~nA levels measured for the devices based on a single ZNW[236, 237] or ZNW arrays[238-240], at comparable UV illumination intensity. The amplitude and direction of the photocurrent are controlled by competition between the built-in potential of ZnO and the externally applied bias.

4.2.1 Fabrication of scalable ZnO/CNT hybrid thin films

The hybrid nanostructured film comprising ZNWs directly grown on a HACNT sheet was fabricated via sequential CVD processes. First, a VA-CNT "blade" array was grown on Fe catalyst lines (patterned by photolithography) by atmospheric pressure CVD using C_2H_4 as the carbon feedstock[78]. Next, the CNT blades were mechanically rolled and then exposed to a solvent vapor, resulting in a continuous HACNT sheet where the individual blades overlap like toppled dominos (**Figure 4.1a**)[139]. Then, ZNWs were directly grown on this HACNT sheet (**Figure 4.1b**) via a low-pressure CVD method using Zn foil as the source material[116, 228]. Scanning electron microscopy (SEM) images of the HACNTs before and after ZNW growth are shown in **Figures 4.1c and 4.1d**, respectively. Notably, though this step requires oxygen to form ZnO from vaporized Zn, it does not degrade the CNTs because the CNTs are safe from oxidative degradation at the process temperature of 600 ℃. Owing to the vapor-solid growth mechanism of ZnO, in which a surface roughness is essential to initiate seeding of ZnO nanoclusters[140], ZNW are formed selectively at high density on the CNTs while few ZNWs are found on the surrounding smooth substrate[228].

In order to measure the *I-V* characteristics, Au electrodes are deposited at both ends of the HACNT sheet prior to ZNW growth. Optionally, another Au electrode is deposited on top of the ZnO in order to characterize the ZnO-CNT heterojunction as discussed later. Based on the direction of current flow with respect to the alignment of the CNTs in plane (**Figure 4.2**, insets), we designate the parallel (PRL) device as having Au electrodes along the substrate edges perpendicular to the CNTs, and the perpendicular (PPD) device as having Au electrodes along the edges parallel to the CNTs. Therefore the

PRL device is used to measure transport primarily along the CNTs, whereas the PPD device is used to measure transport in the perpendicular direction which is dominated by CNT-CNT junctions.

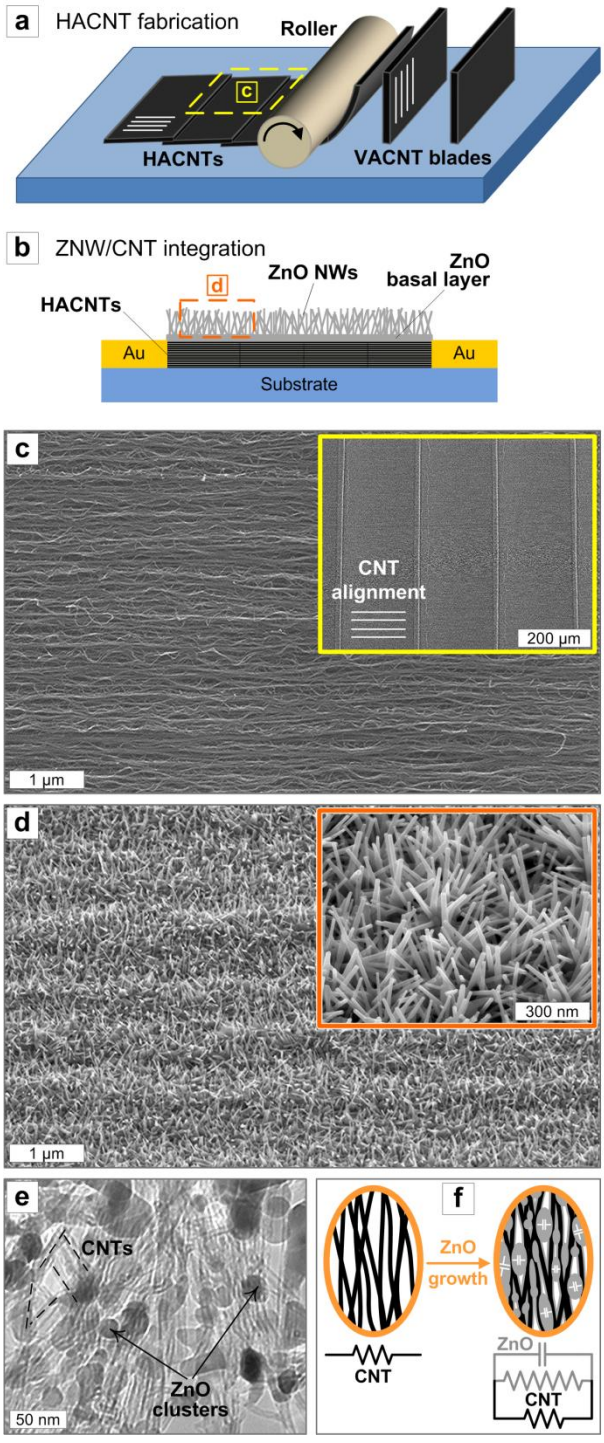

Figure 4.1 Fabrication of ZnO/CNT hybrid devices: (a) Perspective view of the mechanical rolling process to transform the vertically-aligned CNT (VA-CNT) blades into horizontally-aligned CNT (HA-CNT) sheets serving as electrically addressable substrates for subsequent ZNW growth. (b) Side view of the conformal ZNWs directly grown on the Au-deposited HA-CNTs; Au electrodes are deposited on both ends of HA-CNTs prior to ZNW integration in the way the electrons flow either along (i.e. parallel (PRL) configuration) or across (i.e. perpendicular (PPD) configuration) the CNT alignment direction. (c) SEM image of an as-processed HA-CNT; inset shows low-magnification view, disclosing the height of VA-CNT blades is controlled for them to be slightly overlapped with each other when rolled down, forming a continuous, scalable HA-CNT sheet. (d) SEM image of ZNW-grown HA-CNT surface, indicating high-density ZNW structure is conformally grown on the underlying CNTs; inset reveals the enlarged view of ZNWs that are randomly oriented with approximately 25-50 nm diameter and 300-500 nm length in average. (e) TEM image taken at the initial growth stage where ZnO nanoclusters are being formed between the CNT strands and (f) its schematic (top) and circuit (bottom) diagrams comparatively demonstrating the electrical connection of ZnO over the neighboring CNTs.

4.2.2 Anisotropic electrical and photoconductive properties

For both PRL and PPD configurations, the device conductivity increases after ZNW/ZnO growth due to the electrical contribution of the semiconducting ZnO coating on the CNTs[228]. **Figure 4.2** shows the *I-V* curves measured under continuous voltage sweep before and after ZnO growth. The increase in conductivity is much greater in the PPD configuration (340%) than the parallel configuration (13 %) as indicated in **Table 4.1**. This anisotropy in electrical conductivity is because the ZnO deposited on the CNTs plays a greater role in improving the connectivity of CNT-CNT junctions which dominate transport in the perpendicular direction, compared to the conduction along the CNTs. It has been shown previously that CNT-CNT conduction is dominated by electron hopping[141], and we expect that the nanoscale ZnO contacts significantly reduce the contact resistance between the CNTs in the HA-CNT sheets. This argument was experimentally clarified by the transmission electron microscopy (TEM) imaging of the ZnO/CNT hybrid structure (**Figure 4.1e**) where the growth process was halted on purpose at the initial ZnO nucleation stage. It can be seen that ZnO nanoclusters are attached across the multiple CNT strands, which will be followed by additional nucleation for further connections and ZNW growth to cap all.

When the device is illuminated with UV light (365 nm peak wavelength, corresponding to ≈3.4 eV) having photon energy exceeding the ZnO bandgap (≈3.37 eV), a proportional increase in DC conductivity is observed due to the photogeneration of charge carriers in ZnO (i.e. electrons in n-type ZnO). As indicated in **Figure 4.2** along with **Table 4.1**, this increase is more pronounced in the PPD (13-23 % increase from UV-off status) than the PRL case (1.6-3.5 % increase from UV-off status). Once again, this is

due to the critical role of ZnO in CNT-CNT conduction in the PPD configuration. The change in conductivity of ZnO upon UV illumination has a greater influence on CNT-CNT junction contact than on conduction along the path parallel to the CNTs.

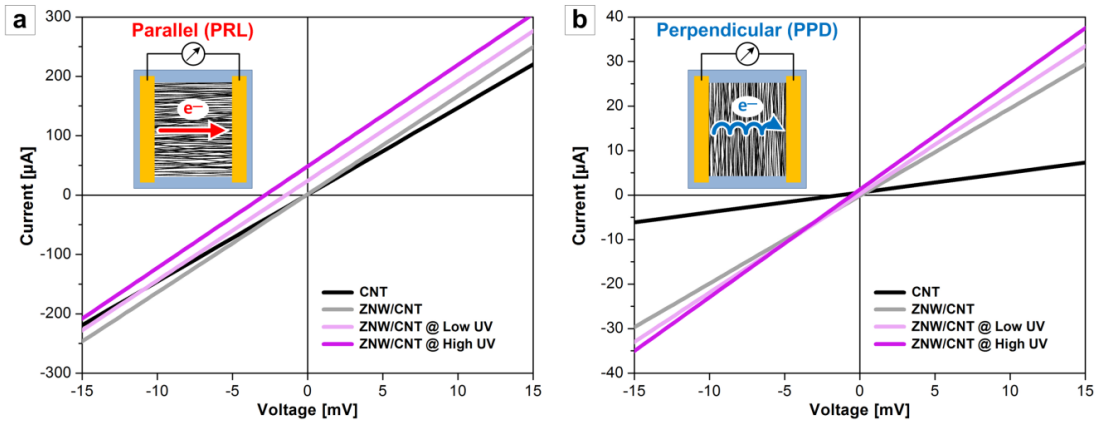

Figure 4.2 *I-V* plots of the ZnO/CNT hybrid devices in (a) PRL and (b) PPD configurations. The measurements were first performed before and after ZNW growth without UV illumination, indicating the conductivity is improved by the electrical reinforcement of semiconducting ZnO. ZnO-driven photoconductivity is characterized by illuminating the continuous UV light with low (1.4 mW/cm^2) and high (7.5 mW/cm^2) power densities, demonstrating the conductivity is further enhanced by UV-induced photoconductivity. The values and increase %'s of conductivities are listed in Table 4.1.

Table 4.1 Electrical conductivities of hybrid ZNW/CNT structures, and effect of illumination on conductivity. UV intensities "low" and "high" represent 1.4 mW/cm^2 and 7.5 mW/cm^2, respectively.

	Parallel to CNTs (PRL)			**Perpendicular to CNTs (PPD)**		
	Conductivity [S/cm]	% Increase from CNT	% Increase from ZnO/CNT	Conductivity [S/cm]	% Increase from CNT	% Increase from ZnO/CNT
(HA-)CNT only	60.7	-	-	1.7	-	-
ZnO/CNT	68.5	12.9	-	7.3	340	-
ZnO/CNT + Low UV	69.6	-	1.6	8.2	-	12.6
ZnO/CNT + High UV	70.9	-	3.5	9.0	-	23.0

4.2.3 Rapid photoresponse dynamics

The fast photo-switching speed of is one of the most prominent features of our ZnO/CNT hybrid architecture. We investigate the photoresponse dynamics by applying pulsed UV illumination which generates the photocurrent peak from the background. **Figure 4.3a** discloses a close look of photocurrent peak generated in phase with the pulsed UV irradiation of 2-second temporal width for the PRL device without external bias. The pulse width is set much longer than the rise and decay time of the photocurrent. Defining the rise time as the time required for the photocurrent to reach at 90 % of the peak value, and the decay time as one to restore to 10 % of the peak value[241], both the rise and decay responses are as swift as 0.3 ± 0.05 s. These rapid dynamics stand good regardless of the CNT alignment direction and bias existence (not shown here). Note that this is unusually fast as compared to typical response times of conventional ZnO-based photodetectors that are on the orders of a few tens of seconds to even hours[51, 146-148].

4.2.3.1 General photoconduction mechanism of ZnO

The photocurrent generation in ZnO has been studied extensively and is well-established. In the absence of UV light, oxygen is adsorbed on the ZnO surface by taking a free electron from n-type ZnO to form a chemically adsorbed surface state. Under the exposure of UV light with the energy exceeding the ZnO bandgap, excitons are generated and then separated to electron-hole pairs inside the ZnO. While the holes are trapped on the ZnO surface, the unpaired electrons are free to flow to produce photocurrent[49]. Namely, ZnO belongs to photoconductors rather than photodiodes as the UV-induced charge flow in the ZnO is dominated by the excessive electrons in a unipolar

manner[242]. Despite its straightforward photoconduction mechanism, the ZnO-based thin film photodetectors often suffer from the intrinsic large ZnO resistivity which mainly results in high recombination rate and slow dissipation of excess charge carriers[243].

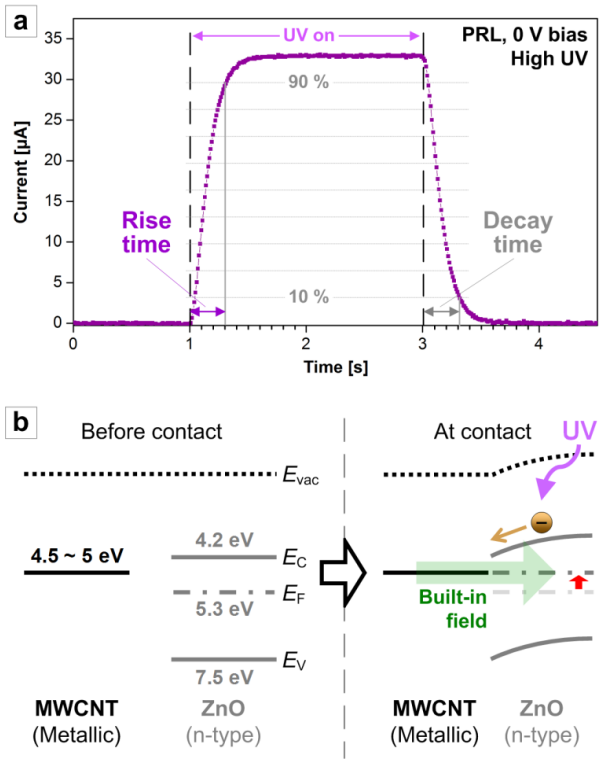

Figure 4.3 (a) Photoresponse of the ZnO/CNT hybrid device in PRL configuration under a 2-s duration UV pulse of the power density of 7.5 mW/cm^2 (i.e. High UV) without external bias. The plot indicates the photoresponse time is as rapid as ~0.3 s; (b) Band diagrams before (left) and after (right) the contact is formed between ZnO and CNTs, demonstrating the built-in potential is formed in the way from CNTs to ZnO at contact.

4.2.3.2 Rapid transport mechanism in ZnO/CNT hybrids

In our ZnO/CNT architecture, the metallic CNTs are electrically connected to the thin ZnO layer. **Figure 4.3b** illustrates the energy band diagram of ZnO-CNT system. Under the equilibrium state, the Fermi energy level of ZnO is aligned to that of the CNT as the ZnO work function (≈5.3 eV) is larger than CNT's (4.5-5.0 eV). Accordingly, the ZnO-CNT forms Ohmic interface and the 'built-in' potential is generated in the direction

from CNTs to ZnO. Along this potential slope, the free electrons photogenerated in ZnO can therefore be favorably transported to CNTs. The metallic CNTs may allow higher mobility of these excess charge carriers and thus reduce recombination until they are extracted to the external circuit by diffusion along whichever the contact resistance is lower. Furthermore, the intimate Ohmic contact between ZnO and highly conductive CNTs enables the UV-generated excess charges to be rapidly transported to CNTs and then to external circuit. The nanostructured large interfacial contact may further facilitate quick discharge of remaining excess charge carriers when the UV is turned off.

4.2.4 Photocurrent characterizations: performance evaluation and application perspective

We now systematically characterize the photocurrent generation for PRL and PPD devices under 5 s-duration UV pulses by varying UV intensities and bias voltages (**Figure 4.4**). The amplitudes of photogenerated currents were indicated by the difference between peak and ground values in **Figures 4.4a-c**. The corresponding current densities were then calculated per unit cross-section of the HA-CNT films, and are plotted in **Figure 4.4d** with the relative increase %'s from the zero-bias values.

Under UV illumination without any external bias, the ZnO/CNT film behaves like a photovoltaic (PV) cell as it produces a considerable amount of photocurrent with no external power source. This confirms the energetically favorable transport of photogenerated electrons from ZnO to CNTs discussed above. Moreover, the ZNWs may facilitate more efficient UV absorption by providing much larger surface area as compared to simple ZnO thin films. When the external bias is engaged (**Figures 4.4b and**

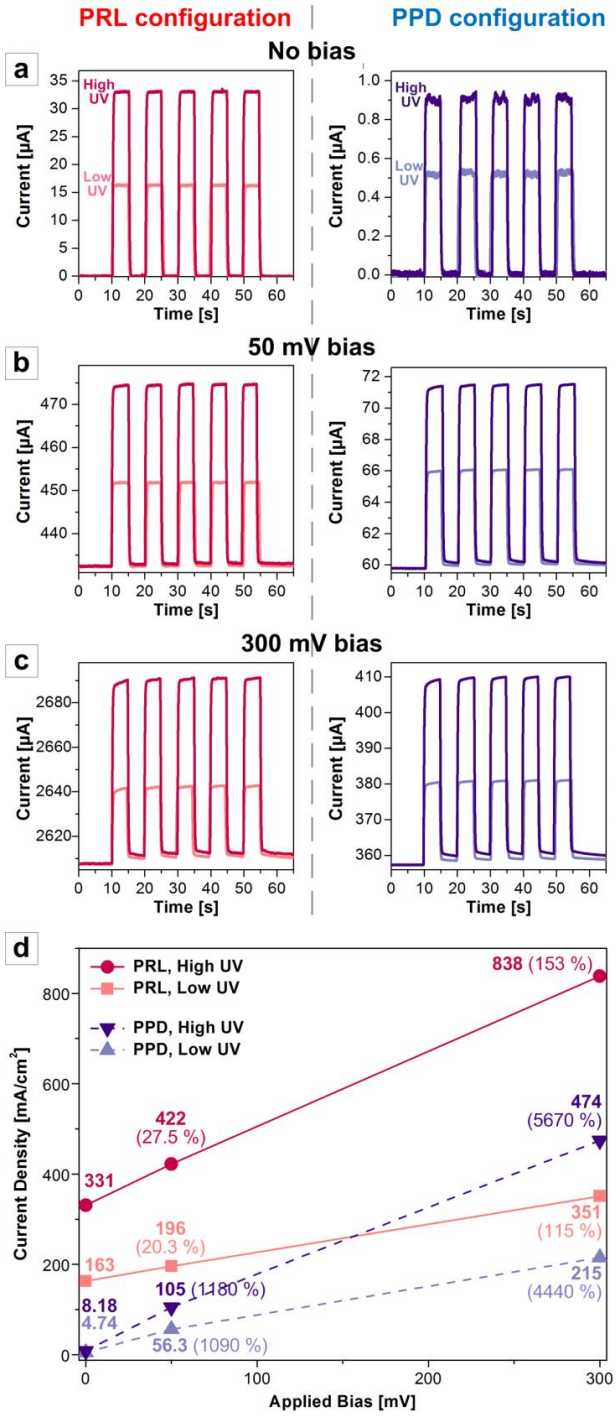

Figure 4.4 Photocurrent dynamics of ZnO/CNT hybrid devices upon pulsed UV illumination under the biases of (a) 0 V, (b) 50 mV, and (c) 300 mV for PRL and PPD configurations. Dark and shaded curves are taken from the high (7.5 mW/cm^2) and low (1.4 mW/cm^2) UV intensities. The photocurrent densities calculated per unit cross-sections of the PRL and PPD devices are plotted in (d) where their values and relative increase %'s with respect to the 0 V-bias values are also presented.

4.4c), larger current can be collected under the same UV intensity as the electron flow is further accelerated via field-induced drift. Also, the photocurrent increases proportionally with respect to the incident UV flux, which is manifested by the same slope for the same UV intensity in **Figure 4.4d**. This is consistent with the theoretical approximation roughly given as $I_{ph} \sim V\Phi_{ph}$ [244], where I_{ph} , V, and Φ_{ph} are photocurrent, external bias, and incident photon flux, respectively.

The intrinsic capacitance of ZnO is responsible for the transient charge-discharge behavior observed in photocurrent curves, especially under external bias (**Figures 4.4b and 4.4c**). The photocurrent once generated upon UV illumination charges this ZnO capacitor, which is manifested by gradual increase in photocurrent until reaching at the peak; when the illumination is turned off, the rate of decay is also governed by the discharge rate of the ZnO capacitors. Because the ZnO capacitance is proportional to the electric field[245], this charge-discharge behavior originating from ZnO capacitance becomes more apparent when the external bias is applied.

The external quantum efficiency (EQE), defined as the ratio of the number of electrons photogenerated (per second) to the number of incident photons (per second), is popularly used to evaluate the performance of photodetectors or photovoltaic cells[242]. The EQEs currently we achieve under the 300 mV bias and incident UV power density of 1.4 mW/cm^2 are calculated up to 36 % for PRL and 21 % for PPD devices, which are already comparable to the previously reported EQEs from other types of photodetectors[242]. Interestingly, these EQEs at 300 mV bias decrease to 16 % for PRL and 9 % for PPD devices under higher UV illumination of 7.5 mW/cm^2, indicating that the HA-CNT channel currently designed to 1.5 μm thickness cannot afford all photons

provided by the higher UV illumination. We assume that the excess energy from the photons not contributing to generating electron charges is wasted via other types of energy including thermal loss. Hence, the EQE of hybrid ZnO/CNT photodetectors can be potentially further improved by optimizing the structural parameters (e.g. HA-CNT thickness) and/or tuning the incident UV intensity.

The measured photocurrent density of our ZnO/CNT hybrid devices is significantly higher than those of other ZnO-based photoelectric devices either relying on bare ZnO thin films[246] or using ZNWs but not employing CNTs[247]. We also note that our photocurrents are generated under low-voltage consumption at zero or sub-1V biases (i.e. 50-300 mV) whereas previous ZnO-based photoelectric structures typically require a few to hundreds of volts. In this regard, our architecture may be applicable to the scalable and high-current photoelectronic devices that can operate at low power or potentially be self-powered.

Moreover, as shown in **Figure 4.4d**, the photocurrent densities generated under the pulsed UV input are greater in the PRL configuration due to the high conductivity along the aligned CNT axes, while the increase ratios are more drastic in PPD configuration where ZnO has dominant contribution to the total conductivity. This is analogous to the *I-V* sweep results under continuous UV illumination discussed above. Owing to these high photocurrents, we could confirm high signal-to-noise ratios (SNRs): e.g. ~1100 in the PRL and ~30 in the PPD from **Figure 4.4a**, both of which are sufficiently high to overcome electrical and thermal noises on the order of hundreds of nA's. This anisotropic photoelectric behavior along with the rapid photoresponse can be exploited to develop fast-responsive devices working independently or simultaneously as

a high photocurrent generator in the PRL direction and a more sensitive photodetector along the PPD direction within a single ZnO/HA-CNT cell.

4.2.5 Characterization of ZnO-CNT junctions

Fabrication of another Au electrode on top of the middle section of the ZnO/CNT hybrid film as shown in **Figure 4.5a** (i.e. Au-ZnO-CNT-Au) let us investigate the ZnO-CNT (semiconductor-metal) junction behavior. Here we compare the PRL and PPD configurations again and investigate the influence of the direction of applied bias. To reverse the bias direction, the probes connected to the measurement system were switched.

As schematically remarked in **Figure 4.5b**, the built-in potential has simply aided rapider electron extraction from ZnO to CNTs that actually connect two electrodes and carry most current in the ‘symmetric’ configuration. Now the built-in potential directionally affects the current flow as ZnO and CNTs are connected in series in this ‘asymmetric’ configuration, meaning it serves as a direct factor to determine the net current direction. In order for further clarification, **Figure 4.5c** shows the equivalent circuit diagrams for each case.

The built-in potential formed across the ZnO-CNT interface is always in the direction from CNTs to ZnO due to bend bending discussed in **Figure 4.3b**. Hence, without any external bias, the photogenerated excess electrons in ZnO preferentially flow from ZnO to CNTs (**Figure 4.5d**). Such effect is confirmed by the (+/-) sign of current signals indicating exactly the same amplitude but with the reversed sign when the measurement reads are switched.

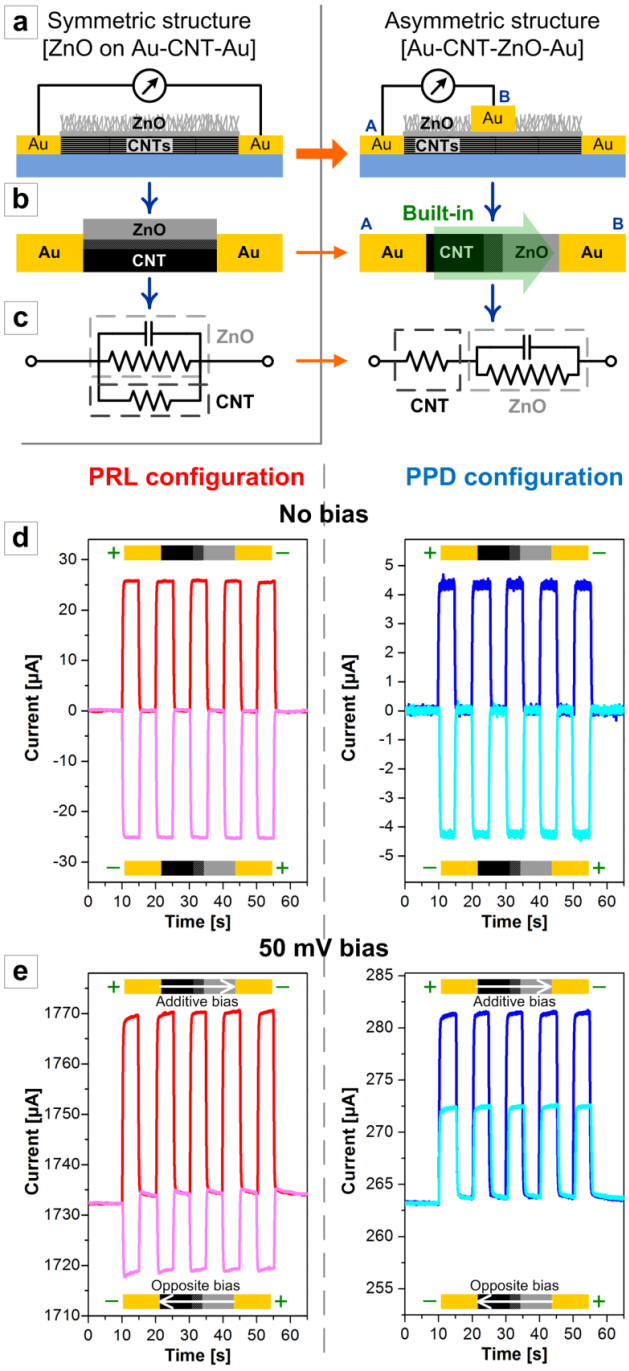

Figure 4.5 (a) Fabrication of asymmetric Au-CNT-ZnO-Au structures starting from the symmetric ZnO/CNT device (left) by depositing another Au electrode on ZnO-grown area (right). The equivalent diagrams of (b) structural schemes and (c) electrical circuits are illustrated, demonstrating the electrons must flow 'across' the ZnO-CNT junctions to be collected by the system. Photoelectrical characterizations of the ZnO-CNT junctions upon pulsed UV illumination under the biases of (d) 0 V and (e) 50 mV for PRL (left) and PPD (right) configurations, respectively. The read direction and/or bias applying direction are described on top or bottom area of each plot for clarification.

Now the external bias when applied, and the existing built-in potential determine the photocurrent amplitude and direction depending on their directions and CNT alignment. When the external field is applied in the same direction as the built-in potential (i.e. “additive” bias), the band bending deepens to form higher electric field at the interface. This promotes more of the photogenerated excess electrons in ZnO to be transported to CNTs, thereby increasing the photocurrents flowing from CNTs to ZnO for both PRL and PPD cases (**Figure 4.5e**). Since the external bias is applied across the ZnO capacitors as well, some of the photogenerated excess electrons contribute to charge the ZnO capacitors under UV and are discharged when the UV light is off. This is shown as transient charge-discharge behavior in photocurrent dynamics.

On the other hand, when the external bias is applied along the “opposite” direction to the built-in field (i.e. “opposite” bias), the net electric field across the ZnO-CNT junction is universally decreased after compensating the built-in field, reducing the UV-induced photocurrent amplitudes for both PRL and PPD cases (**Figure 4.5e**). In other words, there should be a certain amount of current always flowing along the built-in potential when free electrons are generated, which is determined by the system resistance (i.e. $I = V/R$). This presents that the current induced by the built-in potential is much smaller in PPD configuration due to its larger resistance. Apparently it is even smaller than the photocurrent generated under the opposite bias as the net current direction in the PPD device is reversed, indicated by the same (+) sign of current although the measurement reads are switched. In the PRL configuration, however, the net current direction remains unchanged, as indicated by the (-) sign with the switched reads. This means the current induced by the built-in potential is still larger than that from

photogenerated excess electrons because of much higher conductivity of CNTs aligned along the charge flow direction. In both PRL and PPD cases, the quick change in the net current upon UV pulses is always followed by the charging behavior since excess charges are still used for charging capacitors. When the UV is turned off, the current restores to the initial level while the ZnO capacitors are discharged again since there are no more excess charges provided.

4.2.6 Summary

We have developed the ZNW-decorated ZnO/CNT hybrid photoelectronics by directly integrating ZnO nanostructures onto the scalable HA-CNT templates via low-temperature VS growth method. Due to the great electrical conductivity, the ZnO/CNT hybrid photoelectric device can create a considerable amount of photocurrent under UV illumination even without the external power source, demonstrating it can serve as the UV-powered PV cell. Larger photocurrent can be readily generated by the aid of the bias. Importantly, our hybrid architecture realizes very rapid photoresponse which is attributed by the intimate Ohmic connection over the large interfacial area between ZnO and CNTs, enabling the quick transport of photogenerated electrons from ZnO to CNTs upon the dynamic UV pulses. Higher photocurrent can be extracted along the CNT axes, while relative change in photoconductivity is more pronounced across the CNT alignment direction. Hence, this scalable, electrically addressable hybrid architecture will open a way to fast-responsive, low-power drivable UV-photoelectronics that potentially can be utilized to multifunctional devices equipping such as current generation and photon detection in a single cell.

4.3 Photo Roll Lithography (PRL) for continuous and scalable micro/nano-manufacturing

(*This work is done with collaboration with Dr. Moon Kyu Kwak.*)

For decades, photolithography has been the industry workhorse for various micro/nano-scale fabrications with the well-established procedure and highly reproducible results[8]. Despite the steady progress in developing unconventional micro/nano-fabrication and patterning techniques in recent years[9, 155, 156], photolithography has remained the dominant technology due to its excellent reliability and the globally disseminated infrastructure along with the matured protocol of pre- and post-lithgraphy steps such as mask-making, etching, etc. On the other hand, there has been an increasing interest in recent years in large-area electronic[166] and photonic applications[75], especially those made on flexible substrates, where traditional photolithography has not played an important role; instead, further continuous and scalable techniques, most notably represented by the roll-to-roll (R2R) nanomiprint lithography (NIL), are flourishing for large-area and flexible pattern fabrications[159, 164]. By overcoming the limitation in scalability and throughput, it has therefore become more demanding to revitalize the photolithography technique toward large-area continuous patterning with significantly improved process throughput and reduced tool cost. An encouraging development was recently made by extending the traditional phase-shift mask photolithography[248] to a continuous process by utilzing a roll-type phase-shift mask for large-area patterning while maitaining deep sub-micron resolutions[249].

We introduce a new methedology termed Photo Roll Lithography (PRL) for

continuous and scalable lithographic patterning. This process integrates two outstanding characters of micro/nano-fabrication technology: photolithography and rollable processing, into a versatile technique that is applicable to both rigid and flexible substrate. The PRL system is created by utilizing a flexible photomask and a rollable UV exposure unit, which realizes the continuous photolithographic fabrication of a variety of faithful micro/nano-scale features on a moving substrate with high throughput. Since PRL uses a flexible and soft mask without the aid of large force or heating, it can afford the patterning on fragile substrate materials such as graphene layers. The nature of dynamic rolling in PRL further enables the geometrical modulation of outcome patterns using a single mask, simply by controlling the rotation speed of a mask-attached roll with respect to the substrate feeding speed. As an application, we demonstrate the continuous fabrication of optically transparent metal electrodes (TMEs)[250] in the form of metallic mesh pattern as well as the enhanced TMEs by patterning metal mesh patterns directly on a graphene layer using the PRL process. Then we exhibit the geometrical programmability of the speed-variable PRL which then can be applicable to the single-mask fabrication of the IR filters having tunable filtering bands

4.3.1 Process overview of PRL

Figure 4.6a depicts the PRL system which consists of three main parts: a flexible photomask, the rollable UV exposure unit, and the photoresist developing module. The flexible photomask containing the desired pattern openings is first fabricated on a 50 nm-thick Al-coated polyethylene terephthalate (PET) sheet (see **Appendix A** for experimental details). This flexible Al/PET photomask is then conformally adhered to the

outer surface of a hollow quartz cylinder using an intermediate thin polydimethylsiloxane (PDMS) layer. Inside this quartz cylinder, a 365 nm-wavelength UV lighting source is mounted and collimated to a 1mm-wide aperture. A photoresist-coated substrate is then fed by the linear stage under this photomask-attached UV-installed roll where the contact line between the substrate surface and the roll is aligned to the UV exposing aperture slit.

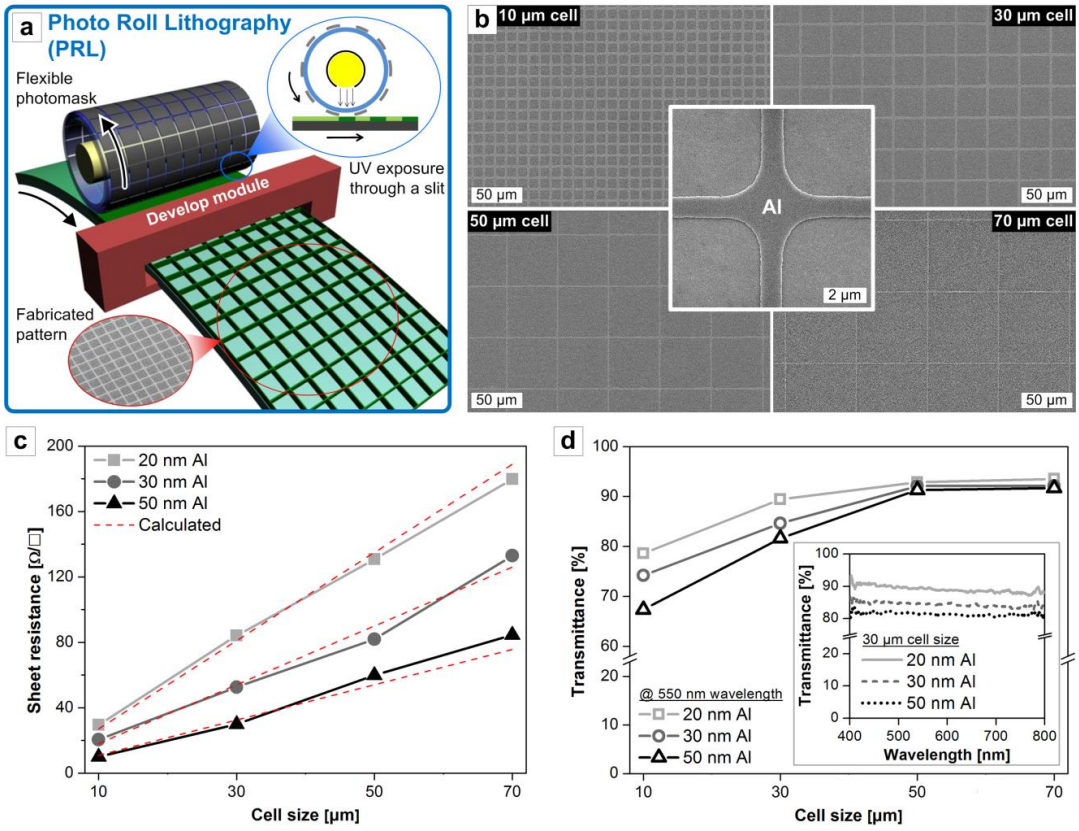

Figure 4.6 Principle of PRL and its application to TME fabrication: (a) Schematic description of the Photo Roll Lithography (PRL) process. A flexible photomask is adhered to the hollow quartz cylinder inside which a collimated UV light source is mounted (as shown in the upper right inset). As the rolling proceeds, a photoresist-coated substrate continuously undergoes UV exposure and develop steps, finalizing to the desired pattern (as shown in the lower left inset). (b) SEM images of the PRL-fabricated Al mesh-based TMEs having varying mesh cell sizes of 10, 30, 50, and 70 μm. The central inset to (b) reveals the clearly defined Al line patterns with 1 μm linewidth. (c) Sheet resistances and (d) transmittances at 550 nm wavelength of the TMEs fabricated by different period (10, 30, 50, and 70 μm) and Al thickness (20, 30, and 50 nm). Dashed lines in (c) indicate theoretically calculated values. The transmittances of the 30 μm-period samples along the entire visible range are selectively shown in an inset to (d).

The mask-substrate contact can be adjusted from the contact mode to the proximity mode; in case of contact mode, either rolling or linear feeding can drive the isokinetic mask-substrate movement by friction, while the proximity mode allows separate controls of the mask and the substrate for geometrical tuning as will be shown later. As the rolling proceeds at a speed up to 5 mm/s with the UV light on, UV light is continuously exposed through the slit, defining the photoresist patterns which are finalized after passing through the resist development process.

4.3.2 Application to transparent metal electrodes (TMEs)

To develop tangible electronic applications by utilizing the PRL process, we demonstrate the continuous fabrication of TMEs. The TME based on invisible metallic pattern was introduced several years ago as a potential candidate to replace the indium tin oxide (ITO) transparent conductor for optoelectronic applications[62, 64]. However a truly scalable manufacturing process is still lacking. Here we describe TMEs made by fabricating metal mesh pattern on either flexible (e.g. PET) or rigid (e.g. glass) transparent substrates in a continuous fashion. We first systematically investigate the Al mesh patterns made by PRL by parameterizing the Al thickness as well as the mesh cell size, then demonstrate the PRL processing of Al mesh patterns on a graphene layer to further improve the perfomance of TMEs for broader range of applications. After the flexible photomask containing designed mesh patterns is prepared and attached to the roll, PRL was performed in contact mode over the photoresist-coated transparent substrates having either a metal layer or a metal/graphene layers, followed by resist development and wet-etching processes.

Figure 4.6b shows the scanning electron microscope (SEM) images of the fabricated Al mesh patterns with the cell sizes varying from 10 to 70 μm. Inset to **Figure 4.6b** zooms into the point of intersection of crossing Al lines with 1 μm linewidth. The sheet resistances of the fabricated TME samples of each cell size having varying metal thicknesses of 20, 30, and 50 nm were measured and plotted with the theoretically calculated values in **Figure 4.6c**. The measurements and calculations show a good agreement within 10 % deviation, validating the precise patterning capability of the PRL process. A slight mismatch between the measured and calculated values might result from the defects (e.g. metal line disconnections) and/or the natural oxidation of Al. **Figure 4.6d** shows the transmittance measurements of the TME samples fabricated on glass substrates, with a bare glass as a reference. To avoid the complexity and show the trend more clearly, we collected single-point transmittance values per each sample at 550 nm wavelength from the sweeping measurement along the visible wavelength regime (i.e. 400-800 nm). As exemplified with the 30 μm cell data in the inset to **Figure 4.6d**, the transmittance values appear almost constant over the entire visible wavelength range, which is highly desirable in most of the applications.

There is a trade-off between sheet resistsance and transmittance of the fabricated TMEs; the transmittance increases with decreasing Al thickness or increasing cell size, both of which can cause increase in sheet resistance. Nevertheless, it can be seen that dependence of the transmittance on Al thickness becomes very small as the cell size increases (i.e. 50 and 70 μm) because the areal coverage of transparent opening becomes more dominant. The trade-off between sheet resistance and transmittance can therefore be optimized at the mesh cell size of 50 μm in our studied parametric space. Certainly the

cell geometry is not limited to square, but can also be other shapes such as hexagon. One can further taylor the desired TME specification by choosing the proper metal thickness and the cell size, both of which can be fully controllable and readily processable in PRL.

4.3.3 Incorporation of graphene for improved TMEs

While the TME fabricated by the PRL has suitable resistance and transparency for touch panel application, the spacing between the metal lines is too large for it to be used directly in other optoelectronic devices such as organic light-emitting diodes (OLEDs) or organic photovoltaics (OPVs), where charge injection or collection occurs uniformly across the transparent electrode. This problem can be solved by adding a highly conductive layer to form a composite electrode structure [65, 251]. Another strategy is to incorporate a graphene layer to distribute the current. Having excellent electrical property and high optical transparency[252], a single- or few-layer graphene film transferred onto the transparent substrate can directly serve as transparent conducting electrodes[253, 254]. However the sheet resistance of the graphene film itself is still too large for many optoelectronic applications, e.g. OLED and OPV. The overall conductivity can be improved with little decrease in transmittance when the graphene layer is incorporated with metal grid patterns[255]. However, it could be challenging to conformally cover the graphene layer over the metal patterns in large scale without damaging or leaving residual stress on graphene.

In this regard, we fabricate the metal mesh patterns directly on top of graphene by using PRL. Since in PRL a flexible photomask cushioned by a PDMS pad makes a soft contact to the substrate and patterning proceeds without much force, a flat graphene layer

covered by a thin metal layer can remain intact throughout the PRL patterning. **Figure 4.7a** depicts the overall fabrication procedure of graphene-incorporated TMEs (G-TMEs). We used single- or multi-layer graphenes and varied the metal thickness and mesh dimension depending on the targeted function. Either glass or PET film was used as a transparent substrate; **Figure 4.7b** shows the graphene film transferred to PET. After the

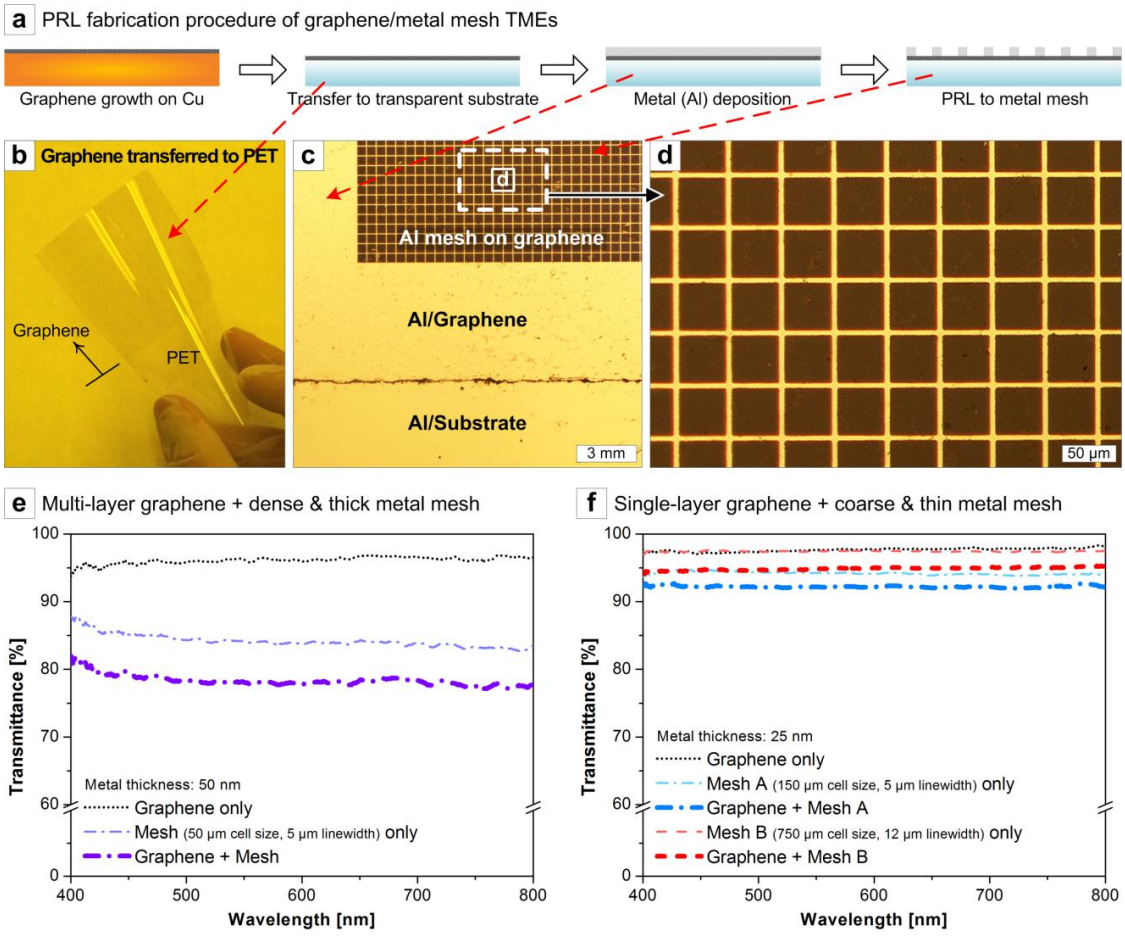

Figure 4.7 Incorporation of graphene to PRL for improved TME fabrication: (a) Schematic illustration of overall G-TME fabrication procedure. An as-grown graphene is transferred onto a transparent substrate, followed by Al deposition. PRL is then performed to pattern the Al layer to metal mesh structures. (b) An exemplary photo of graphene-transferred transparent PET substrate. (c) Microscope image of the PRL-patterned Al mesh on a graphene/PET substrate. Enlarged view (d) reveals cleanly defined Al mesh pattern. Optical transmittance plots (e) and (f) indicate the transmittances of bare graphene, bare metal mesh, and graphene-incorporated metal mesh samples for different mesh geometry and metal thickness described in the legends.

the Al deposition on the graphene-transferred substrate, PRL is conducted to define the metal mesh pattern on top of graphene, as demonstrated in **Figure 4.7c**. The enlarged view (**Figure 4.7d**) shows that the metal pattern is cleanly formed with few defects, which is widely attributed to the gentle nature and reliability of the PRL process.

In our G-TME fabrications, we used two combinations of graphene and metal mesh pattern: (1) multi-layer graphene + dense and thick metal mesh (50 μm cell size, 50 nm thick Al), and (2) single-layer graphene + coarse and thin metal meshes (150 and 750 μm cell size, 25 nm thick Al). To ensure better adhesion the mesh linewidths were designed to be 5 μm, except the 750 μm cell size mesh having 12 μm linewidth. **Figures 4.7e and 4.7f** compare the transmittances over the visible range for the bare graphene, bare metal mesh (TMEs), and graphene-mesh combined samples (G-TMEs), and the measured sheet resistances along with representative transmittances at 550 nm wavelength of all cases are summarized in **Table 4.2**. Comparing to bare graphene, the sheet resistance drastically decreased (i.e. 79-97 %) with much smaller decrease in transmittance (i.e. 2.9-18 %) after metal mesh patterning on graphene by PRL. Interestingly, the total combined resistance (R_{tot}) and transmittance (T_{tot}) of G-TMEs can be predicted from those of graphene (T_g, R_g) and metal mesh (T_m, R_m) based on the following equations:

$$R_{tot} = (R_g^{-1} + R_m^{-1})^{-1} = (R_g \times R_m)/(R_g + R_m) \quad (4\text{-}1)$$

$$T_{tot} = 1 - \left((1 - T_g) + (1 - T_m)\right) = T_g + T_m - 1 \quad (4\text{-}2)$$

where Equation (4-1) simply means that the metal mesh layer and the graphene layer are electrically connected in parallel, and Equation (4-2) assumes that transmittance is purely

determined by the absorption of each layer. Here the scattering effect is small and neglected. The calculated values are well-matched to the measurement data as indicated in **Table 4.2**, confirming that the metal mesh can be successfully patterned on the graphene film by PRL with few defects and negligible degradation of electrical property of either metal mesh or graphene.

Table 4.2 Measured sheet resistances of graphene, bare TMEs, and G-TMEs for different metal mesh geometry and thickness, and their comparison to calculated values.

Graphene type/ Mesh specification (Cell size [μm] / Al thickness [nm])		Graphene	Mesh (TMEs)	Graphene+Mesh (G-TMEs)
Multi-layer Graphene + Dense & thick mesh (50/50)	Sheet resistance [Ω/□] (decrease % from graphene)	469.8	14.3	14.0 (97 %)
	Calculated combined resistance [Ω/□] (Eq.(4-1))			13.8
	Transmittance at 550 nm wavelength [%] (decrease % from graphene)	95.2	84.1	78.0 (18 %)
	Calculated combined transmittance [%] (Eq. (4-2))			79.4
Single-layer Graphene + Coarse & thin mesh (150/25)	Sheet resistance [Ω/□] (decrease % from graphene)	1208	131.9	118.8 (90 %)
	Calculated combined resistance [Ω/□] (Eq.(4-1))			118.9
	Transmittance at 550 nm wavelength [%] (decrease % from graphene)	97.6	94.2	92.1 (5.6 %)
	Calculated combined transmittance [%] (Eq. (4-2))			91.8
Single-layer Graphene + Coarse & thin mesh (750/25)	Sheet resistance [Ω/□] (decrease % from graphene)	1208	287.7	248.8 (79 %)
	Calculated combined resistance [Ω/□] (Eq.(4-1))			232.4
	Transmittance at 550 nm wavelength [%] (decrease % from graphene)	97.6	97.4	94.8 (2.9 %)
	Calculated combined transmittance [%] (Eq. (4-2))			95.0

In our experimental scope of TME fabrication, for example for the 30 or 50 nm-thick Al-based TMEs having up to 50 μm cell sizes, the sheet resistance spans from 10 to 80 Ω/□ while the transmittance can reach up to ~ 90% (**Figures 4.6c and 4.6d**). This performance is comparable to the widely used commercial ITO-coated glass with typical sheet resistance of 20-80 Ω/□[62], and more importantly, can be readily obtained on both rigid and flexible substrates in a continuous and high-throughput manner. By combining graphene and thin metal mesh pattern with coarse geometry, which may be otherwise unsatisfactory if working separately, PRL can continuously fabricated the G-TMEs having much improved conductivity and high optical transmittance. Thus, PRL-manufactured TMEs and/or G-TMEs may potentially provide an excellent alternative to the ITO panels toward scalable and flexible electronics ranging from rollable touch screens to next-generation flexible displays and flexible solar cells.

4.3.4 Geometry-tunable pattern fabrication by PRL

Beyond the continuous and faster processability, PRL further realizes the real-time tuning of the pattern geometry, enabling the fabrication of diverse structures out of the single mask. Whereas the conventional lithography relies on the static and planar alignment between the mask and the substrate, the rolling principle in PRL allows the dynamic control of the mask rotating speed with respect to the feeding substrate during the UV exposure. In this case, the rollable mask and the feeding substrate are slightly separated to allow independent motions (i.e. proximity mode printing). Depending on the relative mask-substrate motions, the shape of resulting photolithography patterns can be modulated as more specfically described in **Figure 4.8a**; for example in line patterns, if

the mask rolling is faster than the substrate moving, the resulting line pattern becomes denser than the original mask pattern, and vice versa. Likewise for more complicated patterns, the final geometry can be readily tuned to achieve different aspect ratio using a single mask, as vividly exhibited in **Figures 4.8b and 4.8c**. Fast rotating of the roll mask compresses the original image in the substrate moving direction, while low speed rotation makes it elongated.

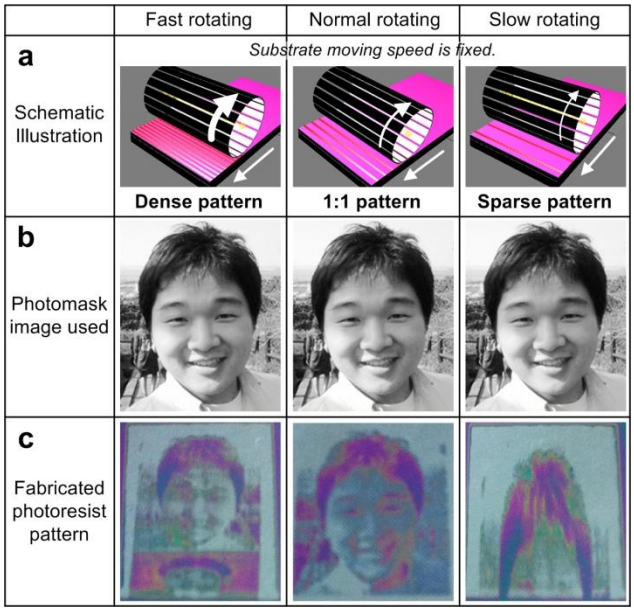

Figure 4.8 Demonstration of geometry-programmable PRL: (a) Conceptual schematics illustrating that the period of line patterns can be real-time controlled in PRL by modulating the mask rotation speed with respect to the substrate moving speed. Using an identical mask shown in (b), more complicated patterns can also processed to different shapes as displayed in (c) by such mask-substrate motion controls.

Since the UV exposure time may vary depending on the roller mask rotating speed in this geometry-tunable PRL process, the UV intensity can be regulated accordingly for consistent and reliable exposure. Namely, slow rotating speed leads to relatively long exposure time per one opening area on the photomask, which can broaden or even wipe out the photoresist pattern by over-exposure. Conversely, fast rotating speed

can cause under-exposure with a dose not enough to develop the photoresist pattern. To avoid these issues, the effective UV intensity (T') can be adjusted to maintain the constant level according to the following relationship:

$$T' = T \times (\omega r / v) \quad (4\text{-}3)$$

where T is the UV intensity calibrated for normal contact-mode PRL process (i.e. giving the 1:1 ratio pattern), and ω, r, and v are the rotating speed of a mask roll, its radius, and the substrate moving speed, respectively.

One unique advantage of this geometry-tunable PRL process is that a single photomask can produce a manifold of micro/nano-structures of varying dimensions. As an example, we demonstrate plasmonic IR filters having tunable polarizing bands based on the metal-insulator-metal (MIM) stack[69] (i.e. Al-SiO_2-Al in our design). Here PRL is applied to continuously pattern the top metal layer into sub-wavelength size dot array to induce surface plasmon polaritons (SPPs), similar to what has been previously investigated by utilizing R2R NIL[75]. While such NIL-based methods can also continuously create the large-area MIM pattern at high speed, it is impossible to tune the metal dot shapes in real-time in R2R NIL due to the precise mechanical imprinting characteristics. In comparison, PRL can modulate the dot pattern shapes simply by real-time controlling the mask-substrate motions with the same original mask, thereby tayloring the desired plasmonic performance.

Figure 4.9 displays the flexible IR filters fabricated on MIM-stacked PET substrates by the PRL process where the mask rotating speed was modulated under the fixed substrate feeding rate to make two different patterns (**Figures 4.9a and 4.9b**) using the identical photomask containing sub-wavelength scale dot pattern. The IR

transmittance spectra taken by a Fourier Transform Infrared (FT-IR) spectroscopy compared in **Figures 4.9c and 4.9d** indicate the difference of dip positions and polarization characteristics depending on the pattern geometry. Overall, two transmission dips emerge at the fundamental and second-order resonance wavelengths, demonstrating the IR filtering performance; in the case of round dot pattern (**Figure 4.9a**), these resonances are not significantly dependent on the polarization axis of incident IR light due to the symmetric dot shapes (**Figure 4.9c**)[75]. On the other hand, the asymmetric

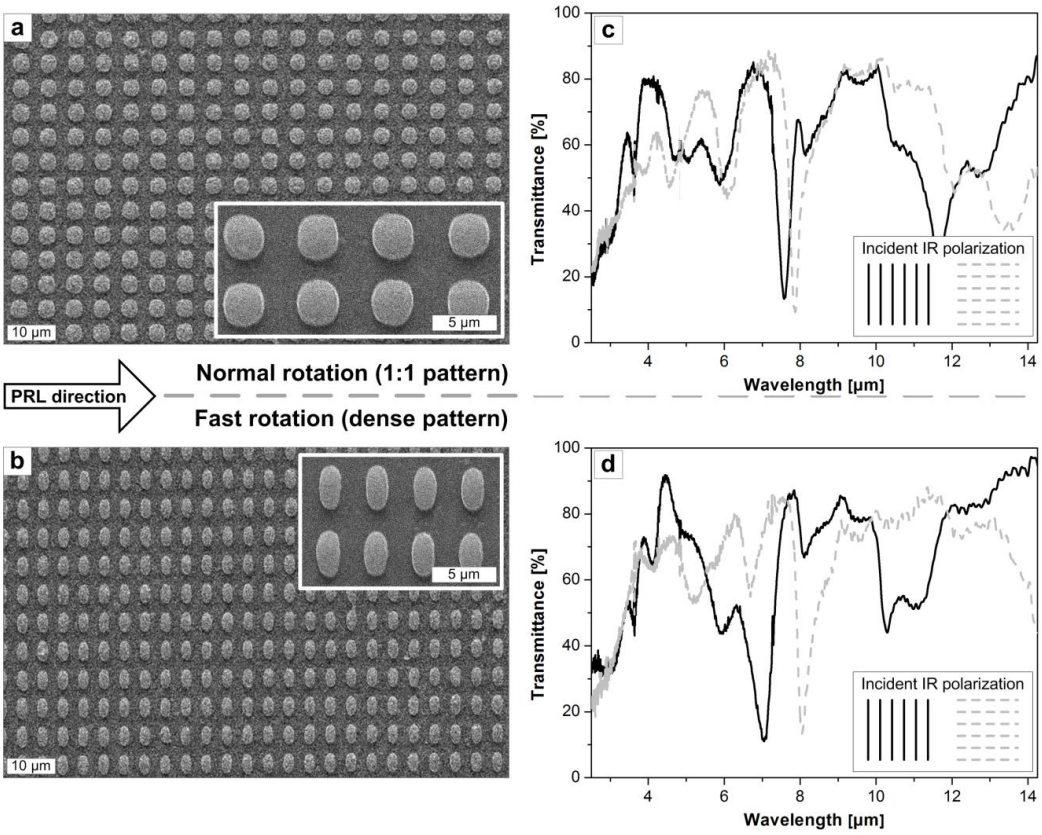

Figure 4.9 Single-mask fabrication of tunable plasmonic IR filters: SEM images of (a) round and (b) oval Al dot arrays patterned on MIM substrate by PRL using the same photomask at different mask rotating speeds. Insets to (a) and (b) clearly discloses that the shape and interspacing of the round dot array, obtained by moving the mask and substrate in 1:1 ratio, become smaller with faster rotation of the mask. The IR transmittance spectra taken from (c) round and (d) oval dot arrays demonstrate the tunability of dip positions and polarization characteristics in those two IR filters.

oval dot pattern slenderized by faster rotation of the rollable photomask during PRL (**Figure 4.9b**) reveals stronger polarization against the incident IR polarization axis while the resonances are blue-shifted because of the shrinked pattern size (**Figure 4.9d**). The result is currently at the preliminary stage, yet suggests a clear and prospective way to taylor the desired characteristics in many micro/nano-structured devices by utilizing the PRL process capable of real-time tunable patterning.

4.3.5 Summary

A new micro/nano-fabrication methodology termed as *PRL* – Photo Roll Photolithography – was developed to realize continuous and scalable photolithography by combining the advantages of photolithography and roll-processing. Not only can PRL faithfully perform the typical 1:1 photolithography but also can achieve the real-time geometry-tunable patterning by modulating the relative mask-substrate motions. A gentle processability further allows the use of delicate nanomaterials such as graphene as a substrate for PRL patterning. We have demonstrated the continuous fabrication of flexible TMEs and band-tunable IR filters by utilizing PRL to practical applications. Moving forward, PRL may extend its applicability to wider micro/nano-scale fabrications and devices that require high-throught and large-area processing and/or the use of flexible substrates.

Chapter 5

Concluding Remarks

5.1 Findings and contributions of this work

As a 'big' picture, this thesis has exploited three main themes: (1) hybrid nanoarchitectures comprising complementary nanostructures, (2) continuous and high-throughput nanomanufacturing processes, and, by capitalizing these novel methodologies as well as incorporating conventional techniques, (3) pragmatic and scalable micro/nano-engineered applications to energy conversion, optoelectronics, and photonics. Ranging from fundamental design, fabrication, and characterization, to theoretical analysis and diverse utilization, the major findings and contributions of this work include:

Functional hybrid nanoarchitectures comprising complementary nanostructures

- A development of **hybrid architectures of ZnO nanowires** (**ZNWs) grown on organized carbon nanotubes** (**CNTs)** through a two-step chemical vapor deposition based on the ZNW-CNT compatible Vapor-Solid growth mechanism;
- In-depth observations of structural and photoluminescence properties;
- An analytic model of nanocrystal growth;
- An emphasis on yield and scalability through mathematical estimation
- **Thin-film integration and further macroscopic scaling-up** by adopting the roll processing of CNT templates;

- A study of anisotropic electrical and photoconductive properties;
- An elucidation of general photoconduction mechanism of ZnO and its specifically rapid transport behavior upon CNT hybridization;
- **Versatile energy conversion applications**: rapid-responsive photodetectors and high-power photocurrent generators, with in-depth characterizations of photoelectric properties.

Continuous and scalable nanomanufacturing methodologies

- **Roll-to-Roll (R2R) nanomanufacturing**
  - A discussion on design criteria for successful R2R patterning;
  - An utilization of R2R process to continuous and scalable fabrication of flexible plasmonic metamaterials;
- **NanoChannel-guided Lithography (NCL)**
  - A development of NCL realizing continuous and seamless nanograting fabrication on liquid resists;
  - A comparative study: nanogratings fabricated on liquid-coated surfaces by NCL, achieving higher aspect ratio compared to ones formed on solids;
  - A study on interactive influence of resist wettability and substrate topography;
  - A study on temperature-controlled grating aspect ratios;
- **Vibrational Indentation-driven Patterning (VIP)**
  - A development of VIP achieving template-free fabrication of micro/nano-scale grating structures;
  - A study and demonstration of versatility of VIP, with an emphasis on real-time period and angle tunability, and extensive applicability to various substrate materials and multidimensional patterns;
  - An utilization of VIP process to IR polarizers;
- **Photo Roll Lithography (PRL)**
  - A development of PRL integrating photolithography and roll-processing for continuous and scalable micro/nano-fabrication;

- An application to transparent conducting electrodes, along with graphene incorporation for improved performance;
- A demonstration of geometry-tunable patterning and its application to band-tunable IR filters.

Pragmatic applications

- **Rapid-responsive photodetectors**;
- **High-photocurrent generators**;
- **Plasmonic IR filters**;
- **Plasmonic IR polarizers**;
- **Flexible transparent conductors**.

5.2 Outlook for upcoming works

(All the topics described in this section are not published yet, are therefore unable to reveal full details, but have already been embarked and are currently underway. Hence, referencing, reproducing, and mimicking of the contents described in this section without permission are prohibited.)

Extending the reach of this work by integrating further ideas and concepts, a series of highly prospective and additionally useful works may surely follow; several *ongoing* works include:

Hybrid architectures of vanadium oxide nanostructures grown on carbon nanotubes; As another functional hybrid architecture integrating complementary functionalities, vanadium oxide (VOx) directly grown on carbon nanotube templates can be potentially applicable to Li-ion electrochemical devices as an anode having large surface area and rapid charge transport characteristics along with high Li^+ intercalation capacity.

Density-controllable manufacturing of carbon nanotubes by nanoimprint Lithography

; By tailoring the areal coverage of catalyst films through nanoimprint lithography with different period and duty cycle, the areal density of resulting carbon nanotube forests can be tuned, thereby modulating the refractive indexes and possibly wettability.

One-step fabrication of all-polymer waveguides with smooth sidewalls

; Since a tilted cleaved mold make a 2-D contact to a substrate, NCL can produce seamless waveguide structures having ideally smooth sidewall regardless of the roughness existing on the original trench mold, thereby significantly reducing the propagation loss.

Appendices

Appendix A Experimental Details

A.1 Hybrid architectures of ZNWs grown on CNTs (Chapter 3)

A.1.1 CNT forest growth

Catalyst and support layers of Fe (1 nm) and Al_2O_3 (10 nm) were sequentially deposited by electron beam evaporation (SJ-26, Denton Vacuum, Inc.) onto a p-type (100) silicon wafer coated with 500 nm-thick thermally grown SiO_2. The catalyst substrate was loaded in a 1" quartz tube and placed in a single-zone atmospheric pressure tube furnace (Thermo-Fisher MiniMite), which is shown schematically in **Figure 2.2**. The sample was located 10 cm downstream of the control thermocouple of the furnace. After purging with 1000 sccm He (99.999% UHP, Metro Welding, Detroit, MI) at room temperature for 5 minutes, a flow of 400 sccm He and 100 sccm H_2 (99.999% UHP, Metro Welding) was maintained for 5 minutes to establish the catalyst annealing atmosphere before heating. Then, the furnace was heated to the growth temperature of 775 ℃ for 10 minutes, and maintained for 10 minutes to anneal the catalyst, and then 100 sccm C_2H_4 (99.9% UHP, Airgas, Inc., Randor, PA) was added for the growth duration of 20 minutes. After growth, the furnace was cooled to room temperature under a slight He flow.

A.1.2 ZnO NW growth on CNTs

ZnO NW (ZNW) growth was performed in the same tube furnace as CNT growth, and separate dedicated quartz tubes were used for CNT and ZNW growth. A piece of Zn foil (≈ 0.6 g, 99.98%, Alfa Aesar) was loaded at the center position (location of control thermocouple) the of the 1" quartz tube and the CNT samples (i.e. plain CNT forests, CNT bundles on TEM grids, horizontally aligned CNT sheets) were placed 6-7 cm downstream of the center. The furnace was initially pumped to approximately 10^{-2} Torr, then was heated at a ramp rate of 30 ℃ min^{-1} under a controlled amount of He flow which was kept throughout the process to facilitate vapor

transport. Then, a flow of air (zero grade, Airgas) was added after the furnace temperature surpassed the melting temperature of Zn (≈ 420 ℃); this initiates ZNW formation onto the target substrates [116]. The pressure was maintained constant throughout the process using a feedback control system with a motorized valve, which is configured by assembling a rotary pump (DUO 010M, Pfeiffer Vacuum), a compact Pirani pressure gauge (TPR 281, Pfeiffer Vacuum), a motorized valve (EVR 116, Pfeiffer Vacuum), and a feedback control unit (RVC 300, Pfeiffer Vacuum).

The structures shown in **Figures 2.4, 2.6-9** were grown at 17.5/20 sccm air/He, at 6 Torr pressure for 20 minutes, with 600 ℃ furnace setpoint temperature. The structure shown in **Figure 2.11** was grown using the identical conditions except the growth time of 5 minutes. According to temperature profiles (**Figure 2.3**) measured along the central axis of the furnace tube, the temperature was 614 ℃ at the center location and 591 ℃ at the sample position.

A.1.3 Structural and optical characterization

SEM imaging along with EDX analysis was performed using a Philips XL30-FEG, operating at 10 kV, with the stage typically tilted at 45°. GI-XRD analysis was conducted under thin film grazing incidence mode at GI angle of 0.5° with Cu K (alpha) laser radiation (Rigaku Ultima IV). To prepare samples for TEM characterization, as-grown CNTs were sonicated in toluene without any surfactant for 1 hour and several drops of this dispersion were applied to a copper mesh TEM grid. After drying in flowing N_2, some of the thin CNT bundles and/or individual CNT filaments remained suspended. ZNWs were then grown on the CNTs by placing the grid inside the furnace at the same position as the flat substrates. A JEOL 3011 TEM instrument operating at 300 keV was used for conventional TEM (CTEM) imaging. A JEOL-2010F analytical electron microscope (AEM) supporting both CTEM and STEM modes was used at the operation voltage of 200 keV to characterize the ZnO-CNT interface and its elemental composition through high-angle annular dark-field (HAADF) imaging and EELS. The lens conditions were set to define a probe size of 0.2 nm for HAADF imaging and EELS analysis. A 0.5 eV/pixel dispersion was used that gave an energy resolution of about 1.5 eV (full-width at half maximum, FWHM). X-ray diffraction was performed on a Rigaku Ultima IV in thin film grazing incidence (GI) mode at an angle of 0.5°.

In preparation for PL measurements, ZNWs were first grown on a 1 × 1 cm CNT forest substrate, and then the ZNW/CNT sample was carefully delaminated from the substrate using a cleaned razor blade. The ZNW/CNT forest was mounted on a quartz plate using a double-sided tape (3M). An as-grown CNT sample with the same size was processed identically as a reference.

The PL spectra were acquired using a fluorescence spectrophotometer (QM-4, PTI) with an excitation beam wavelength of 325 nm.

A.1.4 Device fabrication

First, vertically aligned CNT "blades" were grown from lithographically patterned catalyst. To pattern the catalyst, a SiO_2/Si wafer was coated with ≈ 3 μm-thick photoresist (SPR220) by spin-coating at 3000 rpm for 30 seconds and pre-baking at 115 ℃ for 90 seconds. The sample was exposed to UV light for 6 seconds on a Karl Suss MA-6 Mask Aligner in order to lithographically define the shape and position of the catalysts. The sample was then post-baked at 115℃ for 90 seconds, and then immersed in MIF 300 developer for 1 minute. Next, Fe and Al_2O_3 were deposited by e-beam evaporation on the sample. Lift-off was performed by sonicating the sample in acetone for 5-10 minutes, then washing in isopropyl alcohol and deionized water. After CNT growth, the CNT blades were transformed to horizontally aligned (HA-CNT) sheets by mechanical rolling followed by elastocapillary densification as discussed in our separate publication[139]. Electrodes were then deposited on by e-beam evaporation of Au (800 nm thickness) through shadow masks that were laser-cut in polyester film. Finally, ZNWs were grown directly on the CNT sheet device having Au electrodes by the aforementioned procedure.

A.1.5 Device characterization

The electrical and photoelectric properties of ZNW/CNT devices were characterized via a 4-point *I-V* measurement using a custom-built probe station. UV irradiation was applied using a UV lamp (Dymax, Model 2000 Flood, 365 nm, 75 mW-cm^{-2}). The UV intensity was modulated by changing the distance between the source and the device. For the measurements in vacuum environment, a vacuum probe station equipped with an ultra-high vacuum system (Varian, TPS-Compact) and an optical window was used, and the experiments were carried out at the pressure lower than 2.5×10^{-6} Torr. All UV exposure experiments were conducted in a dark room to exclude any external light disturbance to the measurements.

A.2 NanoChannel-guided Lithography (NCL) (Chapter 4.4)

A.2.1 Preparations of molds and substrates

The grating molds were fabricated by nanoimprint lithography on a thermally grown SiO_2 layer on Si substrate, and the fabrication details can be found in our previous works[64]. For the

NCL process, only a thin slice of well-cleaved SiO_2/Si grating mold is needed since the patterning process is essentially based on a line contact with the liquid resist on the polymer substrate. The cleaving direction of the mold is perpendicular to the grating pattern for optimal nanochannel formation upon cleaving. Thus, extra care has been taken during the mold fabrication to align the mold grating direction to the crystal planes of Si. The fabricated mold is then cut to a rectangular shape for the ease of handling and subsequent cleaving. To form a sharp and completely flat mold edge, a small notch is first made at one of the edges parallel to grating direction by a diamond scriber (McMaster-Carr), and is then snapped. Additional cleaning is applied to remove the debris generated at cleaving, if necessary. The molds used in this study have two different grating periods: 700 and 200 nm, as shown in **Figures 3.5b and 3.5c**, respectively. To prepare the substrates, a sheet of perfluoroalkoxy (PFA) or polyethylene terephthalate (PET) is first cleaned by acetone and isopropyl alcohol (IPA) followed by nitrogen drying, and then is treated by O_2 plasma (17 sccm, 80 W, 30 s) to remove residual moisture and increase the surface energy by forming –OH surface groups for the ease of resist coating. Fluorine treatment on the PET surface is performed by vapor deposition of a fluorinated surfactant, (tridecafluoro-1,1,2,2-tetrahydrooctyl)trichlorosilane (GELEST, Inc.), for 15 minutes at 90 ℃. To coat the substrates with UV-curable liquid resist, an epoxy-based SSQ ($T^{Phenyl}_{0.4}Q_{0.1}T^{Epoxy}_{0.5}$)[180] mixed with 3 wt% photoacid generator (UV-9820, Dow Corning Corp.) is diluted with propylene glycol monomethyl ether acetate (PGMEA) to make a SSQ resist solution containing 10-20 wt% SSQ. In this study the SSQ solution is spin-casted onto the substrate sheet at 500-1000 rpm. PGMEA is then completely dried to leave a thin layer of SSQ with the thickness of 400 nm – 2 μm. Spin-casting process can be replaced by a continuous coating method in the future, such as die or micro-gravure coating.

A.2.2 NCL processing

A well-cleaved grating mold is mounted to the heater-attached holder which is inclined typically at an angle of 15° with respect to the substrate plane. A substrate is placed on a silicone rubber film attached to a tilting stage. By adjusting the 5-DOF tilting stage (Newport Corp.), the mold edge and the substrate surface are positioned to be parallel along the contact line. The conductive heater attached to the backside of the mold is then turned on to control the process temperature, maintained by the feedback controller (Yokogawa Corp.) throughout the process. Once the temperature is in equilibrium, the edge of a mold makes contact with a substrate under a slight mechanical force (~5 N, monitored by a flexible force sensor (Tekscan Inc.)). Then, the substrate is transferred at a controlled speed (~0.5-2 cm s^{-1}) under a conformal contact with the

mold edge, to create NCL nanograting. A UV light source (7.2 W cm^{-2}, EXFO Inc.) mounted in front of the mold at 10 cm distance promptly cures the liquid resist extruding from the end of the nanochannels on the mold within 10 s, to complete the fabrication of nanograting structures with well-retained profile.

A.2.3 Characterizations

SEM imaging was performed using a Philips XL30-FEG, operating at 20-30 kV, after sputtering a thin Au film (~2-3 nm) to avoid electron charging. To prepare the cross sections, because of the difficulty to cleanly cleave the grating samples fabricated on flexible polymers (e.g. PFA or PET), they were stamped to cleaned Si substrates using epoxysilicone[179] as a resist, followed by UV curing and cleaving. To ensure good adhesion between epoxysilicone and Si surfaces during demolding, the Si substrates cleaned with acetone and IPA and dried by nitrogen blow were pretreated with O_2 plasma (17 sccm, 150 W, 120 s) and then treated with epoxy-adhesion promoters (Silquest A-187, Momentive Performance Materials). Thus, all cross-sectional views in the article reveal the counterprofiles of the patterned resist gratings. The viscosity and shear stress of liquid SSQ were measured using an ARES Rheometer (TA Instruments), monitored and recorded by TA Orchestrator. To determine both the viscosity and shear stress at different shear rates of the liquid SSQ material, a shear rate sweep was performed at room temperature by increasing the shear rate of a pair of stainless steel disk plates (1" diameter, 0.4 mm gap) uniformly filled with liquid SSQ. Viscosity as a function of temperature was then measured by sweeping the temperature at the fixed shear rate of 1 rad/s under identical configurations. The static contact angles of liquid SSQ were measured by a home-made contact angle analyzer with real-time imaging by gently placing an SSQ droplet (~6 µl) on the targeted surface. The presented values were averaged over at least three measurements in each case.

A.3 Vibrational Indentation-driven Patterning (VIP) (Chapter 4.5)

A.3.1 VIP processing

A high-speed DC motor (up to 24000 rpm) with an eccentric mass (~10 g) is fixed to an aluminum tool holder. The motor is connected to an adjustable resistance circuit to allow real-time speed control. A well-cleaved Si piece is mounted to this motor-assembled tool holder which is inclined typically at an angle of 15-45° with respect to the substrate plane. This tool assembly unit was designed to be as light as possible to maximize the vibration amplitude and also to avoid

resonance. A substrate is placed on a thin polydimethylsiloxane (PDMS; Sylgard 184, Dow Corning Corp.) pad attached to a homemade 5-DOF stage (components from Newport Corp.). The PDMS pad provides the attached substrate surface with an ideal flatness by conformal contact to maintain the uniform distance from the vibrating tool edge, thereby ensuring stable and consistent periodic indentations throughout the process. By adjusting the 5-DOF stage, the tool edge and the substrate surface are positioned to be parallel with a small gap controlled to be within the oscillation amplitude of the tool edge. With the motor turned on, the substrate is transferred by a motorized linear motor (CMA-12CC, Newport Corp.) at a controlled speed (~25-250 μm s^{-1}), to create grating patterns on a substrate by periodical vertical indentations of a tool edge.

A.3.2 Substrate preparations

All polymer substrates (PET; Melinex 454, Tekra Corp., PC; Lexan 8010, Tekra Corp., and polyimide; Kapton HN, DuPont) are used as purchased or after IPA cleaning followed by nitrogen drying. Electron beam evaporation (Enerjet Evaporator, Denton Vacuum, Inc.) was performed in case for the deposition of metals (e.g. Au, Al). For the coating of PEDOT, the as-purchased PEDOT (Clevios PH 500, Heraeus Holding) was spin-casted on a cleaned PET substrate (2000 rpm, 30 s) and then baked (110 ℃, 15 min) to remove residual solvent.

A.3.3 Characterizations

SEM (Philips XL30-FEG) imaging was carried out typically at the operating voltage of 10-25 kV, after sputtering a thin Au film (~3-5 nm) to avoid electron charging, if needed. A Veeco Dimension Icon AFM was used for the AFM profiling under the soft-tapping mode (sweeping rate of 2 Hz, 1024 lines per sample). The FT-IR measurement was performed using a Spectrum GX FT-IR spectroscopy (Perkin-Elmer) with the incident IR wavenumbers swept from 1100 cm^{-1} to 800 cm^{-1}) through a high-quality IR polarizer (KRS-5, Perkin-Elmer).

A.4 Scalable hybrid ZnO/CNT thin films (Chapter 5.2)

A.4.1 Fabrication of ZnO/CNT hybrid thin film devices

The CNT “blade” line pattern photomask was designed as the 20 μm linewidth and 1.5 cm length with the 200 μm spacing between each line typically in 1.5 × 1.5 cm area. By the photolithography using this mask, catalyst and support layers of Fe (1 nm) and Al_2O_3 (10 nm)

were patterned on a 250 nm-thick SiO_2 grown Si wafer. The CNT blades were grown on this catalyst pattern by the atmospheric CVD process[78] in a single-zone tube furnace (Thermo-Fisher MiniMite) at the setpoint temperature of 775 ℃ for 5 minutes under a mixed flow of 100 sccm He, 400 sccm H_2 (99.999% UHP, Metro Welding), and 100 sccm C_2H_4 (99.9% UHP, Airgas, Inc.). This results in the VA-CNT blades having ~ 220 μm height in average to allow sufficient overlapping when horizontally rolled down (**Figures 4.1a and 4.1c**). The grown CNT blades were then transformed to HA-CNT sheets by mechanical rolling followed by elastocapillary densification[139], resulting in ~ 1.5 μm thick HA-CNTs. 800 nm-thick Au electrodes were symmetrically deposited on both ends of HA-CNT sheet by using a shadow mask laser-cut in polyester film. Then, ZNWs were directly grown on the HA-CNT sheet device having Au electrodes (**Figures 4.1b and 4.1d**) by the low-pressure CVD under 17.5/20 sccm air/He mixture flowing at 6 Torr pressure with 600 ℃ setpoint temperature using a piece of Zn foil (≈ 0.6 g, 99.98%, Alfa Aesar) as a source. The typical diameter and length of the resulting ZNWs were approximately 25-50 nm and 300-500 nm, respectively. For asymmetric device preparation, an additional 800 nm-thick Au electrode was deposited in the middle 'after' ZNW growth process (see **Figure 4.5a**). Detailed procedure for photolithography and deposition and full description of CNT and ZNW growth processes can also be found in our previous paper[228].

A.4.2 Microscopy characterizations

A Philips XL30-FEG SEM operating typically at 10 kV was used for SEM imaging. TEM imaging was performed using a JEOL 3011 TEM instrument operating at 300 keV. To prepare the sample for TEM characterization, as-grown CNTs were sonicated in toluene without any surfactant for 1 hour and several drops of this dispersion were applied to a copper mesh TEM grid. After dried, the CNT-suspended copper grid was then loaded into ZNW growth process. In about 1 minute after Zn started vaporizing, the growth process was abruptly stopped by ample He purging and cooling, to freeze the ZnO growth at the initial nucleation step.

A.4.3 Electrical and photoelectrical characterizations

The measurements of electrical and photoelectric properties of ZnO/CNT devices were conducted using a custom-built 4-point probe station. UV illumination was supplied using a UV lamp (Dymax, Model 2000 Flood; 365 nm wavelength, 75 mW/cm^2 at the housing outlet). By adjusting the distance between the UV source and the device, the UV intensity was varied and measured by the power meter. For measuring (photo)conductivity (**Figure 4.2**), the DC voltage was swept under continuous UV illumination with the current recording. For characterizing the

photocurrent generation and photoresponse dynamics (**Figures 4.3-5**), a pulsed UV light was illuminated with or without the constant DC bias applied between the electrodes while the current and time were recorded. All UV-photoelectric experiments were carried out in a dark room to minimize external light disturbance.

A.5 Photo Roll Lithography (PRL) (Chapter 5.3)

A.5.1 Setup and operation of the PRL system

Overall, the PRL system consists of a photomask-attached rollable UV exposure unit, a linear-motorized substrate feeding system, and the develop module. First, a collimated UV source core is prepared by housing the 1 mm-wide slit over the UV lamp (CS 2010, Thorlabs, Inc.). This UV core is suspended inside a 90 mm-diameter hollow quartz cylinder with the slit facing downward, supported by ball bearings at both ends of a cylinder so as to allow the cylinder rotation with a static UV core inside. A thin layer of PDMS (Sylgard 184, Dow Corning Corp.) is wrapped around the outer cylinder surface, and then a flexible photomask (see below for fabrication details) is conformally attached onto the PDMS pad. This rollable UV exposure unit is then arranged over a 3-DOF stage motorized by a linear piezo motor (CMA-12CC, Newport Corp.). The substrates are prepared and coated with photoresist for desired fabrications (e.g. TMEs, graphene, and IR filters) as described in detail in the following section. The photoresist-coated substrate sample is then located on a motorized linear stage and is brought into contact (for TME fabrication) or proximity (for geometry-controlled patterning including IR filter fabrication) by controlling the stage axes in the way that the contact line between the substrate surface and the rolled mask is aligned to the UV exposing slit inside. As the mask rolling and substrate feeding proceed either isokinetically (in contact mode) or by independent controlling (in proximity) with the UV light on, a continuous UV exposure is conducted onto the sample through the photomask pattern. With the peak UV wavelength fixed at 365 nm, the intensity was regulated in the range of 40-200 mJ/cm^2 depending on the pattern dimensions and processing speeds, to ensure consistent UV exposure. Finally, the sample passes through the developer bath (MF-319, Shipley) for about 1 minute, finalized by the following metal etching which can be done in case of Al used in this study by additional 1-2 minute immersion in the developer.

A.5.2 Fabrication of a flexible photomask

First, original pattern masks were prepared on either a 5” Cr/glass mask plate by using a

mask maker (for TME and IR filter patterns) or on a PET film by directly laser-printing the black-and-white image (shown in **Figure 4.8**). Using this original mask, a flexible photomask is fabricated through the conventional photolithography process. A 50 nm-thick Al was first deposited on a PET film by using e-beam evaporator (Enerjet Evaporator, Denton Vacuum, Inc.), followed by the spin-coating of a photoresist layer (S1815, Shipley) at 3000 rpm for 30 s. After soft-baking at 95 ℃ for 1 minute, UV exposure is carried out through the prepared hard mask plate containing desired patterns in a Karl Suss MA6 aligner for larger feature sizes (> 1.5 μm) or a stepper (GCA AS200 AutoStep) for small features (~ 500 nm). The sample with UV-exposed mask pattern is then developed in MIF-319 developer, accompanied by the additional 1-2 minute immersion to etch the exposed Al layer as well. The residual photoresist layer was removed by acetone and cleaned by isopropyl alcohol (IPA) to complete the fabrication of a flexible Al/PET photomask.

A.5.3 Preparation of substrates

For the Al mesh TME samples, the substrates are prepared by depositing 20, 30, or 50 nm-thick Al layer on bare or graphene-transferred glass pieces or PET sheets (Melinex 454, Tekra Corp.) via e-beam evaporation (Enerjet Evaporator, Denton Vacuum, Inc.). See the next section for detailed graphene transfer procedure. For IR filter samples, an MIM stack of Al (100 nm)-SiO_2 (200 nm)-Al (200 nm) are sequentially sputtered on a PET sheet by using a Lab 18-2 sputter tool (Kurt J. Lesker). A thin layer of photoresist (Microposit S1805, Shipley) is spin-coated on these substrates, typically at 4000 rpm for 30 s followed by a 1 minute baking at 95 ℃.

A.5.4 Transfer of graphene onto the target substrates

In order to transfer graphene from Cu to our target substrates, we use a technique similar to one described previously [256, 257]. A graphene film grown on a Cu foil (Gratom M, Bluestone Global Tech.) is first spin-cast with a thin layer of poly(methyl methacrylate) (PMMA, 950 A9, MicroChem Corp.) at 1750 rpm for 45 s, and is naturally dried in the ambient environment. Then, the PMMA-coated graphene/Cu piece is floated on a $FeCl_3$ solution (Dalpro E-1G) to etch the Cu foil. Once all Cu has been etched away (~1.5 hours) the PMMA-coated graphene is scooped from the etchant bath with a clean glass cover-slip, followed by ample DI water rinsing, and is floated in a DI water bath. The target transparent substrates pretreated by O_2 plasma (55 sccm O_2, 160 mTorr, 150 W, 30 sec; Glen 1000-P Asher) are used to scoop the PMMA/graphene stack from the DI bath. After completely drying in moderate (~100 Torr) vacuum overnight, the PMMA layer is carefully removed through ample washing in acetone, IPA, and DI water, leaving only the

graphene layer on the target substrate.

A.5.5 Characterizations

SEM imaging was performed using a Philips XL30-FEG SEM, typically at the operating voltage of 10-25 kV after sputtering a thin Au film (<5 nm) to avoid electron charging if necessary. The sheet resistances of fabricated TMEs were measured using a multi-meter (GDT-311, Gardner Bender) after 100 nm-thick Al electrodes were additionally deposited at both ends of the TME sample after separating from non-patterned surrounding area. For each sample, the distance between electrodes was varied to three different values to obtain the exact sheet resistance by extracting contact resistances originating between multi-meter tips and sample electrodes. The optical transmittance measurements of TMEs were conducted using a Nikon Eclipse TE300 microscope with a HR4000CG spectrometer (Ocean Optics Inc.). The IR transmittance spectra of IR filter samples were measured by the FT-IR spectroscopy (Spectrum GX, Perkin-Elmer) with the incident IR wavenumbers swept from 4000 cm^{-1} to 400 cm^{-1}) through a high-quality IR polarizer (KRS-5, Perkin-Elmer).

Appendix B A First-order Model of Nanowire Nucleation and Growth on Carbon Nanotubes by the Vapor-Solid Mechanism

We first define the supersaturation,

$$\alpha = \frac{P}{P_o} \tag{1}$$

where P is the pressure of precursor vapor (source) and P_o is the vapor pressure of precursor that is in equilibrium with a solid surface (substrate).

Because a nanoscale structure has a small radius of curvature, the vapor pressure at its solid surface is higher than a bulk (infinite radius of curvature) surface. This is approximated by the Gibbs-Thomson equation[134] (using P_o above as the vapor pressure above the nanostructured surface).

$$\frac{P_o}{P_\infty} = \exp\left(\frac{2\sigma v \sin\theta}{kTR}\right) \tag{2}$$

P_∞ : vapor pressure above the bulk surface (obtained from standard tables)
σ : surface energy of exposed surface
v : molecular volume (or atomic volume) of the crystal
k : Boltzmann's constant
T : crystal temperature
R : crystal radius
θ : contact angle between crystal and substrate

Next we adopt a general model of nucleation of a nanocrystal on a substrate[134]. The total free energy change due to formation of the crystal, from the gas phase to the solid phase is,

$$\Delta G = \Delta G_{surface} + \Delta G_{bulk} \tag{3}$$

where $\Delta G_{surface}$ and ΔG_{bulk} are changes in the free energy in surface and volume, respectively.

Taking N as the number of molecules in the nanocrystal (ZnO), and assuming the atoms that form a crystal cluster as an ideal vapor, each term of (3) can be rewritten as,

$$\begin{aligned} \Delta G_{surface} &= \sum\nolimits_i S_i \gamma_i \\ \Delta G_{bulk} &= N\Delta\mu = N(\mu_{liquid} - \mu_{vapor}) = -NkT\ln\alpha \end{aligned} \tag{4}$$

where S is the surface area, γ is a surface energy, and μ is a chemical potential per atom (or molecule).

Assuming the cluster as a hemisphere having radius R (**Figure 2.12a**),

$$Nv = \frac{2}{3}\pi R^3 \tag{5}$$

Taking σ_1 as the cluster surface energy, and σ_{12} as the crystal-substrate interface energy (**Figure 2.12a**), then from (4) and (5) we obtain,

$$\begin{aligned} \Delta G_{surface} &= 2\pi R^2 \sigma_1 + \pi R^2 \sigma_{12} = \pi R^2 (2\sigma_1 + \sigma_{12}) \\ \Delta G_{bulk} &= -\frac{2\pi R^3}{3v} kT \ln \alpha \end{aligned} \tag{6}$$

Substituting (6) and (2) (where we take $\sigma = \sigma_1$ and $\theta = 90°$) to (3), we obtain,

$$\Delta G = \pi \left(3.3\sigma_1 + \sigma_{12}\right) R^2 - \frac{2\pi kT}{3v} \ln\left(\frac{P}{P_\infty}\right) R^3 \tag{7}$$

In order for the cluster to continue growing, ΔG must decrease as R increases. Namely, the cluster continues growing when it reaches a critical size R^*; at $R < R^*$, ΔG increases, and at $R > R^*$, ΔG decreases. Hence, we can find the value of R^* by taking the first derivative of ΔG with respect to R,

$$\left.\frac{d\Delta G}{dR}\right|_{R^*} = 0 \tag{8}$$

Thus by taking the first derivative of (7), we finally get,

$$R^* = \frac{(3.3\sigma_1 + \sigma_{12})v}{kT \ln(P / P_\infty)} \tag{9}$$

As discussed in the main text, we now consider two limiting cases: (I) Zn vapor adsorbs to form Zn clusters which are later oxidized, and therefore P_∞ is the vapor pressure of Zn at the substrate temperature; and (II) Zn vapor forms ZnO clusters immediately, and therefore P_∞ is the vapor pressure of Zn above ZnO at the substrate temperature. It is noted that the vapor species over the ZNW growth substrate is mostly Zn while the pressure of ZnO vapor is negligible[258]. Therefore, we can consider that Zn is the dominant precursor species over the substrate surface. **Table A.1** lists the parameter values of each case[135-138] for our growth conditions (i.e. at 600 ℃ furnace setpoint temperature).

Table A.1 Parameters for the two limiting cases: (I) Zn vapor first forms Zn clusters which are later oxidized to ZnO, and (II) Zn vapor directly forms ZnO clusters.

At source (614 ℃)	At substrate (591 ℃)			
Vapor Pressure [Torr]	Case	Vapor Pressure [Torr]	Surface Energy [J/m^2]	Atomic Volume [nm^3] [e]
14.6 [a]	(I) Zn	9.51 [a]	0.742 [c]	1.01×10^7
	(II) ZnO	2.37×10^{-9} [b]	0.353 [d]	2.41×10^7

[a] Ref[136]. [b] Ref[138]. [c] Ref[135]. [d] Ref[137]. [e] The atomic volumes are calculated by dividing molar volumes of Zn (9.2 cm^3/mol) and ZnO (14.5 cm^3/mol) by Avogadro's number.

Substituting parameters given in Table S1 to (9), we get $R^* \approx 11.8$ nm and 0.17 nm for case (I) and (II), respectively.

To predict how the critical cluster size changes with temperature, we plot ΔG versus R using (7) for both cases, at different temperatures (**Figures 2.13b and 2.13c**). At each temperature, the surface energy, vapor pressure, and supersaturation are also affected. As T increases, ΔG decreases.

A decrease in ΔG at higher T would make it easier to continue nucleating new clusters resulting in film growth, rather than to demand newly accommodated atoms seek for energetically favorable direction from existing clusters. **Figure 2.13** advocates this analytical interpretation by showing that the film growth becomes dominant while fewer NWs grow as the temperature (both of the source and the substrate) increases.

Bibliography

[1] L. J. Guo, "Recent progress in nanoimprint technology and its applications," *Journal of Physics D-Applied Physics,* vol. 37, pp. R123-R141, Jun 2004.

[2] D. R. Rolison, R. W. Long, J. C. Lytle, A. E. Fischer, C. P. Rhodes, T. M. McEvoy, *et al.*, "Multifunctional 3D nanoarchitectures for energy storage and conversion," *Chemical Society Reviews,* vol. 38, pp. 226-252, 2009.

[3] Z. L. Wang, "The new field of nanopiezotronics," *Materials Today,* vol. 10, pp. 20-28, May 2007.

[4] Z. L. Wang, "Piezopotential gated nanowire devices: Piezotronics and piezo-phototronics," *Nano Today,* vol. 5, pp. 540-552, 2010.

[5] M. S. Dresselhaus, G. Dresselhaus, and P. Avouris, *Carbon Nanotubes: Synthesis, Structure, Properties and Applications*: Springer, 2001.

[6] H. J. Fan, P. Werner, and M. Zacharias, "Semiconductor nanowires: From self-organization to patterned growth," *Small,* vol. 2, pp. 700-717, Jun 2006.

[7] S. Park and R. S. Ruoff, "Chemical methods for the production of graphenes," *Nature Nanotechnology,* vol. 4, pp. 217-224, Apr 2009.

[8] M. J. Madou, *Fundamentals of Microfabrication and Nanotechnology, Third Edition, Three-Volume Set: The Science of Miniaturization, Second Edition*, 3 ed.: Taylor and Francis, 2009.

[9] L. J. Guo, "Nanoimprint lithography: Methods and material requirements," *Advanced Materials,* vol. 19, pp. 495-513, Feb 2007.

[10] S. Iijima, "HELICAL MICROTUBULES OF GRAPHITIC CARBON," *Nature,* vol. 354, pp. 56-58, Nov 1991.

[11] F. Kreupl, A. P. Graham, M. Liebau, G. S. Duesberg, R. Seidel, E. Unger, *et al.*, "Carbon nanotubes for interconnect applications," *Ieee International Electron Devices Meeting 2004, Technical Digest,* pp. 683-686, 2004.

[12] P. R. Bandaru, "Electrical properties and applications of carbon nanotube structures," *Journal of Nanoscience and Nanotechnology,* vol. 7, pp. 1239-1267, Apr-May 2007.

[13] M. S. Dresselhaus, G. Dresselhaus, and R. Saito, "PHYSICS OF CARBON NANOTUBES," *Carbon,* vol. 33, pp. 883-891, 1995.

[14] T. W. Ebbesen, H. J. Lezec, H. Hiura, J. W. Bennett, H. F. Ghaemi, and T. Thio, "Electrical conductivity of individual carbon nanotubes," *Nature,* vol. 382, pp. 54-56, Jul 1996.

[15] A. Javey, J. Guo, Q. Wang, M. Lundstrom, and H. J. Dai, "Ballistic carbon nanotube

field-effect transistors," *Nature,* vol. 424, pp. 654-657, Aug 2003.

[16] H. J. Li, W. G. Lu, J. J. Li, X. D. Bai, and C. Z. Gu, "Multichannel ballistic transport in multiwall carbon nanotubes," *Physical Review Letters,* vol. 95, Aug 2005.

[17] B. Q. Wei, R. Vajtai, and P. M. Ajayan, "Reliability and current carrying capacity of carbon nanotubes," *Applied Physics Letters,* vol. 79, pp. 1172-1174, Aug 2001.

[18] M. F. Yu, O. Lourie, M. J. Dyer, K. Moloni, T. F. Kelly, and R. S. Ruoff, "Strength and breaking mechanism of multiwalled carbon nanotubes under tensile load," *Science,* vol. 287, pp. 637-640, Jan 2000.

[19] P. Kim, L. Shi, A. Majumdar, and P. L. McEuen, "Thermal transport measurements of individual multiwalled nanotubes," *Physical Review Letters,* vol. 87, Nov 2001.

[20] D. Tasis, N. Tagmatarchis, A. Bianco, and M. Prato, "Chemistry of carbon nanotubes," *Chemical Reviews,* vol. 106, pp. 1105-1136, Mar 2006.

[21] R. Martel, T. Schmidt, H. R. Shea, T. Hertel, and P. Avouris, "Single- and multi-wall carbon nanotube field-effect transistors," *Applied Physics Letters,* vol. 73, pp. 2447-2449, Oct 1998.

[22] K. Keren, R. S. Berman, E. Buchstab, U. Sivan, and E. Braun, "DNA-templated carbon nanotube field-effect transistor," *Science,* vol. 302, pp. 1380-1382, Nov 2003.

[23] C. M. Niu, E. K. Sichel, R. Hoch, D. Moy, and H. Tennent, "High power electrochemical capacitors based on carbon nanotube electrodes," *Applied Physics Letters,* vol. 70, pp. 1480-1482, Mar 1997.

[24] R. Z. Ma, J. Liang, B. Q. Wei, B. Zhang, C. L. Xu, and D. H. Wu, "Study of electrochemical capacitors utilizing carbon nanotube electrodes," *Journal of Power Sources,* vol. 84, pp. 126-129, Nov 1999.

[25] D. N. Futaba, K. Hata, T. Yamada, T. Hiraoka, Y. Hayamizu, Y. Kakudate, *et al.*, "Shape-engineerable and highly densely packed single-walled carbon nanotubes and their application as super-capacitor electrodes," *Nature Materials,* vol. 5, pp. 987-994, Dec 2006.

[26] E. Frackowiak, K. Metenier, V. Bertagna, and F. Beguin, "Supercapacitor electrodes from multiwalled carbon nanotubes," *Applied Physics Letters,* vol. 77, pp. 2421-2423, Oct 2000.

[27] Z. C. Wu, Z. H. Chen, X. Du, J. M. Logan, J. Sippel, M. Nikolou, *et al.*, "Transparent, conductive carbon nanotube films," *Science,* vol. 305, pp. 1273-1276, Aug 2004.

[28] D. S. Hecht, L. B. Hu, and G. Irvin, "Emerging Transparent Electrodes Based on Thin Films of Carbon Nanotubes, Graphene, and Metallic Nanostructures," *Advanced Materials,* vol. 23, pp. 1482-1513, Apr 2011.

[29] E. T. Thostenson, Z. F. Ren, and T. W. Chou, "Advances in the science and technology of carbon nanotubes and their composites: a review," *Composites Science and Technology,* vol. 61, pp. 1899-1912, 2001.

[30] M. J. Biercuk, M. C. Llaguno, M. Radosavljevic, J. K. Hyun, A. T. Johnson, and J. E. Fischer, "Carbon nanotube composites for thermal management," *Applied Physics Letters,* vol. 80, pp. 2767-2769, Apr 2002.

[31] J. N. Coleman, U. Khan, W. J. Blau, and Y. K. Gun'ko, "Small but strong: A review of

the mechanical properties of carbon nanotube-polymer composites," *Carbon,* vol. 44, pp. 1624-1652, Aug 2006.

[32] E. S. Snow, F. K. Perkins, E. J. Houser, S. C. Badescu, and T. L. Reinecke, "Chemical detection with a single-walled carbon nanotube capacitor," *Science,* vol. 307, pp. 1942-1945, Mar 2005.

[33] C. Li, E. T. Thostenson, and T. W. Chou, "Sensors and actuators based on carbon nanotubes and their composites: A review," *Composites Science and Technology,* vol. 68, pp. 1227-1249, May 2008.

[34] Q. Cao and J. A. Rogers, "Ultrathin Films of Single-Walled Carbon Nanotubes for Electronics and Sensors: A Review of Fundamental and Applied Aspects," *Advanced Materials,* vol. 21, pp. 29-53, Jan 2009.

[35] C. B. Jacobs, M. J. Peairs, and B. J. Venton, "Review: Carbon nanotube based electrochemical sensors for biomolecules," *Analytica Chimica Acta,* vol. 662, pp. 105-127, Mar 2010.

[36] C. Gao, Z. Guo, J. H. Liu, and X. J. Huang, "The new age of carbon nanotubes: An updated review of functionalized carbon nanotubes in electrochemical sensors," *Nanoscale,* vol. 4, pp. 1948-1963, 2012.

[37] H. Ago, K. Petritsch, M. S. P. Shaffer, A. H. Windle, and R. H. Friend, "Composites of carbon nanotubes and conjugated polymers for photovoltaic devices," *Advanced Materials,* vol. 11, pp. 1281-+, Oct 1999.

[38] D. M. Guldi, G. M. A. Rahman, M. Prato, N. Jux, S. H. Qin, and W. Ford, "Single-wall carbon nanotubes as integrative building blocks for solar-energy conversion," *Angewandte Chemie-International Edition,* vol. 44, pp. 2015-2018, 2005.

[39] G. L. Che, B. B. Lakshmi, E. R. Fisher, and C. R. Martin, "Carbon nanotubule membranes for electrochemical energy storage and production," *Nature,* vol. 393, pp. 346-349, May 1998.

[40] E. Frackowiak and F. Beguin, "Electrochemical storage of energy in carbon nanotubes and nanostructured carbons," *Carbon,* vol. 40, pp. 1775-1787, 2002.

[41] V. L. Pushparaj, M. M. Shaijumon, A. Kumar, S. Murugesan, L. Ci, R. Vajtai, *et al.*, "Flexible energy storage devices based on nanocomposite paper," *Proceedings of the National Academy of Sciences of the United States of America,* vol. 104, pp. 13574-13577, Aug 2007.

[42] A. C. Dillon, "Carbon Nanotubes for Photoconversion and Electrical Energy Storage," *Chemical Reviews,* vol. 110, pp. 6856-6872, Nov 2010.

[43] C. Masarapu, V. Subramanian, H. W. Zhu, and B. Q. Wei, "Long-Cycle Electrochemical Behavior of Multiwall Carbon Nanotubes Synthesized on Stainless Steel in Li Ion Batteries," *Advanced Functional Materials,* vol. 19, pp. 1008-1014, Apr 2009.

[44] B. J. Landi, M. J. Ganter, C. D. Cress, R. A. DiLeo, and R. P. Raffaelle, "Carbon nanotubes for lithium ion batteries," *Energy & Environmental Science,* vol. 2, pp. 638-654, 2009.

[45] Z. L. Wang, "Nanostructures of zinc oxide," *Materials Today,* vol. 7, p. 26, 2004.

[46] Z. L. Wang, "Zinc oxide nanostructures: growth, properties and applications," *Journal of Physics-Condensed Matter,* vol. 16, pp. R829-R858, Jun 2004.

[47] G. Heiland and H. Ibach, "PYROELECTRICITY OF ZINC OXIDE," *Solid State Communications,* vol. 4, pp. 353-&, 1966.

[48] M. H. Huang, S. Mao, H. Feick, H. Q. Yan, Y. Y. Wu, H. Kind, *et al.*, "Room-temperature ultraviolet nanowire nanolasers," *Science,* vol. 292, pp. 1897-1899, Jun 2001.

[49] Y. Takahashi, M. Kanamori, A. Kondoh, H. Minoura, and Y. Ohya, "PHOTOCONDUCTIVITY OF ULTRATHIN ZINC-OXIDE FILMS," *Japanese Journal of Applied Physics Part 1-Regular Papers Short Notes & Review Papers,* vol. 33, pp. 6611-6615, Dec 1994.

[50] J. X. Wang, X. W. Sun, Y. Yang, H. Huang, Y. C. Lee, O. K. Tan, *et al.*, "Hydrothermally grown oriented ZnO nanorod arrays for gas sensing applications," *Nanotechnology,* vol. 17, pp. 4995-4998, Oct 2006.

[51] H. Kind, H. Q. Yan, B. Messer, M. Law, and P. D. Yang, "Nanowire ultraviolet photodetectors and optical switches," *Advanced Materials,* vol. 14, pp. 158-+, Jan 2002.

[52] Z. L. Wang and J. H. Song, "Piezoelectric nanogenerators based on zinc oxide nanowire arrays," *Science,* vol. 312, pp. 242-246, Apr 2006.

[53] X. D. Wang, J. H. Song, J. Liu, and Z. L. Wang, "Direct-current nanogenerator driven by ultrasonic waves," *Science,* vol. 316, pp. 102-105, Apr 2007.

[54] J. Goldberger, D. J. Sirbuly, M. Law, and P. Yang, "ZnO nanowire transistors," *Journal of Physical Chemistry B,* vol. 109, pp. 9-14, Jan 2005.

[55] X. D. Wang, J. Zhou, J. H. Song, J. Liu, N. S. Xu, and Z. L. Wang, "Piezoelectric field effect transistor and nanoforce sensor based on a single ZnO nanowire," *Nano Letters,* vol. 6, pp. 2768-2772, Dec 2006.

[56] M. Law, L. E. Greene, J. C. Johnson, R. Saykally, and P. D. Yang, "Nanowire dye-sensitized solar cells," *Nature Materials,* vol. 4, pp. 455-459, Jun 2005.

[57] J. B. Baxter and E. S. Aydil, "Nanowire-based dye-sensitized solar cells," *Applied Physics Letters,* vol. 86, Jan 2005.

[58] Q. Wan, Q. H. Li, Y. J. Chen, T. H. Wang, X. L. He, J. P. Li, *et al.*, "Fabrication and ethanol sensing characteristics of ZnO nanowire gas sensors," *Applied Physics Letters,* vol. 84, pp. 3654-3656, May 2004.

[59] B. S. Kang, Y. W. Heo, L. C. Tien, D. P. Norton, F. Ren, B. P. Gila, *et al.*, "Hydrogen and ozone gas sensing using multiple ZnO nanorods," *Applied Physics a-Materials Science & Processing,* vol. 80, pp. 1029-1032, Feb 2005.

[60] M. Ahmad, C. F. Pan, Z. X. Luo, and J. Zhu, "A Single ZnO Nanofiber-Based Highly Sensitive Amperometric Glucose Biosensor," *Journal of Physical Chemistry C,* vol. 114, pp. 9308-9313, May 2010.

[61] A. Stafiniak, B. Boratynski, A. Baranowska-Korczyc, A. Szyszka, M. Ramiaczek-Krasowska, J. Prazmowska, *et al.*, "A novel electrospun ZnO nanofibers biosensor fabrication," *Sensors and Actuators B-Chemical,* vol. 160, pp. 1413-1418, Dec 2011.

[62] M. G. Kang and L. J. Guo, "Nanoimprinted semitransparent metal electrodes and their application in organic light-emitting diodes," *Advanced Materials,* vol. 19, pp. 1391-+, May 2007.

[63] M. G. Kang and L. J. Guo, "Semitransparent Cu electrode on a flexible substrate and its

application in organic light emitting diodes," *Journal of Vacuum Science & Technology B*, vol. 25, pp. 2637-2641, Nov 2007.

[64] M. G. Kang, M. S. Kim, J. S. Kim, and L. J. Guo, "Organic Solar Cells Using Nanoimprinted Transparent Metal Electrodes," *Advanced Materials,* vol. 20, pp. 4408-4413, Dec 2008.

[65] M. G. Kang, H. J. Park, S. H. Ahn, and L. J. Guo, "Transparent Cu nanowire mesh electrode on flexible substrates fabricated by transfer printing and its application in organic solar cells," *Solar Energy Materials and Solar Cells,* vol. 94, pp. 1179-1184, Jun 2010.

[66] Y. Martin, F. Zenhausern, and H. K. Wickramasinghe, "Scattering Spectroscopy of Molecules at Nanometer Resolution," *Appl. Phys. Lett.,* vol. 68, pp. 2475-2477, 1996.

[67] R. J. Heaton, A. W. Peterson, and R. M. Georgiadis, "Electrostatic surface plasmon resonance: Direct electric field-induced hybridization and denaturation in monolayer nucleic acid films and label-free discrimination of base mismatches," *PNAS,* vol. 98, pp. 3701-3704, 2001.

[68] X. D. Hoa, A. G. Kirk, and M. Tabriziana, "Enhanced SPR response from patterned immobilization of surface bioreceptors on nano-gratings," *Biosensors and Bioelectronics,* vol. 24, pp. 3043–3048, 2009.

[69] T. Xu, H. F. Shi, Y. K. Wu, A. F. Kaplan, J. G. Ok, and L. J. Guo, "Structural Colors: From Plasmonic to Carbon Nanostructures," *Small,* vol. 7, pp. 3128-3136, Nov 2011.

[70] Y. J. Shin, C. Pina-Hernandez, Y. K. Wu, J. G. Ok, and L. J. Guo, "Facile route of flexible wire grid polarizer fabrication by angled-evaporations of aluminum on two sidewalls of an imprinted nanograting," *Nanotechnology,* vol. 23, Aug 2012.

[71] J. J. Wang, F. Walters, X. M. Liu, P. Sciortino, and X. G. Deng, "High-performance, large area, deep ultraviolet to infrared polarizers based on 40 nm line/78 nm space nanowire grids," *Applied Physics Letters,* vol. 90, Feb 2007.

[72] M. Auslender, D. Levy, and S. Hava, "One-dimensional antireflection gratings in (100) silicon: a numerical study," *Appl. Opt.,* vol. 37, pp. 369-373, 1998.

[73] T. Xu, Y. K. Wu, X. G. Luo, and L. J. Guo, "Plasmonic nanoresonators for high-resolution colour filtering and spectral imaging," *Nature Communications,* vol. 1, Aug 2010.

[74] H. J. Park, T. Xu, J. Y. Lee, A. Ledbetter, and L. J. Guo, "Photonic Color Filters Integrated with Organic Solar Cells for Energy Harvesting," *Acs Nano,* vol. 5, pp. 7055-7060, Sep 2011.

[75] J. G. Ok, H. S. Youn, M. K. Kwak, K. T. Lee, Y. J. Shin, L. J. Guo, *et al.*, "Continuous and scalable fabrication of flexible metamaterial films via roll-to-roll nanoimprint process for broadband plasmonic infrared filters," *Applied Physics Letters,* vol. 101, Nov 2012.

[76] K. W. Kolasinski, "Catalytic growth of nanowires: Vapor-liquid-solid, vapor-solid-solid, solution-liquid-solid and solid-liquid-solid growth," *Current Opinion in Solid State & Materials Science,* vol. 10, pp. 182-191, Jun-Aug 2006.

[77] X. D. Wang, C. J. Summers, and Z. L. Wang, "Large-scale hexagonal-patterned growth of aligned ZnO nanorods for nano-optoelectronics and nanosensor arrays," *Nano Letters,* vol. 4, pp. 423-426, Mar 2004.

[78] A. J. Hart and A. H. Slocum, "Rapid growth and flow-mediated nucleation of millimeter-scale aligned carbon nanotube structures from a thin-film catalyst," *Journal of Physical Chemistry B*, vol. 110, pp. 8250-8257, Apr 2006.

[79] Y. N. Xia, P. D. Yang, Y. G. Sun, Y. Y. Wu, B. Mayers, B. Gates, *et al.*, "One-dimensional nanostructures: Synthesis, characterization, and applications," *Advanced Materials*, vol. 15, pp. 353-389, Mar 2003.

[80] W. Lu and C. M. Lieber, "Semiconductor nanowires," *Journal of Physics D-Applied Physics*, vol. 39, pp. R387-R406, Nov 2006.

[81] L. D. Qin, S. Park, L. Huang, and C. A. Mirkin, "On-wire lithography," *Science*, vol. 309, pp. 113-115, Jul 2005.

[82] F. S. Ou, M. M. Shaijumon, L. Ci, D. Benicewicz, R. Vajtai, and P. M. Ajayan, "Multisegmented one-dimensional hybrid structures of carbon nanotubes and metal nanowires," *Applied Physics Letters*, vol. 89, Dec 2006.

[83] B. Z. Tian, X. L. Zheng, T. J. Kempa, Y. Fang, N. F. Yu, G. H. Yu, *et al.*, "Coaxial silicon nanowires as solar cells and nanoelectronic power sources," *Nature*, vol. 449, pp. 885-U8, Oct 2007.

[84] B. Tian, T. J. Kempa, and C. M. Lieber, "Single nanowire photovoltaics," *Chemical Society Reviews*, vol. 38, pp. 16-24, 2009.

[85] M. J. Bierman, Y. K. A. Lau, and S. Jin, "Hyperbranched PbS and PbSe nanowires and the effect of hydrogen gas on their synthesis," *Nano Letters*, vol. 7, pp. 2907-2912, Sep 2007.

[86] M. J. Bierman, Y. K. A. Lau, A. V. Kvit, A. L. Schmitt, and S. Jin, "Dislocation-driven nanowire growth and Eshelby twist," *Science*, vol. 320, pp. 1060-1063, May 2008.

[87] K. A. Dick, K. Deppert, M. W. Larsson, T. Martensson, W. Seifert, L. R. Wallenberg, *et al.*, "Synthesis of branched 'nanotrees' by controlled seeding of multiple branching events," *Nature Materials*, vol. 3, pp. 380-384, Jun 2004.

[88] K. A. Dick, S. Kodambaka, M. C. Reuter, K. Deppert, L. Samuelson, W. Seifert, *et al.*, "The morphology of axial and branched nanowire heterostructures," *Nano Letters*, vol. 7, pp. 1817-1822, Jun 2007.

[89] J. H. Zou, S. I. Khondaker, Q. Huo, and L. Zhai, "A General Strategy to Disperse and Functionalize Carbon Nanotubes Using Conjugated Block Copolymers," *Advanced Functional Materials*, vol. 19, pp. 479-483, Feb 2009.

[90] A. L. M. Reddy, M. M. Shaijumon, S. R. Gowda, and P. M. Ajayan, "Coaxial MnO2/Carbon Nanotube Array Electrodes for High-Performance Lithium Batteries," *Nano Letters*, vol. 9, pp. 1002-1006, Mar 2009.

[91] A. J. Miller, R. A. Hatton, and S. R. P. Silva, "Interpenetrating multiwall carbon nanotube electrodes for organic solar cells," *Applied Physics Letters*, vol. 89, Sep 2006.

[92] B. Li, L. Y. Li, B. B. Wang, and C. Y. Li, "Alternating patterns on single-walled carbon nanotubes," *Nature Nanotechnology*, vol. 4, pp. 358-362, Jun 2009.

[93] M. S. Dresselhaus, G. Dresselhaus, and P. Avouris, Eds., *Carbon Nanotubes: Synthesis, Structure, Properties, and Applications* (Topics in Applied Physics. Springer, 2001, p.^pp. Pages.

[94] M. Endo, T. Hayashi, Y. A. Kim, M. Terrones, and M. S. Dresselhaus, "Applications of carbon nanotubes in the twenty-first century," *Philosophical Transactions of the Royal Society of London Series A,* vol. 362, pp. 2223-2238, Oct 2004.

[95] S. S. Fan, M. G. Chapline, N. R. Franklin, T. W. Tombler, A. M. Cassell, and H. J. Dai, "Self-oriented regular arrays of carbon nanotubes and their field emission properties," *Science,* vol. 283, pp. 512-514, Jan 1999.

[96] T. Hiraoka, T. Yamada, K. Hata, D. N. Futaba, H. Kurachi, S. Uemura, *et al.*, "Synthesis of single- and double-walled carbon nanotube forests on conducting metal foils," *Journal of the American Chemical Society,* vol. 128, pp. 13338-13339, Oct 2006.

[97] N. Yamamoto, A. J. Hart, E. J. Garcia, S. S. Wicks, H. M. Duong, A. H. Slocum, *et al.*, "High-yield growth and morphology control of aligned carbon nanotubes on ceramic fibers for multifunctional enhancement of structural composites," *Carbon,* vol. 47, pp. 551-560, Mar 2009.

[98] L. T. Qu, Y. Zhao, and L. M. Dai, "Carbon microfibers sheathed with aligned carbon nanotubes: Towards multidimensional, multicomponent, and multifunctional nanomaterials," *Small,* vol. 2, pp. 1052-1059, Aug 2006.

[99] A. J. Hart and A. H. Slocum, "Force output, control of film structure, and microscale shape transfer by carbon nanotube growth under mechanical pressure," *Nano Letters,* vol. 6, pp. 1254-1260, Jun 2006.

[100] J. T. Hu, M. Ouyang, P. D. Yang, and C. M. Lieber, "Controlled growth and electrical properties of heterojunctions of carbon nanotubes and silicon nanowires," *Nature,* vol. 399, pp. 48-51, May 1999.

[101] J. Luo, L. Zhang, Y. J. Zhang, and J. Zhu, "Controlled growth of one-dimensional metal-semiconductor and metal-carbon nanotube heterojunctions," *Advanced Materials,* vol. 14, pp. 1413-1414, Oct 2002.

[102] J. Luo, Z. P. Huang, Y. G. Zhao, L. Zhang, and J. Zhu, "Arrays of heterojunctions of Ag nanowires and amorphous cairbon nanotubes," *Advanced Materials,* vol. 16, pp. 1512-+, Sep 2004.

[103] R. Y. Li, X. C. Sun, X. R. Zhou, M. Cai, and X. L. Sun, "Aligned heterostructures of single-crystalline tin nanowires encapsulated in amorphous carbon nanotubes," *Journal of Physical Chemistry C,* vol. 111, pp. 9130-9135, Jul 2007.

[104] V. Subramanian, H. W. Zhu, and B. Q. Wei, "Synthesis and electrochemical characterizations of amorphous manganese oxide and single walled carbon nanotube composites as supercapacitor electrode materials," *Electrochemistry Communications,* vol. 8, pp. 827-832, May 2006.

[105] H. L. Hsiao, Z. Y. Liu, and P. H. Lee, "Acetylene assisted formation of GaN-carbon nanotubes heterojunction nanowires," in *2nd International Conference on New Diamond and Nano Carbons*, Taipei, TAIWAN, 2008, pp. 537-540.

[106] S. Sun, D. Yang, G. Zhang, E. Sacher, and J. P. Dodelet, "Synthesis and characterization of platinum nanowire-carbon nanotube heterostructures," *Chemistry of Materials,* vol. 19, pp. 6376-6378, Dec 2007.

[107] J. W. Liu, Y. T. Kuo, K. J. Klabunde, C. Rochford, J. Wu, and J. Li, "Novel Dye-Sensitized Solar Cell Architecture Using TiO2-Coated Vertically Aligned Carbon Nanofiber Arrays," *Acs Applied Materials & Interfaces,* vol. 1, pp. 1645-1649, Aug 2009.

[108] M. H. Huang, Y. Y. Wu, H. Feick, N. Tran, E. Weber, and P. D. Yang, "Catalytic growth of zinc oxide nanowires by vapor transport," *Advanced Materials,* vol. 13, pp. 113-116, Jan 2001.

[109] S. T. Ho, K. C. Chen, H. A. Chen, H. Y. Lin, C. Y. Cheng, and H. N. Lin, "Catalyst-free surface-roughness-assisted growth of large-scale vertically aligned zinc oxide nanowires by thermal evaporation," *Chemistry of Materials,* vol. 19, pp. 4083-4086, Aug 2007.

[110] B. Weintraub, Y. L. Deng, and Z. L. Wang, "Position-controlled seedless growth of ZnO nanorod arrays on a polymer substrate via wet chemical synthesis," *Journal of Physical Chemistry C,* vol. 111, pp. 10162-10165, Jul 2007.

[111] S. Xu, Y. G. Wei, J. Liu, R. Yang, and Z. L. Wang, "Integrated Multilayer Nanogenerator Fabricated Using Paired Nanotip-to-Nanowire Brushes," *Nano Letters,* vol. 8, pp. 4027-4032, Nov 2008.

[112] S. H. Dalal, D. L. Baptista, K. B. K. Teo, R. G. Lacerda, D. A. Jefferson, and W. I. Milne, "Controllable growth of vertically aligned zinc oxide nanowires using vapour deposition," *Nanotechnology,* vol. 17, pp. 4811-4818, Oct 2006.

[113] W. D. Zhang, "Growth of ZnO nanowires on modified well-aligned carbon nanotube arrays," *Nanotechnology,* vol. 17, pp. 1036-1040, Feb 2006.

[114] H. Liu, S. H. Li, J. Zhai, H. J. Li, Q. S. Zheng, L. Jiang, *et al.*, "Self-assembly of large-scale micropatterns on aligned carbon nanotube films," *Angewandte Chemie-International Edition,* vol. 43, pp. 1146-1149, 2004.

[115] C. Py, R. Bastien, J. Bico, B. Roman, and A. Boudaoud, "3D aggregation of wet fibers," *Europhysics Letters,* vol. 77, 2007.

[116] K. Wang, J. J. Chen, W. L. Zhou, Y. Zhang, Y. F. Yan, J. Pern, *et al.*, "Direct growth of highly mismatched type IIZnO/ZnSe core/shell nanowire arrays on transparent conducting oxide substrates for solar cell applications," *Advanced Materials,* vol. 20, pp. 3248-+, Sep 2008.

[117] P. D. Yang, H. Q. Yan, S. Mao, R. Russo, J. Johnson, R. Saykally, *et al.*, "Controlled growth of ZnO nanowires and their optical properties," *Advanced Functional Materials,* vol. 12, pp. 323-331, May 2002.

[118] Z. Y. Jiang, Z. X. Xie, X. H. Zhang, S. C. Lin, T. Xu, S. Y. Xie, *et al.*, "Synthesis of single-crystalline ZnO polyhedral submicrometer-sized hollow beads using laser-assisted growth with ethanol droplets as soft templates," *Advanced Materials,* vol. 16, pp. 904-907, Jun 2004.

[119] E. Einarsson, H. Shiozawa, C. Kramberger, M. H. Rummeli, A. Gruneis, T. Pichler, *et al.*, "Revealing the small-bundle internal structure of vertically aligned single-walled carbon nanotube films," *Journal of Physical Chemistry C,* vol. 111, pp. 17861-17864, Dec 2007.

[120] E. Verploegen, G. Chia, S. Tawfick, M. De Volder, A. J. Hart, and R. E. Cohen, "Non-destructive characterization of structural hierarchy within aligned carbon nanotube assemblies," *(in preparation),* 2009.

[121] R. D. Bennett, A. J. Hart, and R. E. Cohen, "Controlling the morphology of carbon nanotnbe films by varying the areal density of catalyst nanoclusters using block-copolymer micellar thin films," *Advanced Materials,* vol. 18, pp. 2274-+, Sep 2006.

[122] G. D. Nessim, A. J. Hart, J. S. Kim, D. Acquaviva, J. H. Oh, C. D. Morgan, *et al.*,

"Tuning of Vertically-Aligned Carbon Nanotube Diameter and Areal Density through Catalyst Pre-Treatment," *Nano Letters,* vol. 8, pp. 3587-3593, Nov 2008.

[123] A. B. Djurisic and Y. H. Leung, "Optical properties of ZnO nanostructures," *Small,* vol. 2, pp. 944-961, Aug 2006.

[124] K. Vanheusden, W. L. Warren, C. H. Seager, D. R. Tallant, J. A. Voigt, and B. E. Gnade, "Mechanisms behind green photoluminescence in ZnO phosphor powders," *Journal of Applied Physics,* vol. 79, pp. 7983-7990, May 1996.

[125] S. Chakrabarti, D. Ganguli, and S. Chaudhuri, "Photoluminescence of ZnO nanocrystallites confined in sol-gel silica matrix," *Journal of Physics D-Applied Physics,* vol. 36, pp. 146-151, Jan 2003.

[126] G. W. Sears, "A growth mechanism for mercury whiskers," *Acta Metallurgica,* vol. 3, pp. 361-366, 1955.

[127] W. K. Burton, N. Cabrera, and F. C. Frank, "ROLE OF DISLOCATIONS IN CRYSTAL GROWTH," *Nature,* vol. 163, pp. 398-399, 1949.

[128] W. K. Burton, N. Cabrera, and F. C. Frank, "THE GROWTH OF CRYSTALS AND THE EQUILIBRIUM STRUCTURE OF THEIR SURFACES," *Philosophical Transactions of the Royal Society of London Series a-Mathematical and Physical Sciences,* vol. 243, pp. 299-358, 1951.

[129] J. D. Eshelby, "SCREW DISLOCATIONS IN THIN RODS," *Journal of Applied Physics,* vol. 24, pp. 176-179, 1953.

[130] G. W. Sears, "MERCURY WHISKERS," *Acta Metallurgica,* vol. 1, pp. 457-459, 1953.

[131] H. Heyer, "KINETICS OF CRYSTAL GROWTH," *Angewandte Chemie-International Edition,* vol. 5, pp. 67-&, 1966.

[132] R. L. Parker, R. L. Anderson, and S. C. Hardy, "GROWTH AND EVAPORATION KINETICS AND SURFACE DIFFUSION OF K AND HG CRYSTAL WHISKERS," *Applied Physics Letters,* vol. 3, pp. 93-95, 1963.

[133] J. B. Baxter and E. S. Aydil, "Epitaxial growth of ZnO nanowires on a- and c-plane sapphire," *Journal of Crystal Growth,* vol. 274, pp. 407-411, Feb 2005.

[134] R. W. Balluffi, S. M. Allen, and W. C. Carter, *Kinetics of Materials*. Hoboken, New Jersey: John Wiley & Sons, Inc., 2005.

[135] T. R. Hogness, "The surface tensions and densities of liquid mercury, cadmium, zinc, lead, tin and bismuth," *Journal of the American Chemical Society,* vol. 43, pp. 1621-1628, Jul-Dec 1921.

[136] C. G. Maier, "Adjusted vapor pressures of zinc and cadmium," *Journal of the American Chemical Society,* vol. 48, pp. 356-364, Jan 1926.

[137] D. Segets, J. Gradl, R. K. Taylor, V. Vassilev, and W. Peukert, "Analysis of Optical Absorbance Spectra for the Determination of ZnO Nanoparticle Size Distribution, Solubility, and Surface Energy," *Acs Nano,* vol. 3, pp. 1703-1710, Jul 2009.

[138] R. H. Lamoreaux, D. L. Hildenbrand, and L. Brewer, "HIGH-TEMPERATURE VAPORIZATION BEHAVIOR OF OXIDES .2. OXIDES OF BE, MG, CA, SR, BA, B, AL, GA, IN, TL, SI, GE, SN, PB, ZN, CD, AND HG," *Journal of Physical and Chemical Reference Data,* vol. 16, pp. 419-443, 1987.

[139] S. Tawfick, K. O'Brien, and A. J. Hart, "Flexible High-Conductivity Carbon-Nanotube Interconnects Made by Rolling and Printing," *Small,* vol. 5, pp. 2467-2473, Nov 2009.

[140] S. T. Ho, C. Y. Wang, H. L. Liu, and H. N. Lin, "Catalyst-free selective-area growth of vertically aligned zinc oxide nanowires," *Chemical Physics Letters,* vol. 463, pp. 141-144, Sep 2008.

[141] C. L. Pint, Y. Q. Xu, E. Morosan, and R. H. Hauge, "Alignment dependence of one-dimensional electronic hopping transport observed in films of highly aligned, ultralong single-walled carbon nanotubes," *Applied Physics Letters,* vol. 94, May 2009.

[142] D. A. Neamen, *Semiconductor Physics and Devices: Basic Principles*, 3 ed. New York: McGraw-Hill, 2003.

[143] M. Shiraishi and M. Ata, "Work function of carbon nanotubes," *Carbon,* vol. 39, pp. 1913-1917, 2001.

[144] H. Ago, T. Kugler, F. Cacialli, W. R. Salaneck, M. S. P. Shaffer, A. H. Windle, *et al.*, "Work functions and surface functional groups of multiwall carbon nanotubes," *Journal of Physical Chemistry B,* vol. 103, pp. 8116-8121, Sep 1999.

[145] S. H. Jo, D. Banerjee, and Z. F. Ren, "Field emission of zinc oxide nanowires grown on carbon cloth," *Applied Physics Letters,* vol. 85, pp. 1407-1409, Aug 2004.

[146] C. Soci, A. Zhang, B. Xiang, S. A. Dayeh, D. P. R. Aplin, J. Park, *et al.*, "ZnO nanowire UV photodetectors with high internal gain," *Nano Letters,* vol. 7, pp. 1003-1009, Apr 2007.

[147] Y. Z. Jin, J. P. Wang, B. Q. Sun, J. C. Blakesley, and N. C. Greenham, "Solution-processed ultraviolet photodetedtors based on colloidal ZnO nanoparticles," *Nano Letters,* vol. 8, pp. 1649-1653, Jun 2008.

[148] W. Kim and K. S. Chu, "ZnO nanowire field-effect transistor as a UV photodetector; optimization for maximum sensitivity," *Physica Status Solidi a-Applications and Materials Science,* vol. 206, pp. 179-182, Jan 2009.

[149] C. M. Soukoulis and M. Wegener, "Past achievements and future challenges in the development of three-dimensional photonic metamaterials," *Nature Photonics,* vol. 5, pp. 523-530, Sep 2011.

[150] H. F. Wang, C. J. R. Sheppard, K. Ravi, S. T. Ho, and G. Vienne, "Fighting against diffraction: apodization and near field diffraction structures," *Laser & Photonics Reviews,* vol. 6, pp. 354-392, May 2012.

[151] Z. G. Chen, M. Segev, and D. N. Christodoulides, "Optical spatial solitons: historical overview and recent advances," *Reports on Progress in Physics,* vol. 75, Aug 2012.

[152] J. D. Plummer, M. D. Deal, and P. B. Griffin, *Silicone VLSI Technology*. Upper Saddle River, NJ: Prentice Hall, 2000.

[153] A. Rodriguez, S. M. Olaizola, and I. Ayerdi, *Laser Interference Lithography for Micro- and Nano-Fabrication*. Saarbrücken, Germany: VDM Publishing, 2011.

[154] N. Liu, M. Hentschel, T. Weiss, A. P. Alivisatos, and H. Giessen, "Three-Dimensional Plasmon Rulers," *Science,* vol. 332, pp. 1407-1410, Jun 2011.

[155] D. Bratton, D. Yang, J. Y. Dai, and C. K. Ober, "Recent progress in high resolution lithography," *Polymers for Advanced Technologies,* vol. 17, pp. 94-103, Feb 2006.

[156] Z. H. Nie and E. Kumacheva, "Patterning surfaces with functional polymers," *Nature Materials,* vol. 7, pp. 277-290, Mar 2008.

[157] M. G. Kang, T. Xu, H. J. Park, X. G. Luo, and L. J. Guo, "Efficiency Enhancement of Organic Solar Cells Using Transparent Plasmonic Ag Nanowire Electrodes," *Advanced Materials,* vol. 22, pp. 4378-+, Oct 2010.

[158] A. F. Kaplan, T. Xu, Y. K. Wu, and L. J. Guo, "Multilayer pattern transfer for plasmonic color filter applications," *Journal of Vacuum Science & Technology B,* vol. 28, pp. C6O60-C6O63, Nov 2010.

[159] S. H. Ahn and L. J. Guo, "High-speed roll-to-roll nanoimprint lithography on flexible plastic substrates," *Advanced Materials,* vol. 20, pp. 2044-+, Jun 2008.

[160] S. H. Ahn and L. J. Guo, "High-speed Roll-to-Roll Nanoimprint Lithography on Flexible Substrate and Mold-separation Analysis," in *Advanced Fabrication Technologies for Micro/Nano Optics and Photonics Ii*. vol. 7205, T. J. Suleski, W. V. Schoenfeld, and J. J. Wang, Eds., ed, 2009.

[161] J. G. Ok, H. J. Park, M. K. Kwak, C. A. Pina-Hernandez, S. H. Ahn, and L. J. Guo, "Continuous Patterning of Nanogratings by Nanochannel-Guided Lithography on Liquid Resists," *Advanced Materials,* vol. 23, pp. 4444-+, Oct 2011.

[162] S. H. Ahn*, J. G. Ok*, M. K. Kwak, K.-T. Lee, J. Y. Lee, and L. J. Guo, "Template-free Vibrational Indentation Patterning (VIP) of micro/nano-scale grating structures with real-time pitch and angle tunability," *Advanced Functional Materials,* vol. in press, 2013.

[163] S. H. Ahn, J. S. Kim, and L. J. Guo, "Bilayer metal wire-grid polarizer fabricated by roll-to-roll nanoimprint lithography on flexible plastic substrate," *Journal of Vacuum Science & Technology B,* vol. 25, pp. 2388-2391, Nov 2007.

[164] S. H. Ahn and L. J. Guo, "Large-Area Roll-to-Roll and Roll-to-Plate Nanoimprint Lithography: A Step toward High-Throughput Application of Continuous Nanoimprinting," *Acs Nano,* vol. 3, pp. 2304-2310, Aug 2009.

[165] H. J. Park, M. G. Kang, S. H. Ahn, and L. J. Guo, "A Facile Route to Polymer Solar Cells with Optimum Morphology Readily Applicable to a Roll-to-Roll Process without Sacrificing High Device Performance," *Advanced Materials,* vol. 22, pp. E247-+, Sep 2010.

[166] P. Maury, D. Turkenburg, N. Stroeks, P. Giesen, I. Barbu, E. Meinders, *et al.*, "Roll-to-roll UV imprint lithography for flexible electronics," *Microelectronic Engineering,* vol. 88, pp. 2052-2055, Aug 2011.

[167] R. R. Sondergaard, M. Hosel, and F. C. Krebs, "Roll-to-Roll fabrication of large area functional organic materials," *Journal of Polymer Science Part B-Polymer Physics,* vol. 51, pp. 16-34, Jan 2013.

[168] J. Noh, M. Jung, K. Jung, G. Lee, S. Lim, D. Kim, *et al.*, "Integrable single walled carbon nanotube (SWNT) network based thin film transistors using roll-to-roll gravure and inkjet," *Organic Electronics,* vol. 12, pp. 2185-2191, Dec 2011.

[169] S. Bae, H. Kim, Y. Lee, X. F. Xu, J. S. Park, Y. Zheng, *et al.*, "Roll-to-roll production of 30-inch graphene films for transparent electrodes," *Nature Nanotechnology,* vol. 5, pp. 574-578, Aug 2010.

[170] Z. Y. Juang, C. Y. Wu, A. Y. Lu, C. Y. Su, K. C. Leou, F. R. Chen, *et al.*, "Graphene

synthesis by chemical vapor deposition and transfer by a roll-to-roll process," *Carbon,* vol. 48, pp. 3169-3174, Sep 2010.

[171] J. J. Vilatela and D. Eder, "Nanocarbon Composites and Hybrids in Sustainability: A Review," *Chemsuschem,* vol. 5, pp. 456-478, 2012.

[172] T. Makela, S. Jussila, H. Kosonen, T. G. Backlund, H. G. O. Sandberg, and H. Stubb, "Utilizing roll-to-roll techniques for manufacturing source-drain electrodes for all-polymer transistors," *Synthetic Metals,* vol. 153, pp. 285-288, Sep 2005.

[173] J. M. Verilhac, M. Benwadih, A. L. Seiler, S. Jacob, C. Bory, J. Bablet, *et al.*, "Step toward robust and reliable amorphous polymer field-effect transistors and logic functions made by the use of roll to roll compatible printing processes," *Organic Electronics,* vol. 11, pp. 456-462, Mar 2010.

[174] C. E. Lue, I. S. Wang, C. H. Huang, Y. T. Shiao, H. C. Wang, C. M. Yang, *et al.*, "pH sensing reliability of flexible ITO/PET electrodes on EGFETs prepared by a roll-to-roll process," *Microelectronics Reliability,* vol. 52, pp. 1651-1654, Aug 2012.

[175] T. Makela and T. Haatainen, "Roll-to-roll pilot nanoimprinting process for backlight devices," *Microelectronic Engineering,* vol. 97, pp. 89-91, Sep 2012.

[176] C. Ryan, C. W. Christenson, B. Valle, A. Saini, J. Lott, J. Johnson, *et al.*, "Roll-to-Roll Fabrication of Multilayer Films for High Capacity Optical Data Storage," *Advanced Materials,* vol. 24, pp. 5222-5226, Oct 2012.

[177] T. Steenberg, H. A. Hjuler, C. Terkelsen, M. T. R. Sanchez, L. N. Cleemann, and F. C. Krebs, "Roll-to-roll coated PBI membranes for high temperature PEM fuel cells," *Energy & Environmental Science,* vol. 5, pp. 6076-6080, Mar 2012.

[178] H. Park, H. Kang, Y. Lee, Y. Park, J. Noh, and G. Cho, "Fully roll-to-roll gravure printed rectenna on plastic foils for wireless power transmission at 13.56 MHz," *Nanotechnology,* vol. 23, Aug 2012.

[179] X. Cheng, L. J. Guo, and P. F. Fu, "Room-temperature, low-pressure nanoimprinting based on cationic photopolymerization of novel epoxysilicone monomers," *Advanced Materials,* vol. 17, pp. 1419-+, Jun 2005.

[180] C. Pina-Hernandez, L. J. Guo, and P. F. Fu, "High-Resolution Functional Epoxysilsesquioxane-Based Patterning Layers for Large-Area Nanoimprinting," *Acs Nano,* vol. 4, pp. 4776-4784, Aug 2010.

[181] M. J. Preiner, K. T. Shimizu, J. S. White, and N. A. Melosh, "Efficient optical coupling into metal-insulator-metal plasmon modes with subwavelength diffraction gratings," *Applied Physics Letters,* vol. 92, Mar 2008.

[182] I. Puscasu and W. L. Schaich, "Narrow-band, tunable infrared emission from arrays of microstrip patches," *Applied Physics Letters,* vol. 92, Jun 2008.

[183] Y. T. Chang, Y. T. Wu, J. H. Lee, H. H. Chen, C. Y. Hsueh, H. F. Huang, *et al.*, "Emission properties of Ag/dielectric/Ag plasmonic thermal emitter with different lattice type, hole shape, and dielectric material," *Applied Physics Letters,* vol. 95, Nov 2009.

[184] C. M. Wang, Y. C. Chang, M. W. Tsai, Y. H. Ye, C. Y. Chen, Y. W. Jiang, *et al.*, "Angle-independent infrared filter assisted by localized surface plasmon polariton," *Ieee Photonics Technology Letters,* vol. 20, pp. 1103-1105, Jul-Aug 2008.

[185] C. W. Cheng, M. N. Abbas, Z. C. Chang, M. H. Shih, C. M. Wang, M. C. Wu, *et al.*,

"Angle-independent plasmonic infrared band-stop reflective filter based on the Ag/SiO2/Ag T-shaped array," *Optics Letters,* vol. 36, pp. 1440-1442, Apr 2011.

[186] C. Koechlin, P. Bouchon, F. Pardo, J. Jaeck, X. Lafosse, J. L. Pelouard, *et al.*, "Total routing and absorption of photons in dual color plasmonic antennas," *Applied Physics Letters,* vol. 99, p. 3, Dec 2011.

[187] P. Bouchon, C. Koechlin, F. Pardo, R. Haidar, and J. L. Pelouard, "Wideband omnidirectional infrared absorber with a patchwork of plasmonic nanoantennas," *Optics Letters,* vol. 37, pp. 1038-1040, Mar 2012.

[188] N. Liu, T. Weiss, M. Mesch, L. Langguth, U. Eigenthaler, M. Hirscher, *et al.*, "Planar Metamaterial Analogue of Electromagnetically Induced Transparency for Plasmonic Sensing," *Nano Letters,* vol. 10, pp. 1103-1107, Apr 2010.

[189] N. Liu, M. Mesch, T. Weiss, M. Hentschel, and H. Giessen, "Infrared Perfect Absorber and Its Application As Plasmonic Sensor," *Nano Letters,* vol. 10, pp. 2342-2348, Jul 2010.

[190] J. M. Hao, J. Wang, X. L. Liu, W. J. Padilla, L. Zhou, and M. Qiu, "High performance optical absorber based on a plasmonic metamaterial," *Applied Physics Letters,* vol. 96, Jun 2010.

[191] T. Maier and H. Bruckl, "Wavelength-tunable microbolometers with metamaterial absorbers," *Optics Letters,* vol. 34, pp. 3012-3014, Oct 2009.

[192] T. Maier and H. Brueckl, "Multispectral microbolometers for the midinfrared," *Optics Letters,* vol. 35, pp. 3766-3768, Nov 2010.

[193] A. Greenwald, "R2R metamaterials, MRS proc," ed.

[194] T. Ling, S. L. Chen, and L. J. Guo, "High-sensitivity and wide-directivity ultrasound detection using high Q polymer microring resonators," *Applied Physics Letters,* vol. 98, May 2011.

[195] K. Y. Suh, J. Park, and H. H. Lee, "Controlled polymer dewetting by physical confinement," *Journal of Chemical Physics,* vol. 116, pp. 7714-7718, May 2002.

[196] M. K. Kwak, "Phase litho," ed.

[197] C. Pina-Hernandez, P. F. Fu, and L. J. Guo, "Easy duplication of stamps using UV-cured fluoro-silsesquioxane for nanoimprint lithography," *Journal of Vacuum Science & Technology B,* vol. 26, pp. 2426-2429, Nov 2008.

[198] C. M. Bingham, H. Tao, X. L. Liu, R. D. Averitt, X. Zhang, and W. J. Padilla, "Planar wallpaper group metamaterials for novel terahertz applications," *Optics Express,* vol. 16, pp. 18565-18575, Nov 2008.

[199] S. H. Ahn and L. J. Guo, "Dynamic Nanoinscribing for Continuous and Seamless Metal and Polymer Nanogratings," *Nano Letters,* vol. 9, pp. 4392-4397, Dec 2009.

[200] J. L. White and D. Huang, "EXTRUDATE SWELL AND EXTRUSION PRESSURE LOSS OF POLYMER MELTS FLOWING THROUGH RECTANGULAR AND TRAPEZOIDAL DIES," *Polymer Engineering and Science,* vol. 21, pp. 1101-1107, 1981.

[201] L. Chen, J. J. Wang, F. Walters, X. G. Deng, M. Buonanno, S. Tai, *et al.*, "Large flexible nanowire grid visible polarizer made by nanoimprint lithography," *Applied Physics*

Letters, vol. 90, Feb 2007.

[202] C. T. Pan and C. H. Su, "Fabrication of gapless triangular micro-lens array," *Sensors and Actuators a-Physical,* vol. 134, pp. 631-640, Mar 2007.

[203] J. J. Chae, S. H. Lee, and K. Y. Suh, "Fabrication of Multiscale Gradient Polymer Patterns by Direct Molding and Spatially Controlled Reflow," *Advanced Functional Materials,* vol. 21, pp. 1147-1153, Mar 2011.

[204] J. A. Brydson, *Flow properties of polymer melts*. New York: Van Nostrand Reinhold Co., 1970.

[205] J. J. Dumond and H. Y. Low, "Recent developments and design challenges in continuous roller micro- and nanoimprinting," *Journal of Vacuum Science & Technology B,* vol. 30, Jan 2012.

[206] S. H. Ahn and L. J. Guo, "Dynamic Nanoinscribing for Continuous and Seamless Metal and Polymer Nanogratings," *Nano Lett.,* vol. 9, pp. 4392-4397, 2009.

[207] M. Sitti and R. S. Fearing, "Synthetic gecko foot-hair micro/nano-structures as dry adhesives," *Journal of Adhesion Science and Technology,* vol. 17, pp. 1055-1073, 2003.

[208] A. Jo, W. Joo, W.-H. Jin, H. Nam, and J. K. Kim, "Ultrahigh-density phase-change data storage without the use of heating," *Nat. Nanotech.,* vol. 4, pp. 727-731, 2009.

[209] H. G. Shin, J. T. Kwon, Y. H. Seo, and B. H. Kim, "Development of 3d micro–nano hybrid patterns using anodized aluminum and micro-indentation," *Thin Solid Films,* vol. 516, pp. 6438–6443, 2008.

[210] J. Y. Kim, K. Lee, N. E. Coates, D. Moses, T. Q. Nguyen, M. Dante, *et al.*, "Efficient tandem polymer solar cells fabricated by all-solution processing," *Science,* vol. 317, pp. 222-225, Jul 2007.

[211] V. E. Ferry, M. A. Verschuuren, M. C. van Lare, R. E. I. Schropp, H. A. Atwater, and A. Polman, "Optimized Spatial Correlations for Broadband Light Trapping Nanopatterns in High Efficiency Ultrathin Film a-Si:H Solar Cells," *Nano Letters,* vol. 11, pp. 4239-4245, Oct 2011.

[212] M. G. Deceglie, V. E. Ferry, A. P. Alivisatos, and H. A. Atwater, "Design of Nanostructured Solar Cells Using Coupled Optical and Electrical Modeling," *Nano Letters,* vol. 12, pp. 2894-2900, Jun 2012.

[213] H. Hillmer, A. Grabmaier, H. L. Zhu, S. Hansmann, and H. Burkhard, "CONTINUOUSLY CHIRPED DFB GRATINGS BY SPECIALLY BENT WAVE-GUIDES FOR TUNABLE LASERS," *Journal of Lightwave Technology,* vol. 13, pp. 1905-1912, Sep 1995.

[214] N. Chen, Y. Nakano, K. Okamoto, K. Tada, G. I. Morthier, and R. G. Baets, "Analysis, fabrication, and characterization of tunable DFB lasers with chirped gratings," *Ieee Journal of Selected Topics in Quantum Electronics,* vol. 3, pp. 541-546, Apr 1997.

[215] R. Steingruber, M. Mohrle, A. Sigmund, and W. Furst, "Continuously chirped gratings for DFB-lasers fabricated by direct write electron-beam lithography," *Microelectronic Engineering,* vol. 61-2, pp. 331-335, Jul 2002.

[216] V. Lien, Y. Wu, D. Zhang, Y. Berdichevsky, J. Choi, and Y.-H. Lo, "A Novel Technology for Fabricating Gratings of Any Chirp Characteristics by Design," *IEEE PHOTONICS TECHNOLOGY LETTERS,* vol. 15, pp. 712-714, 2003.

[217] Y.-T. Yoon, H.-S. Lee, S.-S. Lee, S. H. Kim, J.-D. Park, and K.-D. Lee, "Color filter incorporating a subwavelength patterned grating in poly silicon," *OPTICS EXPRESS*, vol. 16, pp. 2374-2380, 2008.

[218] J. S. Bouillard, S. Vilain, W. Dickson, G. A. Wurtz, and A. V. Zayats, "Broadband and broadangle SPP antennas based on plasmonic crystals with linear chirp," *Scientific Reports*, vol. 2, Nov 2012.

[219] E. G. Loewen and E. Popov, *Diffraction Gratings and Applications*. New York: Marcel Dekker, Inc., 1997.

[220] K. D. Hong, G. F. Brand, and T. Idehara, "APPLICATION OF BLAZED GRATINGS TO MILLIMETER-SUBMILLIMETER WAVE GYROTRONS," *Journal of Applied Physics*, vol. 74, pp. 2197-2202, Aug 1993.

[221] X. Wang, D. Wilson, R. Muller, P. Maker, and D. Psaltis, "Liquid-crystal blazed-grating beam deflector," *Applied Optics*, vol. 39, pp. 6545-6555, Dec 2000.

[222] S. H. Lim and R. K. Kostuk, "Field-of-View extender for a novel camera system - art. no. 648815," in *Conference on Practical Holography XXI*, San Jose, CA, 2007, pp. 48815-48815.

[223] C. H. Chang, R. K. Heilmann, R. C. Fleming, J. Carter, E. Murphy, T. C. Bailey, *et al.*, "Fabrication of sawtooth diffraction gratings using nanoimprint lithography," *Journal of Vacuum Science & Technology B*, vol. 21, pp. 2755-2759, Nov-Dec 2003.

[224] H. Lin and L. F. Li, "Fabrication of extreme-ultraviolet blazed gratings by use of direct argon-oxygen ion-beam etching through a rectangular photoresist mask," *Applied Optics*, vol. 47, pp. 6212-6218, Nov 2008.

[225] J. R. Yan, Q. H. Wang, D. H. Li, and J. D. Zhang, "Edge-Lighting Light Guide Plate Based on Micro-Prism for Liquid Crystal Display," *Journal of Display Technology*, vol. 5, pp. 355-357, Sep 2009.

[226] C. F. Lin, Y. B. Fang, and P. H. Yang, "Optimized Micro-Prism Diffusion Film for Slim-Type Bottom-Lit Backlight Units," *Journal of Display Technology*, vol. 7, pp. 3-9, Jan 2011.

[227] H. Yoon, S. G. Oh, D. S. Kang, J. M. Park, S. J. Choi, K. Y. Suh, *et al.*, "Arrays of Lucius microprisms for directional allocation of light and autostereoscopic three-dimensional displays," *Nature Communications*, vol. 2, Aug 2011.

[228] J. Ok, S. Tawfick, K. Juggernauth, K. Sun, Y. Zhang, and A. Hart, "Electrically Addressable Hybrid Architectures of Zinc Oxide Nanowires Grown on Aligned Carbon Nanotubes," *Advanced Functional Materials*, vol. 20, pp. 2470-2480, 2010 2010.

[229] J. C. Johnson, K. P. Knutsen, H. Q. Yan, M. Law, Y. F. Zhang, P. D. Yang, *et al.*, "Ultrafast carrier dynamics in single ZnO nanowire and nanoribbon lasers," *Nano Letters*, vol. 4, pp. 197-204, Feb 2004.

[230] R. S. Ruoff and D. C. Lorents, "MECHANICAL AND THERMAL-PROPERTIES OF CARBON NANOTUBES," *Carbon*, vol. 33, pp. 925-930, 1995.

[231] J. Gaillard, M. Skove, and A. M. Rao, "Mechanical properties of chemical vapor deposition-grown multiwalled carbon nanotubes," *Applied Physics Letters*, vol. 86, Jun 2005.

[232] S. Sotiropoulou and N. A. Chaniotakis, "Carbon nanotube array-based biosensor,"

Analytical and Bioanalytical Chemistry, vol. 375, pp. 103-105, Jan 2003.

[233] S. Iijima, C. Brabec, A. Maiti, and J. Bernholc, "Structural flexibility of carbon nanotubes," *Journal of Chemical Physics,* vol. 104, pp. 2089-2092, Feb 1996.

[234] M. De Volder, S. H. Tawfick, S. J. Park, D. Copic, Z. Z. Zhao, W. Lu, *et al.*, "Diverse 3D Microarchitectures Made by Capillary Forming of Carbon Nanotubes," *Advanced Materials,* vol. 22, pp. 4384-+, Oct 2010.

[235] M. Zhang, K. R. Atkinson, and R. H. Baughman, "Multifunctional carbon nanotube yarns by downsizing an ancient technology," *Science,* vol. 306, pp. 1358-1361, Nov 2004.

[236] Y. W. Heo, B. S. Kang, L. C. Tien, D. P. Norton, F. Ren, J. R. La Roche, *et al.*, "UV photoresponse of single ZnO nanowires," *Applied Physics a-Materials Science & Processing,* vol. 80, pp. 497-499, Feb 2005.

[237] D. Zhang, S. K. Lee, S. Chava, C. A. Berven, and V. Katkanant, "Investigation of electrical and optoelectronic properties of zinc oxide nanowires," *Physica B-Condensed Matter,* vol. 406, pp. 3768-3772, Oct 2011.

[238] K. Keem, H. Kim, G. T. Kim, J. S. Lee, B. Min, K. Cho, *et al.*, "Photocurrent in ZnO nanowires grown from Au electrodes," *Applied Physics Letters,* vol. 84, pp. 4376-4378, May 2004.

[239] C. L. Hsu, S. J. Chang, Y. R. Lin, P. C. Li, T. S. Lin, S. Y. Tsai, *et al.*, "Ultraviolet photodetectors with low temperature synthesized vertical ZnO nanowires," *Chemical Physics Letters,* vol. 416, pp. 75-78, Nov 2005.

[240] Y. B. Li, F. Della Valle, M. Simonnet, I. Yamada, and J. J. Delaunay, "High-performance UV detector made of ultra-long ZnO bridging nanowires," *Nanotechnology,* vol. 20, Jan 2009.

[241] P. Y. Yang, J. L. Wang, W. C. Tsai, S. J. Wang, J. C. Lin, I. C. Lee, *et al.*, "Photoresponse of hydrothermally grown lateral ZnO nanowires," *Thin Solid Films,* vol. 518, pp. 7328-7332, Oct 2010.

[242] G. Konstantatos and E. H. Sargent, "Nanostructured materials for photon detection," *Nature Nanotechnology,* vol. 5, pp. 391-400, Jun 2010.

[243] U. Ozgur, Y. I. Alivov, C. Liu, A. Teke, M. A. Reshchikov, S. Dogan, *et al.*, "A comprehensive review of ZnO materials and devices," *Journal of Applied Physics,* vol. 98, Aug 2005.

[244] J. D. Prades, R. Jimenez-Diaz, F. Hernandez-Ramirez, L. Fernandez-Romero, T. Andreu, A. Cirera, *et al.*, "Toward a systematic understanding of photodetectors based on individual metal oxide nanowires," *Journal of Physical Chemistry C,* vol. 112, pp. 14639-14644, Sep 2008.

[245] J. Tornow, K. Ellmer, J. Szarko, and K. Schwarzburg, "Voltage bias dependency of the space charge capacitance of wet chemically grown ZnO nanorods employed in a dye sensitized photovoltaic cell," *Thin Solid Films,* vol. 516, pp. 7139-7143, Aug 2008.

[246] B. J. Coppa, C. C. Fulton, S. M. Kiesel, R. F. Davis, C. Pandarinath, J. E. Burnette, *et al.*, "Structural, microstructural, and electrical properties of gold films and Schottky contacts on remote plasma-cleaned, n-type ZnO{0001} surfaces," *Journal of Applied Physics,* vol. 97, May 2005.

[247] X. Y. Yang, A. Wolcott, G. M. Wang, A. Sobo, R. C. Fitzmorris, F. Qian, *et al.*,

"Nitrogen-Doped ZnO Nanowire Arrays for Photoelectrochemical Water Splitting," *Nano Letters,* vol. 9, pp. 2331-2336, Jun 2009.

[248] J. A. Rogers, K. E. Paul, R. J. Jackman, and G. M. Whitesides, "Using an elastomeric phase mask for sub-100 nm photolithography in the optical near field," *Applied Physics Letters,* vol. 70, pp. 2658-2660, May 1997.

[249] M. K. Kwak, J. G. Ok, J. Y. Lee, and L. J. Guo, "Continuous phase-shift lithography with a roll-type mask and application to transparent conductor fabrication," *Nanotechnology,* vol. 23, Aug 2012.

[250] K. Ellmer, "Past achievements and future challenges in the development of optically transparent electrodes," *Nature Photonics,* vol. 6, pp. 808-816, Dec 2012.

[251] M. G. Kang, H. J. Park, S. H. Ahn, T. Xu, and L. J. Guo, "Toward Low-Cost, High-Efficiency, and Scalable Organic Solar Cells with Transparent Metal Electrode and Improved Domain Morphology," *Ieee Journal of Selected Topics in Quantum Electronics,* vol. 16, pp. 1807-1820, Nov-Dec 2010.

[252] S. Garaj, W. Hubbard, A. Reina, J. Kong, D. Branton, and J. A. Golovchenko, "Graphene as a subnanometre trans-electrode membrane," *Nature,* vol. 467, pp. 190-U73, Sep 2010.

[253] S. Lee, K. Lee, C. H. Liu, and Z. H. Zhong, "Homogeneous bilayer graphene film based flexible transparent conductor," *Nanoscale,* vol. 4, pp. 639-644, 2012.

[254] X. Li, Y. Zhu, W. Cai, M. Borysiak, B. Han, D. Chen, *et al.*, "Transfer of Large-Area Graphene Films for High-Performance Transparent Conductive Electrodes," *Nano Letters,* vol. 9, pp. 4359-4363, Dec 2009.

[255] Y. Zhu, Z. Z. Sun, Z. Yan, Z. Jin, and J. M. Tour, "Rational Design of Hybrid Graphene Films for High-Performance Transparent Electrodes," *Acs Nano,* vol. 5, pp. 6472-6479, Aug 2011.

[256] A. Reina, H. B. Son, L. Y. Jiao, B. Fan, M. S. Dresselhaus, Z. F. Liu, *et al.*, "Transferring and Identification of Single- and Few-Layer Graphene on Arbitrary Substrates," *Journal of Physical Chemistry C,* vol. 112, pp. 17741-17744, Nov 2008.

[257] X. S. Li, W. W. Cai, J. H. An, S. Kim, J. Nah, D. X. Yang, *et al.*, "Large-Area Synthesis of High-Quality and Uniform Graphene Films on Copper Foils," *Science,* vol. 324, pp. 1312-1314, Jun 2009.

[258] H. A. Wriedt, "The O−Zn (Oxygen-Zinc) system," *Journal of Phase Equilibria and Diffusion,* vol. 8, pp. 166-176, 1987.